COPPE
Instituto Alberto Luiz Coimbra de Pós-Graduação e Pesquisa de Engenharia
UFRJ

HIERARCHICAL MGO CATALYSTS FOR ETHANOL UPGRADING TO 1-BUTANOL

Caio Henrique Pinheiro

Tese de Doutorado apresentada ao Programa de Pós-graduação em Engenharia Química, COPPE, da Universidade Federal do Rio de Janeiro, como parte dos requisitos necessários à obtenção do título de Doutor em Engenharia Química.

Orientador: Henrique Poltronieri Pacheco

Rio de Janeiro
Abril de 2025

HIERARCHICAL MGO CATALYSTS FOR ETHANOL UPGRADING TO 1-BUTANOL

Caio Henrique Pinheiro

TESE SUBMETIDA AO CORPO DOCENTE DO INSTITUTO ALBERTO LUIZ COIMBRA DE PÓS-GRADUAÇÃO E PESQUISA DE ENGENHARIA DA UNIVERSIDADE FEDERAL DO RIO DE JANEIRO COMO PARTE DOS REQUISITOS NECESSÁRIOS PARA A OBTENÇÃO DO GRAU DE DOUTOR EM CIÊNCIAS EM ENGENHARIA QUÍMICA.

Orientador: Henrique Poltronieri Pacheco

Aprovada por: D.Sc. Cristiane Barbieri Rodella
D.Sc. Alexandre Barros Gaspar
Prof. Carlos Andres Ortiz Bravo
D.Sc. Eugenio Furtado de Souza

RIO DE JANEIRO, RJ – BRASIL
ABRIL DE 2025

Henrique Pinheiro, Caio

Hierarchical MgO catalysts for ethanol upgrading to 1-butanol/Caio Henrique Pinheiro. – Rio de Janeiro: UFRJ/COPPE, 2025.

XX, 156 p.: il.; 29, 7cm.

Orientador: Henrique Poltronieri Pacheco

Tese (doutorado) – UFRJ/COPPE/Programa de Engenharia Química, 2025.

Referências Bibliográficas: p. 81 – 99.

1. Ethanol upgrading. 2. Magnesium oxide. 3. Structure sensitivity. I. Poltronieri Pacheco, Henrique. II. Universidade Federal do Rio de Janeiro, COPPE, Programa de Engenharia Química. III. Título.

Aos meus pais e à minha irmã

Agradecimentos

Esta tese é, sobretudo, resultado do apoio e da amizade que construímos no NUCAT. Agradeço incondicionalmente à Maria Auxiliadora e ao Antônio José — engraçado chamá-lo assim, prefiro Macarrão, do inglês *pasta* —, que são as pessoas mais generosas que já conheci nesta vida. Também agradeço ao meu amigo Henrique, que por acaso é meu orientador. Só ele sabe o que fez por mim – e ele também sabe o quanto sou grato. Por um lado ele acha que só fez a obrigação dele, e pelo outro eu finjo que acredito nisso. Não falamos sobre o assunto porque, aparentemente, ele prefere assim. Obrigado, Henrique, por absolutamente tudo.

Agradeço,

Aos amados amigos do NUCAT anexo: Gabi, Maynara, Ruan, Renato, Claudinho, Clara, Guilherme, Ídia, Claudio, Edmário, Hebert, Vitória, Victor, Profa. Vera, Neuman, Prof. Fabio, Débora, Lucas, Priscilla e Lorena. E também do I2000: Gabizinha, Evelyn, Carla, Anacleto e Rodrigo. Esses dividiram comigo não apenas os momentos de pressão, mas também dias de risos e gargalhadas genuínas – principalmente com as minhas idiotices laboratoriais.

Ao Felipe (do Engepol) e ao Pedro (da USP), que muito me ajudaram na síntese dos catalisadores desta tese.

Ao aluno de IC Matheus, meu fiel escudeiro.

Aos professores do PEQ, especialmente José Carlos Pinto e Argimiro Secchi, que são fontes de inspiração como educadores.

Ao Eugenio, grande amigo e mestre, meu agradecimento sincero. Foi um enorme incentivador nos momentos difíceis do doutorado, sempre apoiando e acreditando nas minhas ideias.

À Zoraya e ao Décio, minhas companhias diárias na minha casa em Botafogo. Zoraya, maternal e acolhedora, tornou-se um verdadeiro amparo nesses 5 anos.

À minha namorada, Thaís, que foi o alicerce primordial nesta reta final. Te amo. Obrigado por ser tão doce, compreensível e respeitosa, mesmo quando estou estressado. Agradeço também à minha sogra e ao meu sogro, pessoas batalhadoras e fontes de inspiração — especialmente à minha sogra, que, diga-se de passagem, cozinha muito bem.

Aos amigos de fora da academia: o pai de santo Rapha, o empresário Dhieguinho

Roots e meu advogado Matheuzinho. Minhas grandes amigas Marina, Nath, Ingrid e Bia. Aos membros do grupo Tião: Juninho Caboclo, Phaelzin, Babs, Alberto, Tio Davidson, Nega, Guga e Tonho.

Àqueles(as) que partiram no meio de minha trajetória, mas deixaram seus ensinamentos. E também àquele que se foi de forma literal e precoce, o querido Graziâni *in memoriam*.

Ao fomento recebido do CNPq (142211/2020-6)

Ao acolhe COPPE, especialmente a querida Josi. Agradeço também ao meu psicólogo Gabriel.

Aos amigos do ateliê, minha pausa semanal entre pincéis, dedos sujos e vinho. Obrigado por tornarem a arte um momento de diversão e sanidade no meio da loucura acadêmica. Camões e Geraldo, valeu por tantas boas histórias, cantorias no Karaokê e por me ensinarem que pintura também é terapia disfarçada.

Ao bar que frequento em Botafogo, o lendário (por motivos discutíveis) Gabiru.

Aos amigos que compuseram as equipes das nossas duas visitas ao LNLS para as medidas realizadas na linha IMBUIA: Henrique, Rodrigo, Ortiz e Dora. Sem dúvidas, foi a época mais inesquecível desses anos – acho que nunca me diverti tanto.

Ao Dr. Raul e ao Dr. Lucyano Macedo, da linha IMBUIA do LNLS.

A Deus e aos meus guias.

Ao chegar até aqui, é impossível não olhar para minha trajetória e reconhecer que esta tese é fruto de muito mais do que apenas meu esforço individual. Lembro-me da infância em Pouso Alegre-MG, quando meu pai me levava ao colégio de Honda Biz. Assim que chegávamos, com as mãos ele ajeitava com cuidado meu cabelo — amassado pelo capacete e cortado em forma de cuia, como mandava a moda da época —, e me dizia com carinho para me dedicar às aulas naquele dia. Espero, um dia, ser um pai tão dedicado e responsável quanto o senhor. Muito obrigado.

Recordo também de minha mãe, que preparava o café da manhã todos os dias e, ao me acordar, dizia: — Vamos levantar, filho; a gente vai vencer. Vencemos mãe. Mais tarde, já na graduação, ela passava os fins de semana correndo contra o tempo para lavar minhas roupas antes do meu inevitável e nada animador retorno dominical a São José dos Campos–SP. Realizei meu sonho, agora espero que a senhora realize os seus. Te amo.

Finalizo com um desejo que também é o meu, nas palavras de Luiz Antônio Simas:

> "Desejo que cada um tenha o direito de encontrar o mistério do que lhe é pertencimento, em gentileza e gestos de silêncio, toques de tambor e cantos de celebração da vida."

Resumo da Tese apresentada à COPPE/UFRJ como parte dos requisitos necessários para a obtenção do grau de Doutor em Ciências (D.Sc.)

HIERARCHICAL MGO CATALYSTS FOR ETHANOL UPGRADING TO 1-BUTANOL

Caio Henrique Pinheiro

Abril/2025

Orientador: Henrique Poltronieri Pacheco

Programa: Engenharia Química

O aprimoramento da conversão do etanol em produtos de maior valor agregado é uma estratégia promissora para diversificar rotas de aproveitamento dessa matéria-prima. Entretanto, apesar do interesse crescente, os mecanismos reacionais associados à conversão a 1-butanol em catálise heterogênea ainda não são plenamente compreendidos. Nesse contexto, o óxido de magnésio (MgO) destaca-se como uma alternativa catalítica de baixo custo e ampla disponibilidade. Estudos recentes conduzidos por nosso grupo indicam que defeitos estruturais específicos em MgO podem exercer influência significativa nos caminhos reacionais envolvidos. Para investigar essa hipótese, foram desenvolvidos catalisadores hierárquicos com morfologias controladas em forma de flores (MgO-f) e fios (MgO-w), além de uma amostra de referência sem morfologia definida (MgO-p). Esses materiais foram caracterizados detalhadamente e avaliados quanto à atividade e seletividade na conversão de etanol. Os resultados revelaram que a morfologia afeta diretamente parâmetros estruturais como microdeformação e tamanho de cristalito, os quais se correlacionam com a estabilidade de intermediários e a eficiência catalítica. Com o objetivo de avançar na identificação de espécies adsorvidas, empregou-se espectroscopia *in situ* por refletância difusa acoplada à espectrometria de massas (DRIFTS-MS), complementada por Nanospectroscopia por Infravermelho baseada em radiação síncrotron (SINS). Embora a abordagem SINS apresente potencial para análises com resolução espacial, os experimentos indicaram limitações metodológicas, principalmente associadas à baixa reprodutibilidade espectral ao longo da partícula e à dificuldade de distinguir contribuições topográficas e químicas. Os resultados dos testes catalíticos de bancada, por sua vez, reforçam que a estrutura morfológica do MgO influencia diretamente seu desempenho, não apenas por meio

da modificação das propriedades texturais, mas também pela distribuição de sítios ativos originados de baixa coordenação. Especificamente, os catalisadores MgO-p e MgO-f apresentaram rendimentos específicos de BuOH aproximadamente 205 % e 231 % superiores, respectivamente, em relação ao MgO-w, evidenciando a relevância da morfologia na promoção da rota de acoplamento.

Abstract of Thesis presented to COPPE/UFRJ as a partial fulfillment of the requirements for the degree of Doctor of Science (D.Sc.)

HIERARCHICAL MGO CATALYSTS FOR ETHANOL UPGRADING TO 1-BUTANOL

Caio Henrique Pinheiro

April/2025

Advisor: Henrique Poltronieri Pacheco

Department: Chemical Engineering

The improvement of ethanol conversion into higher value-added products is a promising strategy to diversify the utilization routes of this feedstock. However, despite the growing interest, the reaction mechanisms associated with the conversion to 1-butanol in heterogeneous catalysis are still not fully understood. In this context, magnesium oxide (MgO) stands out as a low-cost and widely available catalytic alternative. Recent studies conducted by our group indicate that specific structural defects in MgO may significantly influence the reaction pathways involved. To investigate this hypothesis, hierarchical catalysts with controlled flower-like (MgO-f) and wire-like (MgO-w) morphologies were developed, along with a reference sample with no defined morphology (MgO-p). These materials were thoroughly characterized and evaluated in terms of activity and selectivity in ethanol conversion. The results revealed that morphology directly affects structural parameters such as microstrain and crystallite size, which correlate with the stability of intermediates and catalytic efficiency. In order to advance the identification of adsorbed species, *in situ* diffuse reflectance infrared spectroscopy coupled with mass spectrometry (DRIFTS-MS) was employed, complemented by synchrotron-based infrared nanospectroscopy (SINS). Although the SINS approach offers potential for spatially resolved analysis, the experiments revealed methodological limitations, mainly associated with low spectral reproducibility across the particle and the difficulty in distinguishing topographic from chemical contributions. Bench-scale catalytic tests, in turn, reinforce that the morphological structure of MgO directly influences its performance, not only through modifications of textural properties but also by the distribution of low-coordination active sites. Specifically, the MgO-p and MgO-f catalysts exhibited BuOH-specific yields approximately 205% and 231%

higher, respectively, compared to MgO-w, highlighting the relevance of morphology in promoting the coupling route.

Contents

List of Figures

List of Tables

Glossary

3OHBuO 3-hydroxybutyraldehyde. 5

AcO acetaldehyde. xiii, 5–8, 10–13, 15–17, 52, 54, 56, 58, 59, 63, 64, 69, 73

AFM Atomic Force Microscopy. xiv, xv, 27, 28, 30, 31, 41, 70–72, 74, 75, 77, 78, 80

BD 1,3-butadiene. 1, 2, 13, 15–17, 55–57, 70

BET Brunauer-Emmett-Teller. 34, 45

BJH Barret-Joyner-Halenda. 34, 46

BuO butyraldehyde. 1, 6, 8, 9, 13, 52, 55–57, 67

BuOH 1-butanol. xiii, 1–15, 17, 18, 21, 30, 31, 52, 54–59, 63, 66, 79

CB carbon balance. 52–55, 101, 102

CrO crotonaldehyde. xiii, 7–9, 11–13, 52, 55, 56, 66, 69, 70

CrOH crotyl alcohol. 7, 13, 52, 55–57, 67, 69, 70

DEE diethyl ether. 2, 10, 15, 52

DFT density functional theory. 2, 7, 9, 12, 13, 19, 68, 69, 80

DRC Degree of Rate Control. 62

DRIFTS diffuse reflectance infrared Fourier transform spectroscopy. xiv, 3, 7, 8, 12, 16, 18, 31, 37, 39, 58, 64, 65, 67–71, 73, 74, 76, 79

EETPD Ex-Situ Ethanol Temperature-Programmed Desorption. xiii–xv, 38–41, 70, 73, 74, 76, 77, 80, 107

EG Ethylene Glycol. 26, 33

ET ethene. 1, 2, 10, 15, 52, 54, 57, 59, 63

EtO ethoxy. 5

EtOH ethanol. xiii–xv, 1–4, 6–18, 21, 25, 30, 31, 33, 35–37, 40, 41, 44, 50–59, 64, 65, 67–69, 71, 73, 74, 76–80, 101, 102, 106

FID Flame Ionization Detection. 36

FTIR Fourier transform infrared. xiii, xv, 27–30, 37, 47, 49, 71, 73, 74, 107

FWHM Full Width at Half Maximum. 23

GC Gas Chromatography. 35, 56

H_α alpha hydrogen. 11

HAP hydroxyapatite. xiii, 6, 8–14, 18, 55

HTO hydrotalcite-derived oxide. 9, 10, 63

IR Infrared. 2, 7, 16, 27–30, 37, 40, 41, 70, 71, 80

JCPDS Joint Committee on Powder Diffraction Standards. 34

KCE Kinetic Compensation Effect. 63

LNLS Synchrotron Light Laboratory. 40

Me_2CO acetone. 10, 15, 52

MPV Meerwein-Ponndorf-Verley. 7, 10, 17, 56

MPV-like Meerwein-Ponndorf-Verley-like. 6, 7, 10

MS mass spectrometry. xiv, xv, 7, 12, 31, 37, 64, 67, 70, 79, 106

PVP Polyvinylpyrrolidone. 26

PXRD Powder X-ray Diffraction. xiv, 3, 21, 31, 43, 44, 46, 66

RDS rate-determining step. 8, 11, 14, 17, 58

s-SNOM s-Scanning Near-Field Optical Microscopy. xiii, 27, 28, 38, 41, 70, 74

SEM Scanning Electron Microscopy. xiii, xiv, 3, 26, 34, 48, 50

SEM - FIB Scanning Electron Microscopy – Focused Ion Beam. 38

SINS Synchrotron-radiation-based Infrared Nanospectroscopy. xiv, 3, 27, 28, 30, 31, 38–41, 70, 71, 73, 74, 76–78, 80

TGA Thermogravimetric Analysis. 3, 44

TOS Time-on-stream. xiv, 35, 51, 52, 55, 101, 102

TPD temperature-programmed desorption. 49, 58

TST Transition State Theory. 3, 60, 61, 63, 79, 103

XRD X-ray diffraction. 33, 42, 79, 80

Chapter 1

Introduction

1.1 Background and Motivation

Ethanol (EtOH) is a widely recognized chemical platform that can be converted into various higher products for the industry. Among them, ethene (ET), hydrogen, 1,3-butadiene (BD), and 1-butanol (BuOH) stand out. Moreover, higher alcohols, aromatics, and lubricants can be obtained through dimerization and oligomerization reactions. Currently, all these products are mostly derived from petroleum. For instance, BuOH is obtained by propylene hydroformylation followed by the hydrogenation of butyraldehyde (BuO) (ABDULRAZZAQ and SCHWARTZ, 2019). However, there is a growing interest in replacing these conventional routes with processes that use biomass as a feedstock. In order for these processes to be competitive, they must exhibit high yields, low operating costs, and long operational stability. Additionally, economic feasibility depends on the development of advanced catalysts capable of achieving high EtOH conversions while maintaining high selectivity toward the desired product. Furthermore, the search for catalytic routes based on renewable raw materials aligns with global efforts to reduce the environmental impacts associated with fossil fuel dependency, reinforcing the relevance of biomass conversion processes from a sustainable development perspective.

In particular, BuOH has multiple industrial applications, especially in the paints and solvents sectors. More recently, it has been proposed as an alternative to fossil fuels due to its high energy density (29.2 MJ L^{-1}), which is superior to that of EtOH (19.2 MJ L^{-1}), potentially working as a partial substitute to gasoline (KOLESINSKA *et al.*, 2019). Additionally, the BuOH market shows a growth trend. It is estimated that its global commercialization will reach approximately $9 billion by 2026 (CHOI *et al.*, 2021). Projections also indicate that the EtOH output will continue to grow until 2031, even under conservative scenarios, ranging between 42.7

and 50.9 billion liters per year (EPE, 2021), as shown in Figure 1.1.

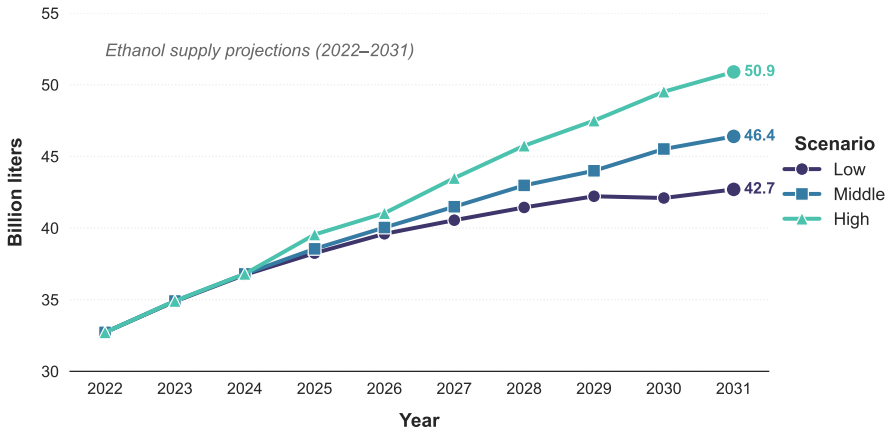

Figure 1.1: Projection of total EtOH supply in Brazil
Source: adapted from EPE (2021). In 2020, the total EtOH supply was 33.6 billion liters.

One of the main challenges in the catalytic upgrading of EtOH lies in the occurrence of multiple simultaneous reactions and the formation of by-products. The reaction pathway involves dehydrogenation, coupling, and subsequent transformations. These transformations are partially known and are typically classified into the Lebedev and Guerbet routes, which lead to the formation of BD and BuOH, respectively. In addition, even before undergoing dehydrogenation, EtOH can be dehydrated to form ET or diethyl ether (DEE) (HANSPAL *et al.*, 2017). In this context, the selectivity of the process strongly depends on the tuning of catalytic properties, particularly surface acidity and basicity, as well as reaction conditions such as temperature and residence time (CARVALHO *et al.*, 2012; CHIEREGATO *et al.*, 2015; KOZLOWSKI and DAVIS, 2013; SCALBERT *et al.*, 2014).

It is important to note that significant gaps remain in various aspects of the reaction mechanism. Although several pathways have been proposed there is no consensus regarding the intermediates and kinetically dominant steps. This controversy arises largely from the difficulty in directly detecting intermediate species by spectroscopy, with their presence often inferred through indirect evidence and simulations based on density functional theory (DFT). Additionally, the exact assignment of some vibrational modes observed in mid-Infrared (IR) spectroscopy experiments remains under debate.

Despite advances in mechanistic understanding, few studies integrate structural, spectroscopic, and microkinetic observations to explain the origin of the catalytic behavior of MgO in this reaction. In particular, the impact of catalyst morphology on the modulation of surface chemistry and activation barriers remains unexplored. Based on this premise, this thesis is built upon the hypothesis that morphological

variations in MgO catalysts — especially those related to hierarchical architectures — directly influence the activation and transformation of EtOH into BuOH, altering the reactivity and selectivity patterns.

1.2 Objectives

This work investigates the effect of the morphology of three MgO structures on the catalytic performance in the conversion of EtOH into BuOH and other higher products. The main objective is to understand how the physical and crystalline structure of the catalysts influences their reactivity, selectivity, and the mechanisms involved in the reaction. To achieve this, the following specific objectives are established:

- Prepare and characterize MgO catalysts with different morphologies, including flower-like particles (MgO-f), wires (MgO-w), and a reference material with no controlled morphology (MgO-p);
- Characterize the catalysts in terms of structure, texture, and morphology using techniques such as Powder X-ray Diffraction (PXRD), Scanning Electron Microscopy (SEM), Thermogravimetric Analysis (TGA), and N_2 physisorption;
- Evaluate the catalytic activity and selectivity in the conversion of EtOH, quantify the main products by chromatography, and estimate kinetic parameters;
- Interpret the reaction kinetics based on the Transition State Theory (TST), applying nonlinear models and discussing compensation effects;
- Investigate surface intermediates and adsorbed functional groups using *in situ* spectroscopy (diffuse reflectance infrared Fourier transform spectroscopy (DRIFTS)) and spatial resolution techniques such as Synchrotron-radiation-based Infrared Nanospectroscopy (SINS);

Chapter 2

Literature Review

2.1 Guerbet Reaction and Other Mechanisms

The historical development of the Guerbet process illustrates the evolution of catalytic chemistry in the early 20th century. The Guerbet reaction, named after Marcel Guerbet, was first reported in 1899 and represents a significant advance in alcohol chemistry. Guerbet showed how short-chain alcohols, such as isopropanol, could couple to form longer-chain alcohols (4-methyl-2-pentanol and 2,4-dimethyl-6-heptanol) via aldol condensation in a homogeneous catalytic system (GUERBET, 1909). Figure 2.1 presents an example of the Guerbet reaction mechanism in heterogeneous catalysis, which involves the coupling of two EtOH molecules to form BuOH, with the release of water. The reaction pathway sequentially involves a complex series of elementary reactions: dehydrogenation, aldolization, dehydration, and hydrogenation. The formed BuOH can undergo cross-coupling with a new EtOH molecule or other higher alcohols to produce 1-hexanol, 2-ethyl-1-butanol, and 1-octanol, among others (WU *et al.*, 2018). However, it is important to highlight that the complete description of the elementary steps in heterogeneous systems has not been fully elucidated and remains controversial.

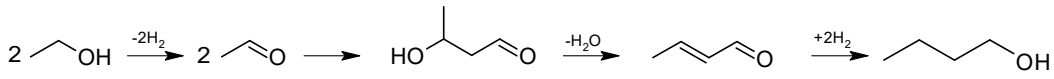

Figure 2.1: Guerbet Reaction
Source: GABRIËLS *et al.* (2015); KOZLOWSKI and DAVIS (2013)

Figure 2.2 shows the detailed mechanism of the Guerbet reaction over Mg_xAlO_y surface, which includes pairs of adjacent acidic M^{n+} (where M = Mg or Al and n = 2 or 3) and basic O^{2-} sites. In the first step, an EtOH molecule initially adsorbs

onto a Lewis acid site and onto an adjacent basic site to generate an ethoxy (EtO) species, which then undergoes H removal from its C_α to form acetaldehyde (AcO). Secondly, aldol condensation of AcO occurs on a site of a Lewis Acid-Brønsted base pair. In this step, the pair adsorbs one AcO molecule and then processes proton abstraction generating an enol specie, which attacks a vicinal AcO molecule to yield a four-carbon aldol – 3-hydroxybutyraldehyde (3OHBuO). Finally, the aldol undergoes dehydration (to form an α,β-unsaturated carbonyl compound) and several hydrogenation steps to form BuOH. However, it is important to note that these steps are not fully elucidated, as discussed by YOUNG and DAVIS (2018) and further supported by DE SOUZA *et al.* (2020).

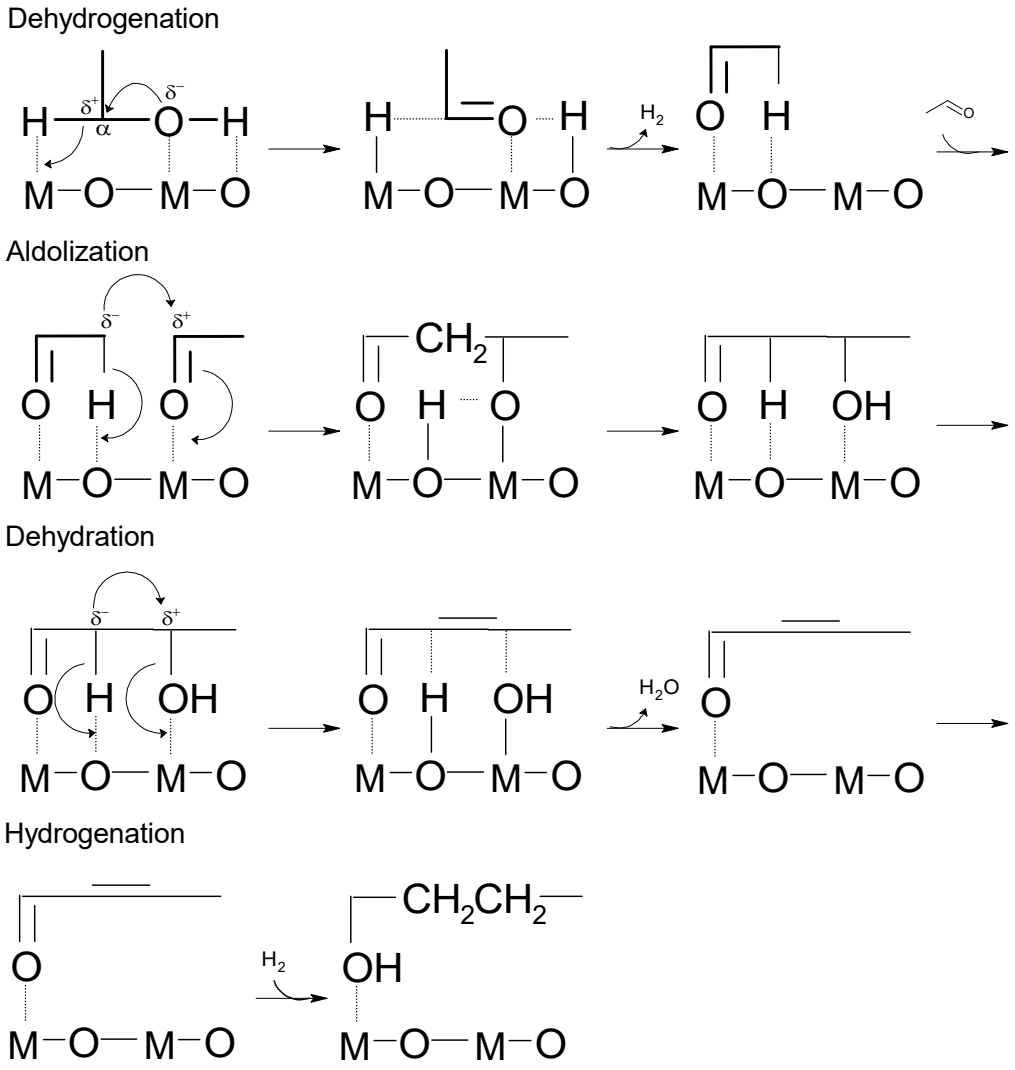

Figure 2.2: The formation mechanism for BuOH on pairs of adjacent Lewis acid-base sites

Adapted from DI COSIMO *et al.* (2000); WU *et al.* (2018).

In addition to the previously described Guerbet mechanism, BuOH can also be

synthesized through the dimerization of two EtOH molecules, without involving any aldol intermediate. This process is facilitated by the activation of the C_{β}-H bond through a basic metal oxide. The resulting surface species then condenses with a neighboring EtOH molecule to directly form BuOH and water (NDOU *et al.*, 2003; SCALBERT *et al.*, 2014). This pathway was initially considered following observations that the addition of Guerbet intermediates did not enhance BuOH production rates, as noted in studies using basic zeolites (YANG and MENG, 1993). Moreover, research by GINES and IGLESIA (1998) supported this view, demonstrating through isotopic tracer studies that direct EtOH coupling could occur without AcO formation when using K-$Cu_yMg_5CeO_x$ catalysts (XU and IGLESIA, 1998). The direct reaction between two EtOH molecules has also been proposed with other catalysts such as MgO (NDOU *et al.*, 2003), and nonstoichiometric hydroxyapatite (HAP) (TSUCHIDA *et al.*, 2006).

SCHEID *et al.* (2019), using the Mg_xAlO_y catalyst obtained from hydrotalcite, performed a series of bench-scale kinetic experiments. The authors propose a mechanism of elementary reactions, which were analyzed by the discrimination of kinetic parameters to select the main set of thermodynamically favorable reactions. The outcomes demonstrated that the Guerbet pathway does occur, but only up until the formation of BuO, though the final conversion of this intermediate to BuOH is not thermodynamically advantageous. Thus, the authors claimed that the direct condensation of two EtOH molecules to BuOH was the most favorable path.

For alcohol coupling over HAP, SCALBERT *et al.* (2014) presented thermodynamic insights to conclude that the self-aldol condensation of AcO — the second step in the Guerbet route, Figure 2.2 — is not kinetically relevant above 623 K. Beyond the mentioned direct route, the authors proposed a new reaction mechanism as another indirect route different from the Guerbet path, as shown in Figure 2.3. The suggested mechanism starts with an EtOH molecule undergoing dehydrogenation. The second step is dehydration, in which AcO reacts with a second EtOH molecule, yielding but-2-en-1-ol either directly (step 2a) or even by formation 1,4-butanediol as an intermediary – steps $2b_1$ and $2b_2$. In step 3, BuOH is finally formed after the Meerwein-Ponndorf-Verley-like (MPV-like) reaction of but-2-en-1-ol with a third EtOH molecule.

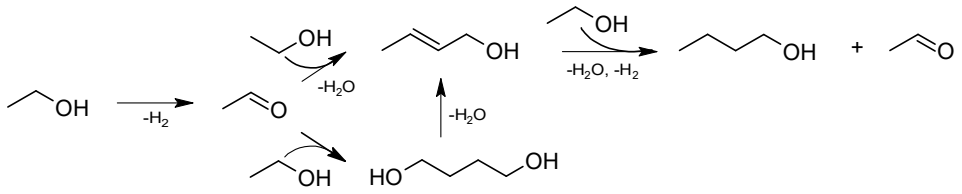

Figure 2.3: BuOH formation minor indirect route
Adapted from SCALBERT *et al.* (2014).

It is important to note that, although SCALBERT *et al.* (2014) label step 3 of the mechanism as a Meerwein-Ponndorf-Verley (MPV) reaction, this term is not entirely appropriate. Therefore, in this text, we use the term MPV-like in such cases. A more precise definition for the MPV reaction is when it uses an additional molecule, known as a sacrificial alcohol as external hydrogen (H) source to reduce carbonyl groups (C=O) (DE SOUZA *et al.*, 2020; IVANOV *et al.*, 1994), which is not the exact case in the mechanism proposed by SCALBERT *et al.* (2014). That is to say the MPV reaction is necessarily the "exchange" of a carbonyl group of one species for the hydroxyl group of another, a fact that does not occur due to the persistence of the hydroxyl group in the C_4 alcohol in step 3 of the SCALBERT *et al.* (2014) mechanism, Figure 2.3. For the sake of accuracy, whenever a C=C bond undergoes direct hydrogenation by a sacrificial EtOH, we will opt rather to this process will be referred to as MPV-like

CHIEREGATO *et al.* (2015), in turn, aimed to elucidate the key intermediates of EtOH conversion over MgO. They provided evidence from reactivity tests, in situ IR spectroscopy, mass spectrometry (MS) analysis, and theoretical modeling that the role of the aldol condensation step in the overall reaction is minimal. Supported by DFT, the authors specify that the carbanion species — formed by the abstraction of one proton from the methyl group in EtOH — can be assigned in DRIFTS results in the band in ν= 1143 cm^{-1}. The spectra tendency along with the temperature suggests that, after 523 K, the carbanion and AcO/acetyl may react together to form adsorbed crotyl alcohol (CrOH). Moreover, they observe no signal of acetaldol or crotonaldehyde (CrO) in the spectra, leading them to conclude that the aldol condensation (the key feature of the Guerbet mechanism) is not the key mechanism in the formation of the C_4 compounds from EtOH on basic oxide materials.

Considering the prior statements, the authors reported a new indirect mechanism instead of the Guerbet pathway. Figure 2.4 shows the proposed mechanism. It can be noted that there is neither aldol nor CrO as intermediates. The route starts with EtoH's H_β bonding with the MgO basic site (O^{2-}), and the carbanion is stabilized by the adjacent Mg. Then there is a nucleophilic attack by a C_β (from a second vicinal

EtOH molecule) on the C_α of the first EtOH. The structure is then stabilized by the formation of the C–C bond simultaneous to the cleavage of the C–OH bond. Water is formed, and BuOH is finally desorbed, restoring the active sites for the next cycle. Nevertheless, it is important to emphasize that their mechanism does not account for the fact that CrO and BuO are formed and detected in these reactions over MgO and HAP (WANG *et al.*, 2020; YOUNG *et al.*, 2016).

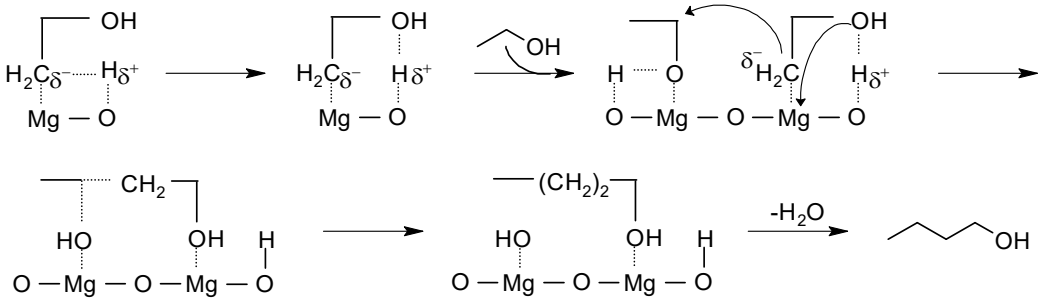

Figure 2.4: Proposed mechanism disregarding Guerbet reaction
Source: PACHECO (2019), Adapted from CHIEREGATO *et al.* (2015).

YOUNG *et al.* (2016) assessed the kinetics of the aldol condensation step of AcO on TiO_2, HAP, and MgO. An important insight from this study is that the activation of the C-H bond does not seem to play a kinetically relevant role. This suggests that the rate-limiting factor of the reaction is not in the formation of the enolate but in other steps of the process that follow. Experimental results with adsorption microcalorimetry and DRIFTS provided additional information on how the adsorbed aldehydes interact with the catalytic surface. These results revealed that surface reactions, such as AcO adsorption and product desorption, occur easily even under mild conditions. A critical observation well made by the authors is that if the bimolecular surface reaction between the surface enolate and AcO were the rate-determining step (RDS), a second-order dependence on AcO in the condensation kinetics would be expected. However, experimental data show a first-order reaction concerning AcO. This reinforces the conclusion that the surface reaction between AcO and the enolate is not the RDS.

The rate at which the coupling step between two AcO molecules occurs is attributed to the acid-base pairs strenght over the surface, such as in MgO and HAP. Additionally, the acid-base features extend to other reaction steps. For instance, HANSPAL *et al.* (2015) demonstrated that the retention of adsorbed EtOH over the MgO surface at significantly higher temperatures, 673 K, compared to HAP, 473 K, indicates a stronger interaction between EtOH and MgO than between EtOH and HAP. This is consistent with adsorption microcalorimetry results, which showed that the initial differential heat of EtOH adsorption on HAP is approximately 30

kJ mol^{-1} lower than on MgO. In addition, the desorption temperature of ethoxide intermediates was 200 K lower on HAP than on MgO. These quantitative differences confirm the higher basicity of MgO relative to HAP. Compared to HAP, MgO has a basicity, which allows it to keep EtOH adsorbed at higher temperatures. This aligns with the idea that weak acid-base bifunctional catalysts facilitate the Guerbet coupling. With this observation by HANSPAL *et al.* (2015), it becomes evident to correlate the success of the Guerbet mechanism due to the incorporation of a Lewis acid such as Al^{3+} present in the hydrotalcite-derived oxide (HTO) compared to pure MgO (DI COSIMO *et al.*, 1998, 2000).

In order to contribute to the discussion, DE SOUZA *et al.* (2020) conducted a combined theoretical and experimental approach to investigate the candidate pathways of EtOH-to-BuOH upgrading reaction over MgO. DFT calculations revealed that a defective kink site of MgO increases EtOH's reactivity. Then, the authors probed two sets of elementary reaction steps namely aldol and β- routes. The first mechanistic proposal was based on the EtOH C_α-activated Guerbet-like sequence of the reactions (KOZLOWSKI and DAVIS, 2013), whereas the second one was based on a direct C_β-activated C–C coupling (YANG and MENG, 1993), as shown in Figure 2.5.

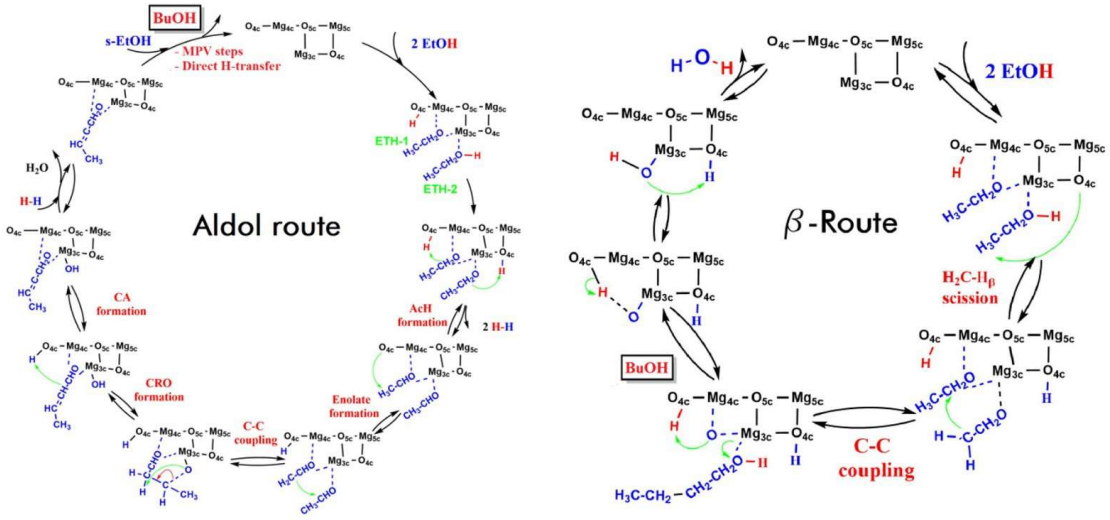

Figure 2.5: Elementary Steps of Aldol and β-Route Reaction Pathways for EtOH. Adapted from DE SOUZA *et al.* (2020)

One key computational result found by DE SOUZA *et al.* (2020) suggests that both BuOH and BuO can be generated through the β-route. Furthermore, the sequential formation of the CrO molecule is unfavorable — this step can be noted around the bottom of the Aldol route in Figure 2.5 —, which seems to indicate that the direct β-route is more likely. However, at high temperatures (up to 673 K), the activation of the EtOH's H-C_β bond is unlikely and, therefore, the surface

concentration of aldol intermediates tends to increase through the activation of H-C_α bond, thus favoring the occurrence of the more endergonic direct route. All in all, in the BuOH formation from EtOH, at lower temperatures, the prevalent pathway is the direct coupling (β-route), whereas from 673 K on the Guerbet-like predominates.

Considering the pivotal role of H for all mechanisms presented so far, another important aspect of the conversion mechanism of EtOH to BuOH regards the proton source in the hydrogenation and dehydration steps. While the community generally agrees that the dehydrogenation process occurs on the catalyst's basic site, it is not exactly known which molecule the proton comes from to hydrogenate the C_4 oxygenates to form BuOH. In turn, it can be pointed out that the most candidate molecules for hydrogen sources should be: i) gas-phase hydrogen; ii) surface hydrogen adatoms; or iii) EtOH itself by the direct hydrogen transfer via MPV (or MPV-like) reaction. The first hypothesis was rebutted by research conducted by GINES and IGLESIA (1998), who conducted experiments using gas-phase deuterium and observed minimal deuterium integration into the coupling products when the reaction took place on mixed oxides of Mg and Ce. After that, YOUNG and DAVIS (2018) noticed that adding dihydrogen or deuterium to the Guerbet coupling of EtOH over HAP and MgO did not affect the rate or selectivity of the reaction toward BuOH. Both catalysts enhance the MPV-like hydrogen transfer from EtOH to acetone (Me_2CO) at 473 K, but neither catalyst could hydrogenate Me_2CO with H_2. The authors state that during the Guerbet coupling process, all hydrogen transfer processes include MPV-like interactions between alcohols and carbonyls, with C=O bonds undergoing direct hydrogenation rather than C=C bonds.

Beyond identifying the hydrogen source, understanding how catalyst composition influences the cascade reaction mechanism is also crucial to elucidate the Guerbet pathway. For the Guerbet pathway over HTO, some essential inferences are widely accepted. For instance, using a Mg_xAlO_y catalyst and combining evidence from spectroscopy and isotopic exchange experiments, DI COSIMO *et al.* (1998) studied the impact of the catalyst structure on EtOH upgrading. The authors claimed that the nature, density, and strength of the surface basic sites depended on the Al content. The addition of controlled amounts (Al/(Al+Mg) < 0.2) of Al^{3+} cations to MgO significantly increased the rate of AcO formation due to the formation of new surface Lewis acid–strong base pair of sites. On the other hand, the dehydration of EtOH to ET and the coupling and dehydration to DEE increased with Al content, probably reflecting the density increase of both Al^{3+}–O^{2-} pairs and low- and medium-strength basic sites. Notably, the formation rate of DEE increased by approximately 130 times, and that of ET by 15 times, when comparing pure MgO

with the Al / (Al + Mg) = 0.65 catalyst.

Until now, the essential works that have laid the groundwork for understanding the mechanism of BuOH formation from EtOH in terms of heterogeneous catalysis have been outlined. Specifically, the focus has been on MgO and Mg_xAlO_y catalysts. Throughout the previous paragraphs, one key underlying aspect for these catalysts is the pivotal role of the balance between acidic and basic sites for the success of the Guerbet coupling. Stoichiometric HAP ($Ca_{10}(PO_4)_6(OH)_2$), in turn, it widely plays a similar role to the mentioned oxides, where Ca acts as Lewis acid site. For instance, TSUCHIDA *et al.* (2008) used HAP catalysts with different Ca/P molar ratios for EtOH upgradding to BuOH. They observed that increasing the Ca/P ratio increased the concentration of basic sites and reduced the density of acid sites.

HO *et al.* (2016) were pioneers in elucidating how the Guerbet mechanism occurs over HAP. They investigated the EtOH condensation pathway over HAP using in situ titration and spectroscopic experiments, within a partial pressure range of 3.5 kPa – 9.4 kPa of EtOH and 0.06 kPa – 0.12 kPa of AcO. Their findings showed that EtOH dehydrogenation occurs on Ca–O sites, while AcO condensation is catalyzed by $CaO/(PO_4)_3$ pairs. The proposed mechanism involves sequential steps of dehydrogenation, aldol condensation, and hydrogen transfer, similar to those of MgO.

Figure 2.6 illustrates the proposed mechanism for the aldol condensation of AcO over HAP. In Step I, AcO adsorbs onto the catalyst surface. Step II, identified as the RDS, involves the abstraction of alpha hydrogen (H_α) by a basic surface oxygen, generating an enolate species stabilized by adjacent phosphate groups. In Step III, this enolate attacks the carbonyl group of another AcO molecule, forming the aldol intermediate (acetaldol). Step IV corresponds to the dehydration of acetaldol to produce CrO. Subsequent desorption of CrO and water occurs in Steps V and VI, respectively. The figure also highlights the potential inhibition caused by EtOH, which may revert key steps and reduce the efficiency of the condensation pathway.

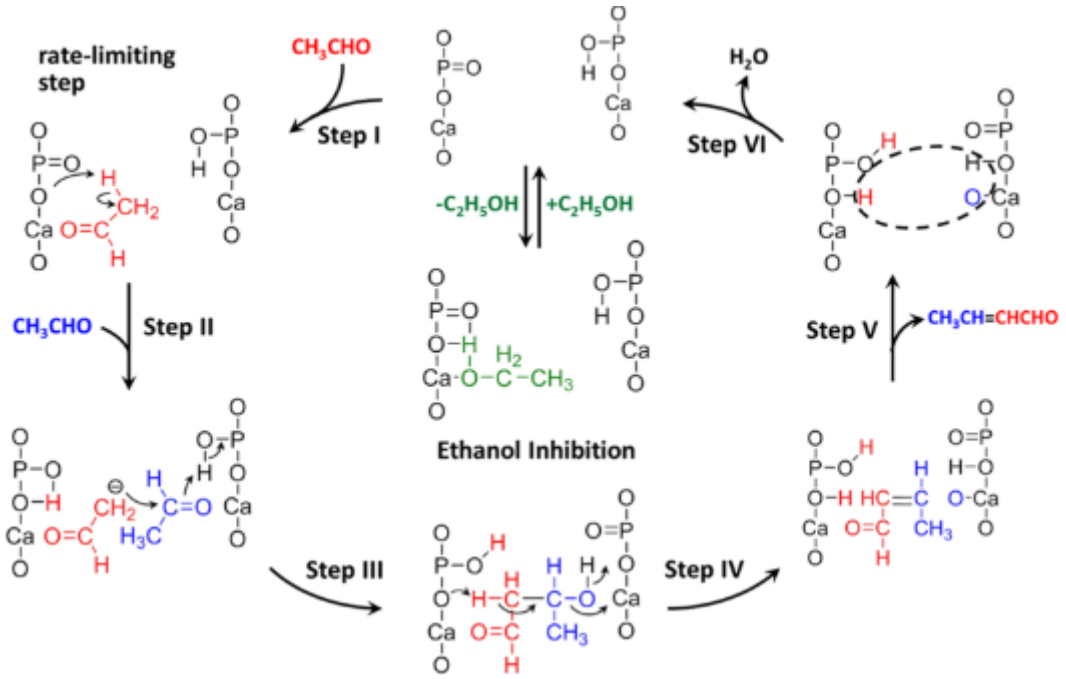

Figure 2.6: Reaction Mechanism for Aldol Condensation of AcO to CrO over HAP
Adapted from HO *et al.* (2016) Copyright 2016 American Chemical Society

The proposals of mechanistic coupling for both MgO and HAP catalysts, besides having acidic and basic sites, also share another characteristic in computational investigations. Both structures require a vicinal EtOH species intentionally allocated in the structure for the coupling reaction to occur. For instance, DE SOUZA *et al.* (2020), chose the kink-defected active center of MgO for DFT calculations, as mentioned earlier. This type of defective site enables coupling due to the proximity of enolates and vicinal AcO, each formed by the abstractions of protons from two EtOHs. On the other hand, in the study presented by HO *et al.* (2016), although the proposed scheme (Figure 2.6) suggests the spatial proximity of reactive species on HAP, there is still no computational evidence indicating which specific HAP sites — or structural defects — could enable such proximity. In this context, it is worth noting that the DFT calculations reported by BRASIL *et al.* (2021) constitute a rare example of theoretical investigation on EtOH conversion over HAP. However, these calculations were limited to a single, ideal HAP (0001) surface, which restricts their mechanism insights. As a result, important experimental factors, such as surface defects and HAP polycrystalline characteristics, as well as how reactants can stay vicinally alocate, have not been explored yet.

WANG *et al.* (2020) also assessed the coupling of EtOH to BuOH over HAP by DRIFTS-MS results. Figure 2.7 illustrates the general mechanism proposed by the authors. The process begins with the adsorption of EtOH on the surface of the HAP catalyst, primarily at the Ca^{2+}/OH^{-} and POH/OH^{-} acid-basic sites. Once adsorbed, EtOH undergoes dehydrogenation, resulting in the formation of AcO (Step

I). Following AcO formation, an aldol condensation reaction occurs at the Ca^{2+}/OH^{-} sites, yielding CrO (Step II), a critical step for subsequent steps. CrO is then hydrogenated via direct hydrogen transfer from another EtOH molecule, leading to the formation of CrOH (Step III). The next stage involves the isomerization and tautomerization of CrOH to BuO over the POH/OH^{-} sites (Step IVa), highlighting the significant role these sites play in the reaction mechanism. BuO then undergoes a second hydrogenation step, again facilitated by direct hydrogen transfer, ultimately yielding BuOH (Step V). Additionally, during the reaction, CrOH can isomerize to form 3-butene-1-ol (Step IVb), indicating alternative pathways within the reaction mechanism.

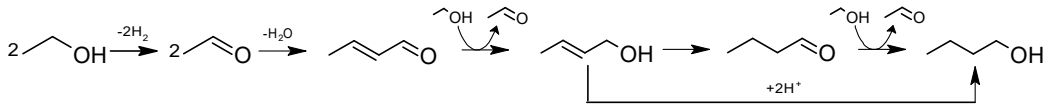

Figure 2.7: Generally accepted pathways of EtOH coupling to BuOH over HAP
Adapted from WANG *et al.* (2020) Copyright 2020 American Chemical Society

The mechanism proposed by WANG *et al.* (2020) is similar to that presented by HO *et al.* (2016). What stands out is the absence of spectroscopic evidence for an aldol intermediate due to high reactivity, as is the case with Mg and Al oxides. Direct detection of this species would provide the definitive signature for the Guerbet mechanism in the conversion of EtOH to BuOH over HAP.

Building on studies investigating the catalytic properties of HAP, another study focused on exploring not only the composition but also the preparation methodologies of these materials and their direct impacts on catalytic activity. In this context, BRASIL *et al.* (2021) examined different HAP preparation methods such as ultrasound, microwave, and autoclave, and how each influences the catalytic activity for converting EtOH to BuOH and BD. It was observed that the synthesis methods significantly alter the number and distribution of acid and base sites, which in turn directly affects the selectivity of the products. Additionally, the study presents a computational approach using DFT to investigate the twelve-step reaction pathways for EtOH conversion on the HAP(0001) surface. To the best of our knowledge, this is the first published paper that conducts DFT simulations of ethanol upgrading with HAP. BRASIL *et al.* (2021) show that the most energetically favorable reaction sequence on the HAP(0001) surface involves the adsorption and deprotonation of EtOH, forming ethoxide and AcO. Furthermore, the presence of acid and basic sites promotes the formation of higher alcohols via aldol condensation. This study reinforces the understanding that suggests Ca^{2+} as Lewis acid sites and

O in PO_4^{3-} groups as Lewis base sites (HO *et al.*, 2016; WANG *et al.*, 2020).

2.2 Ethanol-to-1-butanol over MgO and Mg_xAlO_y catalysts

In the previous section, throughout the presentation of the mechanistic development of the Guerbet reaction, several classical catalysts were outlined, such as pure MgO (DE SOUZA *et al.*, 2020; NDOU *et al.*, 2003), Mg/Al-based mixed oxide (LEÓN *et al.*, 2011; VIKÁR *et al.*, 2023) (referred to henceforth as Mg_xAlO_y), and HAP (TSUCHIDA *et al.*, 2006, 2008). Besides, notable strategies included in these kinds of catalysts are the addition of transition metals (KAMIENIAK *et al.*, 2016; MARCU *et al.*, 2013,?; MÜCK *et al.*, 2021). As this study focuses on MgO-based catalysts, the discussion in this section is predominantly centered on MgO and Mg_xAlO_y catalysts.

Basic oxides catalysts have been widely applied in the EtOH upgrading reaction (KOZLOWSKI and DAVIS, 2013; NDOU and COVILLE, 2004; NDOU *et al.*, 2003), among which MgO exhibits substantial activity ($x_{EtOH} = 0.56$) and selectivity ($S_{BuOH} = 0.33$) at 723 K and 1 bar (NDOU *et al.*, 2003). Although MgO exhibits moderate activity and is not considered a highly selective catalyst, it is commonly used due to its simplicity and ease of modeling. This feature is linked with its acidic and basic sites, which can promote EtOH coupling. Again, the catalytic performance of such materials is primarily determined by the interplay of its acid and basic properties. In addition, KOZLOWSKI and DAVIS (2013) emphasized another important catalyst feature in this case, which regards the catalyst efficiency of promoting the dehydrogenation steps – the RDS. Many authors explore these two insights to design and improve the efficiency of catalysts applied to EtOH upgrading.

Theoretical studies confirmed that the MgO surface terraces — composed of 5-fold coordinated Mg_{5c} and O_{5c} sites — are essentially inert in the activation reaction for several molecules (BRANDA *et al.*, 2003; CHIZALLET *et al.*, 2006), including EtOH (BRANDA *et al.*, 2009; DE SOUZA *et al.*, 2020). A frequent strategy to create a more reactive surface, with lower coordination Mg and O sites, is doping the catalyst with other atoms. Efforts were made to enhance BuOH selectivity over MgO catalysts by doping them with various alkaline earth (e.g., Ca, Ba) and transition (e.g., Zn, Ce, Zr, Pb, Sn) metals (NDOU *et al.*, 2003). Nonetheless, no improvement in the catalytic performance was observed. On the contrary, the incorporation of these metal additives into MgO led to a significant reduction in BuOH yield, ranging from 0.29 % to 7.58 %, compared to 18.39 % for pure MgO, suggesting that these modifications negatively affect the catalytic pathways or the

selectivity of EtOH toward BuOH over MgO-based catalysts. The addition of these metals largely decreased the strong-basic sites required for the abstraction of EtOH's H_β atom. As a result, higher temperatures were required for the strong basic sites to become active for EtOH condensation.

Hydrotalcite is a layered material that is considered to be a predominantly basic support. Aluminum atoms are partially substituted in the layered brucite structure of $Mg(OH)_2$ causing an excess of positive charge. Between the hydroxide layers, the positive charges are neutralized by interlayer anions, such as Cl^-, CO_3^{2-}, NO_3^-, SO_4^{2-}, and OH^- (CAVANI *et al.*, 1991). Upon heating, compensating anions and interlayer water are released as the layered structure collapses, and the Mg_xAlO_y structure is formed. It is well-known that Mg_xAlO_y has several sorts of active sites (SHARMA *et al.*, 2023). Among these: i) weak Brønsted basic sites, which are associated with surface hydroxyl groups remaining after activation; ii) medium-strength acid–base Lewis sites pairs, which are related to Mg^{2+}–O^{2-} and Al^{3+}–O^{2-}; and iii) strong Lewis basic sites, due to the presence of low coordinated O^{2-} species. Furthermore, Mg_xAlO_y shows improved performance in C–C bond formation reactions, such as the aldol self-condensation of Me_2CO or its cross-condensation (GABRIËLS *et al.*, 2015). However, in addition to BuOH, utilizing Mg_xAlO_y often also yields ET, DEE, AcO, butenes, and BD (CARVALHO *et al.*, 2013; LEÓN *et al.*, 2011; SCHEID *et al.*, 2019).

CARVALHO *et al.* (2012) employed Mg_xAlO_y derived from hydrotalcite for the conversion of EtOH into BuOH. In the same study, superior selectivity above 95 % for ET was achieved in Al_2O_3 catalysts, primarily due to the presence of a high amount of both Brønsted acid sites (Al–OH) and Lewis acid sites (Al^{3+}) on the surface, by the mechanism depicted in Figure 2.8. On the other hand, pure MgO sample (1:0) did not revel acid sites. This kind of site was generated only when Al was added to the MgO lattice (3:1). The density of acid sites decreased when Mg was added to Al_2O_3 (1:1). The density of acid sites decreased when Mg was added to Al_2O_3 (Al:Mg=1:1). Both mixed oxides (1:1 and 3:1) showed a low density of Brønsted acid sites. Regarding the catalytic behavior, pure MgO (1:0) revealed low activity for EtOH dehydrogenation and C_4 compounds. The low formation of C_4 products can be associated with the scarcity of Lewis acid sites on the MgO surface. This fact suggested that the C_4 yield is associated with the concomitant presence of pairs of acid and medium basic sites, which occurs only on the mixed oxide surface. Indeed, Mg_xAlO_y promoted the synthesis of the C_4 compounds due to the insertion of Al into the MgO lattice, which generates the referred adjacent acidic and medium basic sites.

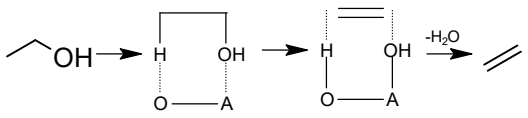

Figure 2.8: EtOH dehydration into Ethene on Brønsted or Lewis acid sites
Notes: Brønsted acid (A = H), Lewis acid (A = e.g., Al^{3+}).
Adapted from WU *et al.* (2018)

CARVALHO *et al.* (2013) conducted *in situ* IRspectroscopic experiments over Mg_xAlO_y. Part of the results suggests that there was the formation of surface carboxylate species, which are related to i) the formation of AcO as an intermediate, and ii) the hindering of the progress of aldol condensation in the Guerbet mechanism by coke deposition. This second statement was later confirmed by computational evidence by TAIFAN *et al.* (2017b). The authors claimed that aldehyde intermediates resulted in strongly bound surface species stable even at high temperatures, assigned to surface acetate, and/or 2,4-hexadienal.

MgO catalysts exhibit a strong mid-IR band in the 1580-1640 cm^{-1} range upon EtOH adsorption, which intensifies with temperature (CARVALHO *et al.*, 2013; CHIEREGATO *et al.*, 2015; TAIFAN *et al.*, 2017a). CARVALHO *et al.* (2013); YOUNG *et al.* (2016) claim that this band is related to the formation of surface carboxyls (acetate-like species) on basic surface sites through the Cannizzaro reaction, Figure 2.9. The authors attribute the presence of these species to the asymmetric stretching vibrations of C=O bonds. However, the doublets associated with symmetrical stretching (1300-1450 cm^{-1}) of the same bonds were not observed in DRIFTS experiments reported by PACHECO (2019). Another study suggested that the band at 1587 cm^{-1} corresponds to C=C stretching in BD adsorbed on defective surface sites (TAIFAN *et al.*, 2017a), although this hypothesis lacks experimental support.

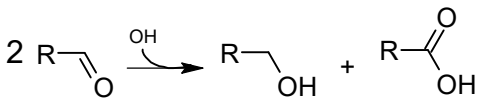

Figure 2.9: Cannizzaro Reaction

The substitution of Mg^{2+} by other divalent cations on Mg_xAlO_y catalysts usually increases the number of acid sites and improves the dehydrogenation activity (JABŁOŃSKA *et al.*, 2017). MARCU *et al.* (2013) studied the EtOH conversion

into BuOH over $M_zMg_{x-z}AlO_y$ (M=Pd, Ag, Mn, Fe, Cu, Sn, or Yb). Cu- and Pd-based catalysts were the most active in terms of EtOH conversion and BuOH selectivity. For the first one, the reaction main products were BuOH and 1,1-diethoxyethane, while the latter was quite selective to BuOH. For the $Cu_zMg_{x-z}AlO_y$ catalysts, with increasing z, the number of basic sites decreased while the BuOH selectivity decreased. This correlation suggests that BuOH formation can be linked with the number of basic sites. The authors inferred that AcO self-condensation, catalyzed by basic sites, would be the RDS of the transformation of EtOH into BuOH. Other authors utilizing $Cu_{0.1}Mg_{x-0.1}AlO_y$ with a ratio of basic and acid sites equal to 1.55 also confirmed that the catalyst's amphoteric property is important. In that catalyst, EtOH dehydrogenation to AcO occurs on weak/medium basic sites, whereas aldolization of aldehydes takes place on medium to strong basic sites. Dehydration and hydrogenation, in turn, take place at acidic sites and transition metal sites, respectively, resulting in the formation of BuOH (RECHI SIQUEIRA *et al.*, 2019). A similar behavior was observed by PACHECO *et al.* (2019), who investigated Ru-Mg_xAlO_y catalysts and found that, despite the increase in EtOH conversion, the presence of Ru redirected the reaction pathway toward methane formation, thereby reducing the selectivity to coupling products such as BuOH and BD.

VIKÁR *et al.* (2023) has investigated the effect of adding 1 wt % of metals (Pd, Pt, Ni, and Ru) to Mg_xAlO_y on the catalytic performance. The incorporation of these metallic components was intended to promote the hydrogenation and dehydrogenation steps. Among the catalysts evaluated, Pd/Mg_xAlO_y exhibited the most favorable performance. At 523 K, the conversion of EtOH in an atmosphere of He increased from 3 % to 22 % with the use of the Pd-containing catalyst. However, selectivity towards BuOH decreased from 80 % to 65 %, accompanied by an increase in the formation of gaseous products such as CH_4, CO and CO_2, which was attributed to enhanced decarboxylation and decarbonylation reactions. At 623 K, the yield of BuOH decreased significantly (to less than 20 %) due to the intensification of these secondary reactions. This behavior has been attributed by the authors to the Pd promoting effect, which facilitates both the initial dehydrogenation of EtOH and the final hydrogenation of unsaturated intermediates through MPV. A similar behavior was observed by PACHECO *et al.* (2019), who investigated Ru-supported catalysts on MgO and Mg_xAlO_y and found that, despite the increase in ethanol conversion, the presence of Ru redirected the reaction pathway toward methane formation, thereby reducing the selectivity to coupling products such as BuOH and 1,3-butadiene.

Another important aspect of the VIKÁR *et al.* (2023) study is the use of H_2 instead of He in the inlet stream. In a dihydrogen atmosphere, there was

a reduction in EtOH conversion at mild temperatures (473 K), but it increased significantly at elevated temperatures (523 K). This suggests that the involvement of H_2 in hydrogen transfer reactions is influenced by the temperature-dependent hydrogenation–dehydrogenation equilibrium. At slightly higher temperatures, the equilibrium begins to shift towards dehydrogenation products. Furthermore, DRIFTS results demonstrated that the active metal facilitated H transfer from H_2 within the narrow temperature range of 473-523 K, where the equilibrium allowed significant concentrations of both dehydrogenated and hydrogenated products.

There is computational and experimental evidence that the conversion of EtOH to BuOH over MgO, Mg_xAlO_y, and HAP is structure-sensitive. The key question is how the design of these surfaces influences catalytic activity and selectivity, especially in pure MgO, where the highly dehydroxylated surface not only acts as a strong base but also exhibits reducing properties.

2.3 Structure-Activity-Selectivity Relationships

Over the decades, one of the most mentioned fundamentals in catalysis is that the catalyst's microstructure affects the activity, selectivity, and deactivation behavior. Designing the surface composition of the catalyst based on classic chemistry is only one of many strategic factors to enhance the catalytic performance. Sometimes the catalyst's effectiveness can be related to the particles' outer shape and average diameter (CIOLA, 1981). When it comes to the development of new catalysts, M. Boudart in 1969 was a pioneer in discussing the activity-structure relationship and how understanding structural differences is fundamental for the correct interpretation of the results of the studied reactions:

> "The rapidly growing list of facile reactions studied on a variety of supported metal catalysts suggests that, from now on, if specific rates are found to be markedly different on two different catalyst preparations, it is more important than ever to ascertain whether this difference really means that the reaction under study is structure-sensitive or can be ascribed to artefacts, metal-support interaction, incomplete reduction of the metal, or other causes." (BOUDART, 1969)

In a more modern perspective, the most active sites are associated with surface defects, which exhibit unusual geometric characteristics and/or distinct local chemical compositions. Crystals with perfectly periodic arrangements of all their structural elements cannot exist; in practice, real crystals contain various imperfections — commonly described as defects — which, could enhance catalytic

activity. These defects may be present in concentrations one or two orders of magnitude lower than regular sites (DAVYDOV, 2003b).

Defects primarily originate from at least three forms: (i) displacements of atoms from their lattice positions to interstitial sites, (ii) the presence of vacancies at specific lattice positions, or (iii) partial displacements of one crystal region relative to another along a crystallographic plane. These defects are usually classified based on their dimensions as point defects (vacancies, interstitial, or foreign atoms), line defects (dislocations), planar defects (shear planes and various internal and external grain boundaries), and spatial defects, such as pores or foreign inclusions (CHATTOT *et al.*, 2020; DAVYDOV, 2003b). For instance, besides being a strong base, the highly dehydroxylated surface of MgO also acts as a reducing agent. The reducing sites are apparently associated with defects, possibly cation vacancies on the surface, as the dissociative chemisorption of Brønsted acids blocks the reactivity of these reducing sites (DAVYDOV, 2003b).

Pure MgO is relatively simple compared to efficient commercial catalysts, which often incorporate a combination of metals supported on an oxide matrix. In the investigation of catalysts that do not contain active metals (as in this work), two fundamental aspects must be considered. First is the catalyst morphology, a characteristic that microscopically indirect reflects the change in the density of defective surface sites, as described by the third origin of defects in the previous paragraph. The second is the textural properties of this material, which can significantly influence diffusion features, affecting how reactants access the active sites during the reaction.

Although computational methods, such ones based on DFT, can predict model structures and correlate local structures with catalyst performance, successfully implementing these models on a real surface remains challenging. This is because (i) atomic-scale control is necessary, which is indeed extremely complex and computationally unfeasible regarding the design and synthesis of the surface structure, and (ii) characterization techniques are limited at the nanoscale, making atomic probing difficult. According to CHATTOT *et al.* (2020), this dichotomy between theoretical insights derived from well-defined atomic systems and the inherent complexity of a highly disordered real surface represents the core challenge in defect engineering. Regarding MgO, each surface atom has its own configuration and should be considered individually, as shown in Figure 2.10.

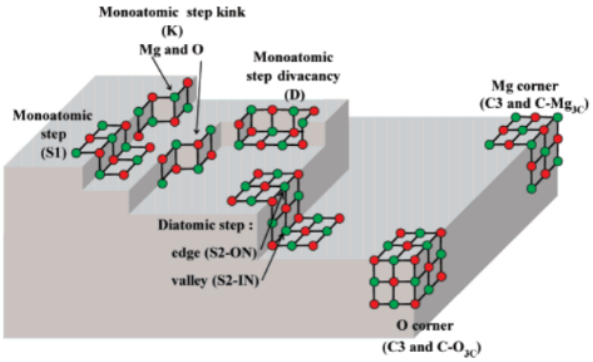

Figure 2.10: Representation of a surface (100) plane of MgO showing imperfections which provide sites for ions of low coordination
(O^{2-}, red spheres; Mg^{2+}, green spheres),
Source: CHIZALLET *et al.* (2007)

There are limitations between simulating a reaction at a specific defect site and subsequently preparing a catalyst that contains the same defects; however, the introduction and control of surface structure have proven to be effective strategies for enhancing catalytic activity. Defects in materials can be classified as either point or extended. Point defects, such as vacancies, interstitials, and substitutional atoms, can generate highly reactive unsaturated coordination sites. In contrast, extended defects, including dislocations and grain boundaries, can create regions with distinct electronic properties, which facilitate the adsorption and activation of reactants (LUO and WU, 2023). All of these defects modify the local electronic structure of the material and influence the surface reactivity.

The perfect MgO adopts the cubic structure B1, as illustrated in Figure 2.11a. This structure consists of two interpenetrating face-centered cubic sublattices (fcc), one anionic and one cationic, arranged alternately along the {111} planes. The unit cell is highlighted to show the three-dimensional arrangement of the Mg and O atoms. Figure 2.11 (b) and (c), in turn, depict dislocation slip systems, indicating typical Burgers vectors and the planes along which atomic shear occurs. These slip systems are directly associated with the presence of extended defects, such as dislocations, which can locally alter the symmetry and electronic density of the surface (AMODEO *et al.*, 2018).

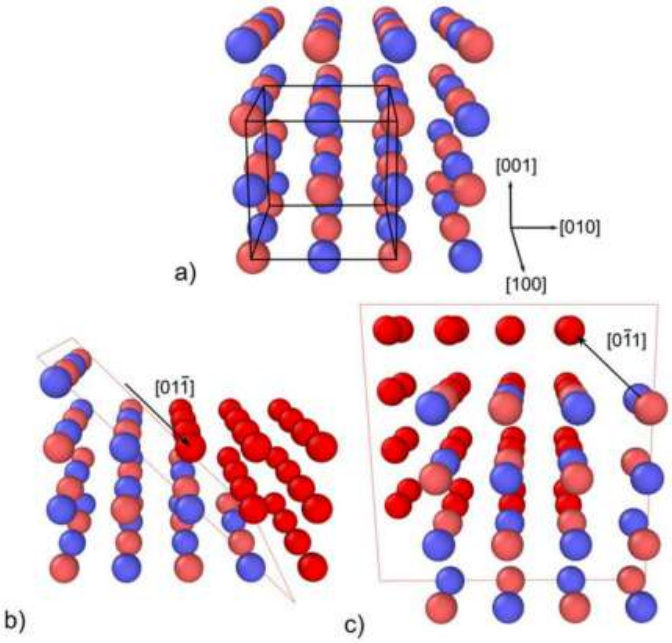

Figure 2.11: MgO crystal structure and slip systems

(a) Perspective view of the MgO crystal structure with the unit cell outlined in black and oriented along the cubic direction. (b) and (c) Illustrations of the shearing process for the $\frac{1}{2}\langle 110\rangle\{110\}$ and $\frac{1}{2}\langle 110\rangle\{100\}$ slip systems, respectively. Displaced atoms are shown in red. Black arrows indicate typical Burgers directions. *Source:* AMODEO *et al.* (2018)

As MgO defects play a key role in the catalytic performance of EtOH conversion to BuOH, it is essential that experimental characterizations identify practical descriptors that quantify and qualify their structural and electronic nature at the surface. These descriptors establish the link between the structure and catalytic activity.

2.4 Descriptors Estimated from Powder X-ray Diffraction (PXRD) Data

PXRD is a technique based on the elastic interaction of X-rays with the crystallographic planes of a polycrystalline sample, generating a characteristic diffraction pattern. This method enables the determination of structural parameters, the identification of crystalline phases, and the analysis of material purity, making it widely used in materials research (SCHLÖGL, 2009). Different phenomena associated with PXRD measurements influence the diffraction profile. Two cases can be highlighted here: (i) the shift of a peak to higher or lower Bragg angles along the x-axis and (ii) the broadening of diffraction peaks.

Figure 2.12 (a) and (b) illustrate the first case. On the left side of Figure 2.12 (a), a region of a grain is shown where the crystallographic planes remain

undeformed. These planes are parallel and maintain a regular spacing, denoted as d_0, representing the interplanar distance under equilibrium conditions, meaning no external stress or strain is applied. This spacing defines the angle at which diffraction ideally occurs, according to Bragg's Law. Otherwise, when the sample is subjected to a uniform tensile stress perpendicular to the reflection planes, the interplanar spacing increases, which, in practice, shifts the diffraction line to lower angles, as shown in Figure 2.12 (b). Under compression, the opposite effect occurs: the interplanar distance decreases, shifting the line to higher angles. Figure 2.12 (c), in turn, illustrates the second case, in which the deformation is non-uniform. This type of deformation causes peak broadening because each portion of the diffracted plane exhibits a slightly different interplanar spacing, as shown on the left side of the Figure 2.12 (c). This results in the superposition of multiple individual contributions from the same plane, widening the diffraction peak (KHORSAND ZAK *et al.*, 2011; RAMGIR *et al.*, 2006).

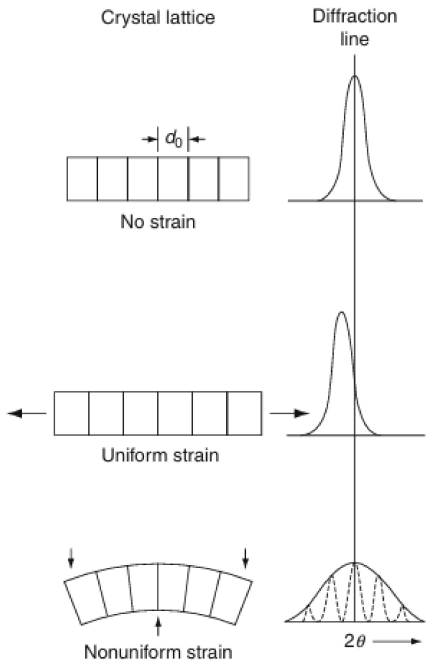

Figure 2.12: Portion of an unstrained grain appears in (a), uniform tensile strain (b), and nonuniform strain (c)

Notes: Uniform strain affects the peak position, and the nonuniform strain affects the peak broadening and intensity.

*Source:*KHORSAND ZAK *et al.* (2011); SCHLÖGL (2009)

The non-uniform deformation is not the only factor responsible for peak broadening. Other sample-related effects also contribute, such as crystallite size,

solid solution inhomogeneity, and temperature variations. In addition to these intrinsic contributions from the sample, instrumental broadening must also be considered, originating from both the monochromaticity of the incident X-ray beam and the optical system of the instrument (such as slit spacing and positions, detector pixel size, etc.). If there were no such instrumental influence, a sufficiently large and highly ordered lattice plane would produce a diffraction pattern very close to a Dirac delta function, which is not observed in practice. The instrumental contribution changes the Dirac's theoretical profile of Bragg peaks into a Gaussian, while the sample contribution tends toward a Lorentzian distribution (CHATTOT *et al.*, 2020).

In order to separate the instrumental contribution from the sample-related broadening (β_{measured}), a diffraction pattern of a reference material, such as silicon, must be collected to determine the instrumental broadening ($\beta_{\text{instrumental}}$) (ROGERS and DANIELS, 2002), as follows in Equation 2.1.

$$\beta_D = \left(\beta^2_{\text{measured}} - \beta^2_{\text{instrumental}}\right)^{\frac{1}{2}} \tag{2.1}$$

Thus, it is possible to obtain the average crystallite size of a sample using the well-known Scherrer equation SCHERRER (1918), as shown in Equation 2.2:

$$\cos\theta = \frac{K\lambda}{D}\frac{1}{\beta_D} \tag{2.2}$$

where D represents the average crystallite-size descriptor, K is a dimensionless constant that depends on the crystal shape (typically $K \approx 0.9$), λ is x-Ray wavelength — in this case, $\lambda_{CuK_{\alpha 2}} = 0.15444$ nm —, β_D is the previously corrected Full Width at Half Maximum (FWHM) of the diffraction peak in radians, and θ is the half of the respective Bragg's angle, also in radians.

2.5 Synthesis of Hierarchical MgO by Hydro- and Solvothermal Methods

The hydrothermal technique has historical roots in the geological sciences and was first mentioned by the British geologist Sir Roderick Murchison in the 19th century (FENG and LI, 2017). Since then, extensive studies have been conducted to comprehend the formation of new materials, develop novel hydrothermal methods, and understand reaction mechanisms.

Hydrothermal synthesis is a process for producing small particles and heavily relies on the ability of species to dissolve in hot water under high pressure. The crystal growth occurs within a high-pressure steel container called an autoclave

(KAFLE, 2020). The main advantage of this method lies in its closed and easily controlled system. Furthermore, the method is advantageous due to its ability to operate without the need for supervision during synthesis, which results in significantly lower experimental effort compared to traditional methods, such as precipitation and sol-gel. The hydrothermal method involves the production of materials through chemical reactions in an aqueous solution above the boiling point of water, while the solvothermal method takes place in a non-aqueous solution at relatively high temperatures, less than 473 K.

In the realm of crystal growth processes, an understanding of reaction kinetics and the crystal growth mechanism of the hydrothermal method is of paramount importance. The hydrothermal method, renowned for its applicability in synthesizing a diverse array of crystals, entails intricate steps that orchestrate the emergence of well-formed crystals. YANG and PARK (2019) outined the main steps of crystalline growth under hydrothermal conditions are as follows:

- **Step 1:** Reactants dissolve in a hydrothermal medium, forming ions or molecular groups in the solution.
- **Step 2:** Temperature differences cause migration of ions or molecules towards cooler regions, leading to seed crystal growth and supersaturated solution formation.
- **Step 3:** Ions or molecules adsorb, decompose, and desorb at the growth interface.
- **Step 4:** Adsorbed material moves at the interface.
- **Step 5:** Dissolved matter crystallizes, giving rise to the final crystal.

The reaction media plays a crucial role in any hydrothermal or solvothermal system as it exhibits remarkable characteristics when exposed to supercritical conditions. While organic solvents are used in these syntheses, water remains the more popular choice due to its environmentally friendly nature and cost-effectiveness. However, it is important to note that under high temperatures and high pressure, water's solvent properties undergo significant alterations. These alterations cause water's density, surface tension, and viscosity to decrease, while its vapor pressure and ion product increase. This underscores the need for a thorough understanding of how these changes impact the overall reactions in hydrothermal and solvothermal systems (FENG and LI, 2017; RABENAU, 1985).

A hydrothermal system exhibits three key features: i. acceleration of the reaction rate among complex ions; ii. intensification of the hydrolysis reaction; and iii. significant changes in the redox potential of the reactants. Generally, there

are two extreme types of basic chemical reactions. The first one involves ionic reactions, including the metathesis reaction of inorganic materials, which can be rapidly conducted at ambient temperatures. The second is free radical reactions, such as explosive reactions of organic compounds. According to the electronic theory, reactions of organic compounds with polar bonds usually exhibit characteristics of the first type. When water is used as medium and the reaction system is heated above its boiling point. in a sealed reactor, the ionic reaction rate is accelerated. This is in line with Arrhenius' equation: $\frac{d\ln k}{dT} = \frac{E}{RT^2}$, where the reaction rate constant k exponentially increases with the rise in reaction temperature (FENG and LI, 2017). As the temperature increases, the ionization constant of water also increases. Consequently, the ionic or hydrolysis reaction of indissolvable inorganic materials, at ambient temperature or organic compounds, can be promoted under high-temperature and high-pressure hydrothermal conditions.

In hydrothermal synthesis, besides water acting as a solvent, it can also be part of the reactants since, depending on the temperature and pressure, it can essentially exist in the form of H_3O^+ and OH^-, altering the chemical and physical properties of the reactants and products, thus accelerating the reaction. On the other hand, in solvothermal synthesis, a variety of organic solvents are used as the reaction medium, providing room for new products. As well as the polyol-mediated synthesis, these solvents not only serve as the reaction medium but also dissolve or partially dissolve the reactants, forming reactant-solvent complexes that affect the reaction rate. Additionally, the choice of the organic solvent can influence the concentration and state of the active species of the reactants, leading to changes in the reaction process. Various molecular and empirical parameters, such as molecular weight, density, melting point, boiling point, molecular volume, heat of evaporation, dielectric constant, dipole moment, and solvent polarity, are considered in selecting the appropriate solvent for solvothermal synthesis (FENG and LI, 2017; RABENAU, 1985).

The synthesis of ultrafine MgO nanowires by the hydrothermal method was reported by AL-GHAMDI *et al.* (2012). Figure 2.13 presents the MgO prepared in that work, showing a flower morphology. Similarly, in the study reported by HADIA and MOHAMED (2015), using water and EtOH as solvents, MgO nanowires were prepared via the solvothermal method. Figure 2.14 displays the prepared MgO, exhibiting a nanowire morphology.

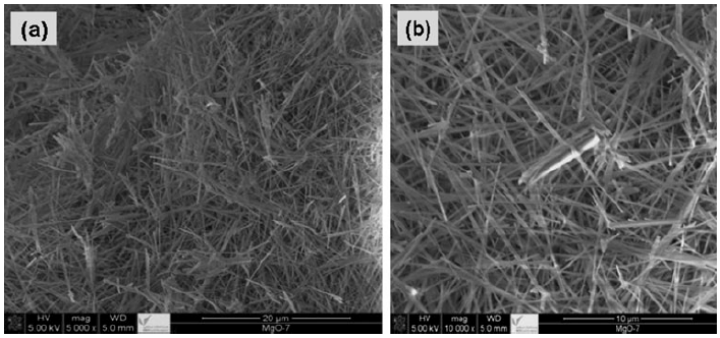

Figure 2.13: SEM images of MgO nanowires (a) 5000×, e (b) 10,000×
Source: AL-GHAMDI *et al.* (2012)

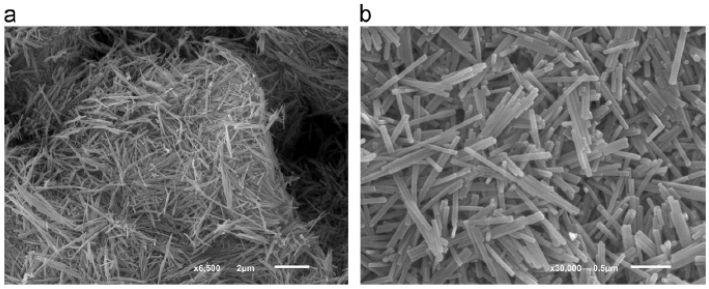

Figure 2.14: SEM images of MgO nanowires (a) 6500×, e (b) 30,000×
Source: HADIA and MOHAMED (2015)

In addition to nanowire morphologies, as a final example, LEE *et al.* (2020) reported the preparation of MgO hollow microspheres in the form of flowers, using Polyvinylpyrrolidone (PVP) as a structure-directing agent and Ethylene Glycol (EG) as the reaction medium. The authors claim that the flower-shaped structures consist of ultrathin nanolaminates with a large surface area, providing excellent access for reactants to the catalytic sites, as illustrated in Figure 2.15.

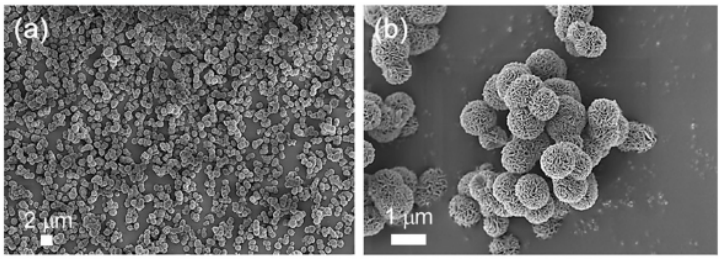

Figure 2.15: SEM images of hollow MgO flower-shaped microspheres (a) 10,000×, e (b) 30,000×

*Source:*LEE *et al.* (2020)

Despite the fact that particles obtained through hydrothermal and solvothermal methods are relatively large (several hundred nanometers) and exhibit different morphologies in micrographs, it is observed that the crystallites are often small.

For instance, GURULE *et al.* (2025) estimated, using only the Scherrer method, that MgO particles synthesized through hydrothermal and sol-gel methods have crystallite sizes ranging from 14.8 nm to 31.3 nm.

In summary, hierarchical MgO-based materials exhibit locally distinct structures that are still somewhat unexplored in catalysis. Additionally, associating surface catalytic phenomena with easily estimable local descriptors remains a challenge. Therefore, the development of analytical methods for microscopic probing may serve as a bridge to relate catalytic performance to local activity.

2.6 Synchrotron-radiation-based Infrared Nanospectroscopy (SINS)

Classic spectroscopic techniques for analyzing catalysts, such as IR, ultraviolet-visible, and Raman spectroscopy, offer valuable information about the catalytic phenomena. However, their spatial resolution is restricted to the micrometer scale, limiting the ability to examine reactions at a smaller, more localized level (WU *et al.*, 2017). Near-field microscopy techniques can surpass these diffraction limitations by confining light-matter interactions to small spatial scales. The antenna effect in s-Scanning Near-Field Optical Microscopy (s-SNOM) enables the confinement of free-space electromagnetic waves into nano-sized volumes, employed as a light nanoprobe, as depicted in Figure 2.16. As a result, the IR light gets focused towards a metallic tip of an Atomic Force Microscopy (AFM) instrument, causing polarization through the electric field it encounters.

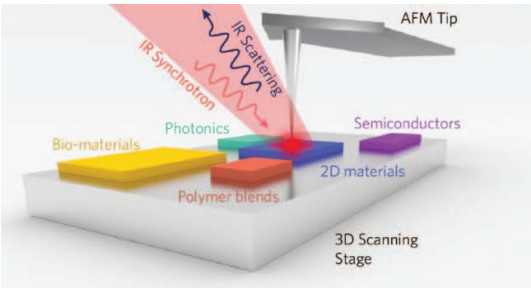

Figure 2.16: 3D representation of the s-SNOM and synchrotron nano-Fourier transform infrared (FTIR)

Source: FREITAS *et al.* (2017)

SINS improves chemical contrast and spectroscopic identification in nano-FTIR by utilizing bright and spatially coherent IR synchrotron radiation as a source for IR scattering measurements (BECHTEL *et al.*, 2014; HERMANN *et al.*, 2014; WU *et al.*, 2017). Synchrotron light is highly intense, much brighter than conventional light sources, making it extremely valuable for experiments that require high

sensitivity. Additionally, light from a synchrotron source has high brightness, which is the combination of its intensity and reduced focal size, enabling high-resolution imaging and detailed spectroscopic experiments. Thus, integrating near-field IR methods with synchrotron IR makes it possible to achieve highly precise chemical and quantum-state imaging with a spatial resolution of less than 25 nm. This combination allows for sensitive detection of molecular or phonon vibrational characteristics across the mid- to far-IR spectral range (BECHTEL *et al.*, 2020).

The light from the synchrotron source passes through a series of mirrors to extract the broadband IR, which is then focused and collimated. In SINS configuration, the quasi-parallel IR beam is coupled to a commercial s-SNOM apparatus, as shown in Figure 2.17. The broadband IR collimated beam goes into an asymmetrical Michelson interferometer. The Michelson interferometer employs a beam splitter to divide the light beam into two separate paths. Its functioning involves two primary actions: firstly, it splits the incoming light beam, and then it enables the interference between the incident light beam and the beam that interacted with the sample, merging them before reaching the detector. In the final arm of the interferometer, there's a stage referred to as s-SNOM, where the incident light beam is directed back as a backscattered beam right after its interaction with the sample. In the s-SNOM stage, the IR light is focused onto an AFM tip, enabling radiation confinement below the diffraction limit at its tip. The sample is placed on a piezoelectric device for AFM scanning, covering areas of 100 μm by 100 μm with a minimum step size of 5 nm. In this way, both topography (AFM) and optical signals (s-SNOM) are detected at the same time. In order to suppress unwanted background signals, the AFM is operated in tapping mode, where the tip is oscillating normal to the sample at a frequency Ω (MESTER *et al.*, 2020).

The utilization of higher harmonics of the tip motion in optical measurements significantly impacts the results' precision and spatial resolution. By demodulating at higher tip harmonics, it becomes possible to suppress far-field background and minimize undesired interferences from the surrounding environment, leading to improved spatial resolution (RICHARDS *et al.*, 2004). In addition to utilizing higher tip harmonics, an asymmetric interferometer introduces optical phase sensitivity in the s-SNOM detection. This sensitivity arises from the fact that only the tip-sample arm carries the phase delays caused by sample dispersion or absorption. Consequently, interferograms are obtained using a method similar to standard FTIR, followed by Fourier transform processing to reconstruct broadband amplitude ($s(\omega)$) and phase ($\varphi(\omega)$) spectra. A graphical representation of this process can be seen at the bottom of Figure 2.17 (FREITAS *et al.*, 2017).

Note that the collected output — amplitude $s(\omega)$ and phase $\varphi(\omega)$ spectra — are not necessarily the absorption measurements as a function of wavenumber

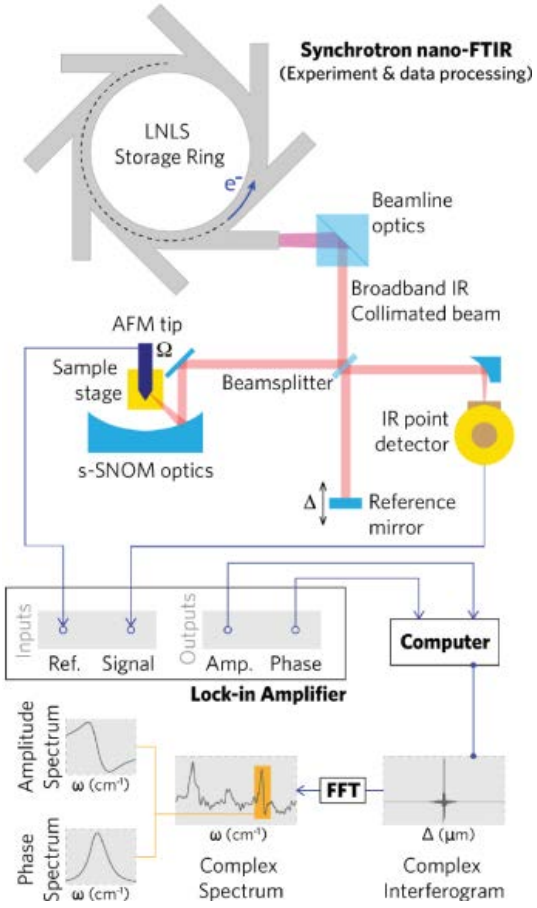

Figure 2.17: Synchrotron nano-FTIR experimental scheme from measurement to data processing.

*Source:*FREITAS *et al.* (2017)

associated with conventional far-field FTIR. In this sense, HUTH *et al.* (2012) and other authors, claim that the phase spectrum, in fact, carries the infrared absorption properties of the sample (BREHM *et al.*, 2006; POLLARD *et al.*, 2014; TAUBNER *et al.*, 2004; XU *et al.*, 2012). For example, experiments with Si_3N_4 nanoislands conducted by STIEGLER *et al.* (2011) indicate that the near-field IR phases ($\Im[\sigma_n(\omega)]$) spectra of small particles exhibit a significant correlation to the far-field absorption A. Here, as performed by HUTH *et al.* (2012), we define the Huth's identity of the nano-FTIR as a second harmonic point spectrum as:

$$a_2 \equiv \Im[\sigma_2(\omega)] \propto A \tag{2.3}$$

where σ is the scattering coefficient. With this identity, it is possible to interpret the vibrational aspects of near-field phase IR spectra in exactly the same way as it is done for conventional FTIR spectra, as illustrated in Figure 2.18[1].

[1]The schematics to the right of the spectra illustrate nano-FTIR and standard transmission FTIR

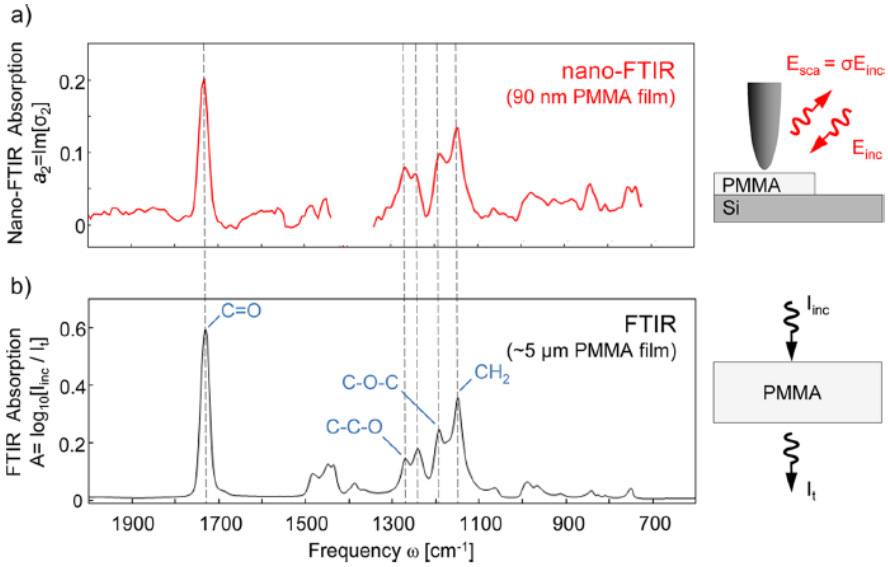

Figure 2.18: Comparison of nano-FTIR with conventional far-field FTIR of poly(methyl) methacrylate

Source: HUTH *et al.* (2012)

SINS technique is evolving in the field of catalysis. This is because most studies offer perspectives on samples prepared exclusively for SINS measurement, which often differ from real catalysts. However, preliminary investigations have been conducted on the use of these techniques in catalysis, particularly in the study of interface processes involving molecular monolayer samples. Recently, LI *et al.* (2023) published a focused review on the use of nano-IR AFM in catalysis. The authors claim that achieving (sub)monolayer sensitivity is a fundamental requirement for investigating catalytic processes. The interaction of near-field IR with finite chemical bonds between the AFM tip and the catalyst is relatively weak, which poses a challenge for the detection limits of detectors in this type of technique. However, one way to overcome this is by using a synchrotron source, such as SINS.

By implementing these unconventional synthesis methods and leveraging the SINS technique, we expect to make significant contributions to advancing our knowledge in heterogeneous catalysis. This will not only fill the identified scientific gap but also bring fresh perspectives to understanding the intricate relationship between MgO-structure and catalytic performance in the EtOH to BuOH conversion process.

2.7 Proposal for Contribution and Approach

Based on the discussions presented in this chapter, it becomes evident that a scientific gap must be addressed: the lack of experimental evidence supporting the relationship between the structure of pure MgO and its catalytic performance in the

conversion of EtOH to BuOH. To address this issue, the development of hierarchical MgO catalysts is proposed using two non-conventional synthesis methodologies described in this review: the hydrothermal and solvothermal methods.

The expectation is that the prepared catalysts will exhibit distinct diffraction profiles, allowing several differences in the broad peak and position. It is important to emphasize that, because structural properties are calculated as an average over the entire catalyst (i.e., spatial resolution is lost as the measurements are performed in the bulk), descriptors such as microstrain and average crystallite size do not reveal the specific nature of active sites but provide statistical insights into the emergence of overall structural disorder.

In addition to conventional characterization techniques, such as PXRD, N_2 physisorption, and in-situ DRIFTS-MS, there is an opportunity to explore a less commonly used technique in catalysis, known as SINS. This approach will allow for a more precise investigation of the influence of catalyst morphology on the conversion of EtOH to BuOH, enabling a detailed analysis at the local level.

In contrast to this study, which employs real MgO-based catalysts with complex polycrystalline surfaces, the literature has presented few studies using the SINS technique in catalysis, typically limited to model surfaces specifically prepared to enable measurement and interpretation of spectroscopic data. For example, WU *et al.* (2017) have employed a model surface (100 ± 30 nm), obtained by evaporation of a metallic Pt film, consisting of a Pt(200) layer on a Si(110) substrate, to investigate the reactivity of peripheral regions of Pt crystallites using SINS, before and after functionalization with N-heterocyclic carbenes. In the present work, the main challenge is to apply the SINS technique to a material with a highly complex surface, which imposes significant limitations. The first expected limitation is associated with the particle topography: since AFM provides height information, variations in local height can lead to differences in the intensity of the phase-resolved spectral signal. The second limitation arises from the polycrystalline nature of the surface, which prevents the precise identification of the exposed crystal facets. Given that different facets may exhibit distinct reactivities, this uncertainty hinders the consistent interpretation of the spectra because it is not possible to unambiguously assign the observed bands to specific surface sites.

By employing these non-conventional synthesis methodologies and utilizing the SINS technique, it is expected to contribute significantly to the advancement of knowledge in catalysis. This will not only address the identified scientific gap but also provide new perspectives for understanding the relationship between morphology and catalytic performance in the conversion of EtOH to BuOH over a real surface. This in turn could shed light onto future tunings in the material synthesis in order to achieve more active and selective catalysts.

Chapter 3

Methods

3.1 Catalyst Preparation

The MgO catalysts evaluated in this work were obtained via three distinct methods: (i) precipitation, (ii) solvothermal, and (iii) hydrothermal. All reagents are listed in Table 3.1. Notably, after preparing the catalyst precursors —as described in the following subsections — all materials underwent the same thermal treatment: using an electric furnace, the MgO precursors were thermally treated under air (GHSV = 0.25 mL min^{-1} mg_{cat}^{-1}) at 723 K for 3 h with a heating rate of 1 K min^{-1}. After it, all catalysts were sized to 106 µm – 180 µm.

Table 3.1: Chemicals used in the syntheses

Reactant	Chemical formula	Manufacturer	Purity / %	Molar weight / g mol^{-1}
Magnesium nitrate hexahydrate	$Mg(NO_3)_2 \cdot 6H_2O$	Sigma-Aldrich	>98.0	256.41
Magnesium acetate tetrahydrate	$Mg(CH_3COO)_2 \cdot 4H_2O$	Sigma-Aldrich	>98.0	214.45
Potassium hydroxide	KOH	Merck	>97.0	56.11
Polyvinylpyrrolidone (PVP)	$(C_6H_9NO)_n$	Sigma-Aldrich		average mol wt 40,000
Urea	NH_2CONH_2	Sigma-Aldrich	>99.0	60.06
Ethylene Glycol (EG)	$HOCH_2CH_2OH$	Dinâmica	>99.0	76.09
Ethanol	CH_3CH_2OH	ChemLab	>99.0	46.07
Distilled water	H_2O	-	-	18.0

3.1.0.1 Precipitation — MgO-p (MgO with no defined morphology)

The first catalyst, MgO-p, was prepared by conventional precipitation, as described in the literature (CHIEREGATO *et al.*, 2015; DI COSIMO *et al.*, 1998, 2000). First, 15.39 g of $Mg(NO_3)_2{\cdot}6H_2O$ were dissolved in 100 mL of distilled water (Solution A). Then, Solution A and a second aqueous solution of 1 M KOH (Solution B) were gradually added to a beaker containing 50 mL of water while maintaining pH 10. The system was kept under magnetic stirring on a hot plate at 333 K for 40 min. After this step, the solid was vacuum-filtered and washed with distilled water to remove excess K^+. The solids exhibited a gelatinous appearance, typical of

highly hydrated hydroxides, and a white color. Subsequently, the solids were dried in a static air oven at 393 K for 12 h to remove surface water. The MgO precursor grain size was reduced using mortar and pestle.

3.1.0.2 Solvothermal — MgO-f (Flower-like MgO)

The second method was solvothermal, as reported by LEE *et al.* (2020). The MgO catalysts obtained by this method exhibited spherical structures with flower-like morphology. In a beaker, 14.4 g of PVP and 9.63 g of $Mg(CH_3COO)_2 \cdot 4H_2O$ were dissolved in 600 mL of EG. The resulting transparent solution was transferred to a 1 L Teflon-lined stainless-steel autoclave. The autoclave was placed in an oven at 463 K for 20 h. Then, the yellowish-white product was collected by centrifugation. The product was washed three times with EtOH and dried in an oven at 323 K. Finally, grinding was performed with a mortar and pestle. The obtained MgO precursor was magnesium glycolate with a flower-like morphology.

3.1.0.3 Hydrothermal — MgO-w (Wire-like MgO)

The last method was hydrothermal, described by AL-GHAMDI *et al.* (2012). The catalysts obtained by this method exhibited nanowire-like structures. First, 6.44 g of $Mg(CH_3COO)_2 \cdot 4H_2O$ were dissolved in 75 mL of distilled water, and the mixture was stirred for 30 min at room temperature. Then, a solution of 1.2 g of urea in 25 mL of distilled water was slowly added to the $Mg(CH_3COO)_2 \cdot 4H_2O$ solution under vigorous stirring for another 30 min. 60 mL of the resulting mixture were transferred to a 100 mL Teflon-lined stainless-steel autoclave. The autoclave was sealed and maintained at 453 K for 2 h. After this period, the autoclave was cooled to room temperature. The products were obtained by centrifugation and washed at 10000 rpm in three cycles of 10 min each. To minimize agglomeration, the products were washed with distilled water in the first two cycles and then with EtOH. The MgO precursor was obtained after drying at 333 K overnight in static air. Grinding was performed with a mortar and pestle.

3.2 Catalyst Characterization

3.2.1 Powder X-ray Diffraction (PXRD)

The crystalline structures in the studied oxides were identified by X-ray diffraction (XRD), after the heat treatment. A Rigaku Miniflex diffractometer was used, with Cu radiation (CuKα_1, $\lambda = 1.5444\,\text{Å}$). The diffractograms were obtained in the 2 $^\circ \leq 2\theta \leq 90^\circ$ range with a step of 0.05 $^\circ$ in continuous scan mode. All

samples were analyzed without prior pretreatment. Before being analyzed, the raw data were subjected to pretreatment. MDI Jade software v.5.0.37 (SP1) was used to process the data and compare the crystallographic information with the Joint Committee on Powder Diffraction Standards (JCPDS) database. This allowed for the identification and confirmation of the crystalline phases.

3.2.2 Thermogravimetric Analysis (TGA)

Thermogravimetric Analysis (TGA) was performed using a Rigaku Thermo Plus TG 8120 instrument under an inert N_2 atmosphere (30 $cm^3 \cdot min^{-1}$). The samples were heated from 298 K to 773 K at a rate of 20 $K \cdot min^{-1}$, followed by a 2 h isothermal step at 773 K. Subsequently, cooling was carried out down to 673 K at the same rate, with an additional 15 min isothermal step. The experimental conditions were identical to those used prior to the catalytic test, except for space velocity and atmosphere composition.

3.2.3 Scanning Electron Microscopy (SEM)

SEM images were obtained using a Versa 3D Dual Beam FEI microscope operated at 15 kV. Samples were prepared by spreading the dry powder over the silicon wafer and then drying it under ambient conditions.

The size of structured particles, such as diameter and width, was measured using ImageJ 1.51j8 software. Finally, the data were statistically analyzed using the `Scipy`[1] package in `Python 3.10`.

3.2.4 N_2 Physisorption

The determination of the specific area, the average diameter and the pore volume was made by physisorption of N_2 at 77 K in a Micromeritics ASAP 2020. Approximately 200 mg of sample mass was used for all samples. All catalysts underwent a pretreatment step to remove moisture. In this procedure, the materials were subjected to a vacuum of 1.10^{-6} mmHg at 573 K for 24 h. Subsequently, the adsorption and desorption isotherms were obtained by plotting the amount of physisorbed N_2 as a function of the N_2 partial pressure. With these curves, specific areas were estimated using the Brunauer-Emmett-Teller (BET) and t-plot models, whereas the average diameter and pore volume were calculated by the Barret-Joyner-Halenda (BJH) approach.

[1] https://www.scipy.org/

3.3 Catalytic Tests

A Gas Chromatograph Shimadzu 2014 with an FID detector and Ar as the carrier gas was used for the bench-scale experiments. All species were detected online using a Porabond Q column (50 m, 0.32 mm internal diameter). Anhydrous EtOH (Sigma-Aldrich, >99.5 %) was fed into the system using a bubbler. In order to maintain both the flow rate and the molar fraction of the 5% EtOH:Ar constant, the bubbler bath temperature was kept at 283 K. This temperature was calculated using the Antoine equation (Equation 3.1) in conjunction with Raoult's law and the ideal gas assumption.

$$p_{\mathrm{EtOH}} = 10^{\left(A - \frac{B}{T+C}\right)} \tag{3.1}$$

where p_{EtOH} represents the vapor pressure of EtOH, and A, B, and C are the Antoine constants, with values of 5.37, 1670.41 K^{-1}, and -40.19 K, respectively.

The reactions were carried out in a U-shaped quartz reactor with an internal diameter of 8 mm. In all experiments, catalyst mass and pressure were maintained at 50 mg and 1.1 bar, respectively. The testing protocol begins with a pretreatment at 773 K, with a heating rate of 10 K min^{-1} and a duration of 2 h, using a pure Ar flow. The reactor is cooled to reaction temperature, initiating the test by switching the valve to an inlet flow 5 % EtOH. After 15 min, the first Gas Chromatography (GC) run is made at Time-on-stream (TOS) = 0 h. The experimental design presented in the following (Table 3.2) details the remaining variables.

Table 3.2: Experimental Planning

Test #	Catalyst	T	τ (GHSV^{-1})	T / K	τ / min $\mathrm{g_{cat}}$ cm^{-3}
1 (DT)	p	+1	-1	723	0.8
2 (DT)	p	+1	-1/2	723	1.3
3 (DT)	p	+1	1/2	723	1.5
4 (DT)	p	+1	1	723	2.5
5	p	-1	1/2	648	1.5
6	f	-1	1/2	648	1.5
7	w	-1	1/2	648	1.5
8	p	0	1/2	673	1.5
9	f	0	1/2	673	1.5
10	w	0	1/2	673	1.5
11	f	0	1/2	723	1.5
12	w	0	1/2	723	1.5

The first four experiments, referred to as diffusional tests (DT), aimed to investigate the operating regime by varying the space-time at three levels while keeping the highest working temperature (723 K) constant. These tests in turn guided the experimental conditions for the other ones, as an optimal catalyst assessment operates at kinetic regime (vide infra).In the remaining tests, temperature was the primary variable, also studied at three levels, while the other conditions remained constant. EtOH conversion (X_{EtOH}) is given by

$$X_{\mathrm{EtOH}} = \frac{A^{\mathrm{in}}_{\mathrm{EtOH}} - A^{\mathrm{out}}_{\mathrm{EtOH}}}{A^{\mathrm{in}}_{\mathrm{EtOH}}} \times 100 \tag{3.2}$$

where $A^{\mathrm{in}}_{\mathrm{EtOH}}$ is the area of the EtOH peak measured bypassing the reactor and $A^{\mathrm{out}}_{\mathrm{EtOH}}$ is the EtOH peak area measured from the reactor outlet. Furthermore, the specific conversion was also calculated as the EtOH conversion normalized by catalyst specific area (S_s), $X_{\mathrm{specific}} = \frac{X_{\mathrm{EtOH}}}{100 \cdot w \cdot S_s}$. This was done to ensure that a fairer comparison could be done among the catalyst. As it is not possible to quantify the actual active sites in the tested catalysts, weighting the results by the area of the materials was the normalization of choice. The selectivity for each product i was calculated as follows.

$$S_i = \frac{A^{\mathrm{out}}_i}{f_i \times Mw_i} \left(\sum_{i=1}^{N} \frac{A^{\mathrm{out}}_i}{f_i \times Mw_i} \right)^{-1} \times 100 \tag{3.3}$$

where A^{out}_i is the peak area of each product in the chromatograms, f_i is its response Flame Ionization Detection (FID) factor (DIETZ, 1967), and Mw_i is the molecular weight of the product. Thus, the specific yield ($\mathrm{Y}_i = \mathrm{X}_{\mathrm{specific}} \cdot \frac{S_i}{100}$) is defined, representing the rate of product formation per unit area of the catalyst. The observed rates of the product i at each temperature j were calculated according to Equation 3.4.

$$r^{obs}_{i,j} = \left(\frac{\hat{A}^{\mathrm{out}}_{i,j}}{\sum_i \hat{A}^{\mathrm{out}}_{i,j}} \right) \cdot \frac{X_{\mathrm{EtOH}} \cdot \dot{n}^{\mathrm{in}}_{\mathrm{EtOH}}}{w \cdot S_s} \tag{3.4}$$

The term $\dot{n}^{\mathrm{in}}_{\mathrm{EtOH}}$ represents the reactor inlet EtOH molar flow (mol s^{-1}), w is the catalyst mass (g), and S_s is the specific surface area ($\mathrm{m}^2\,\mathrm{g}^{-1}$). Moreover, the notation with hat in the area of each peak indicates that these have been corrected for by their respective factor FID and molar mass. After that, non-linear regression was performed using the `curve_fit` function from the Scipy library. The optimization was based on minimizing the sum of squared residuals between the observed (r^{obs}_j) and predicted (r^{pred}_j) values. The objective function was defined as follows:

$$S(\boldsymbol{\theta}) = \min_{\boldsymbol{\theta}} \sum_{j=1}^{N} \left(r_j^{obs} - r_j^{pred}(T_j, \boldsymbol{\theta}) \right)^2, \tag{3.5}$$

where $\boldsymbol{T}$ = [648, 673, 773] K represents the independent variable, and $\boldsymbol{\theta}$ is the parametetric vector optimized by the Levenberg-Marquardt algorithm, the default method in the `curve_fit`. The coefficient of determination (R^2) was calculated to evaluate the quality of the fit.

3.4 In-Situ Diffuse Reflectance Infrared Fourier Transform Spectroscopy with Mass Spectrometry (DRIFTS-MS)

DRIFTS technique enables monitoring of changes on the catalyst surface following the adsorption and desorption/reaction of a probe molecule, in this case EtOH. The MS technique was performed at the DRIFTS chamber outlet, allowing online identification of reaction products.

A Perkin Elmer Spectrum 100 FTIR spectrometer was used with a Harricks Praying Mantis diffuse reflectance accessory, equipped with a heating chamber, ZnSe window, and liquid N_2-cooled MCT (HgCdTe) detector. The flow-through heating chamber enabled in situ analysis. Proper He purging was essential to minimize spectral contributions from residual gases in the IR chamber. A quadrupole mass spectrometer (QMS, PFEIFFER VACUUM - QME 200) was coupled to the gas outlet to assist in product identification.

Under constant He flow (30 mL min^{-1}), the procedure consisted of:

- In situ sample drying (40 mg) under pure He flow at 773 K (heating rate 10 K min^{-1}), held for 1 h
- EtOH adsorption from a EtOH:He flow generated by a bubbler at 273 K, maintained for 30 min at 298 K
- Surface cleaning with pure He for 30 min to remove physisorbed molecules
- Outlet flow diversion to the mass spectrometer
- Desorption at 2 K min^{-1} under pure He flow, with IR spectra acquisition every 5 K (4 cm^{-1} resolution, 4000 cm^{-1} –400 cm^{-1}) until 673 K.

3.5 SINS experiments

3.5.1 Sample preparation

The Au substrates consisted of Si wafers from Topsil, p-doped with B, featuring a [100] crystallographic orientation and approximately 400 μm thickness. These substrates received an additional 50 nm Au layer deposited via sputtering.

A small amount of the catalyst was placed in a microcentrifuge tube with 5 cm^3 of water to suspend the powder. The tube underwent vigorous agitation on a vortex mixer, followed by sonication in an ultrasonic bath for 15 min. The samples were prepared by drop-casting an aqueous suspension containing the catalysts onto the previously prepared Au surface. The samples were then dried under a vacuum desiccator for 24 h at room temperature.

In the SINS area spectra experiment, the strategy was not to complete coat Si wafers with Au. Instead, small grids were defined on the surface by lithography using Scanning Electron Microscopy – Focused Ion Beam (SEM - FIB) to delimit the regions, as illustrated in Figure 3.1.

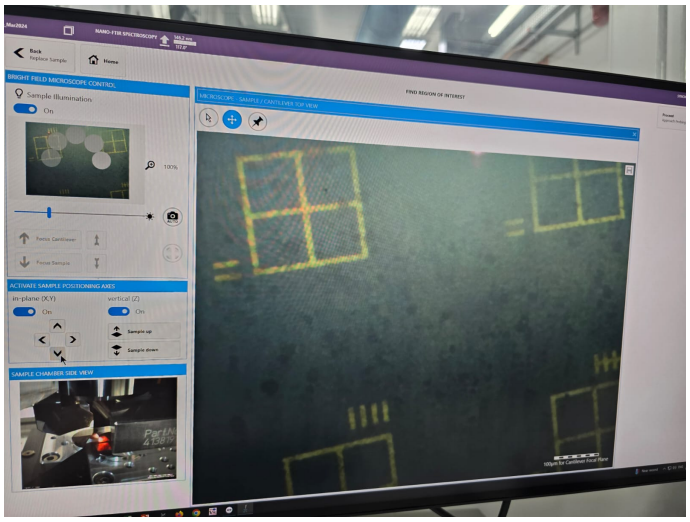

Figure 3.1: Photograph of the screen of the s-SNOM system displaying a Si wafer with Au microgrids

The grid facilitated the localization of the same nanoparticle in the microscope before and after the Ex-Situ Ethanol Temperature-Programmed Desorption (EETPD) treatment, which is described in the following subsection.

3.5.2 Ex-Situ Ethanol Temperature-Programmed Desorption (EETPD) protocol

Both the EETPD unit and the methodology were developed. The experimental EETPD unit comprised two main parts, as illustrated in Figure 3.2. The first part

(Figure 3.2a) was responsible for generating and controlling the saturated gas flow. In this stage, the carrier gas (N_2) was directed by a flow controller to a bubbler, maintained at a constant temperature of 291 K by a thermoregulated bath. A bypass valve allowed the flow to be redirected into the reaction chamber.

The second part (Figure 3.2b) consisted of the heating chamber, where the sample was placed. The chamber temperature was controlled by an external system, the same device used for the DRIFTS chamber. The saturated gas was introduced into the chamber through a dedicated inlet, enabling contact with the sample during adsorption and reaction steps.

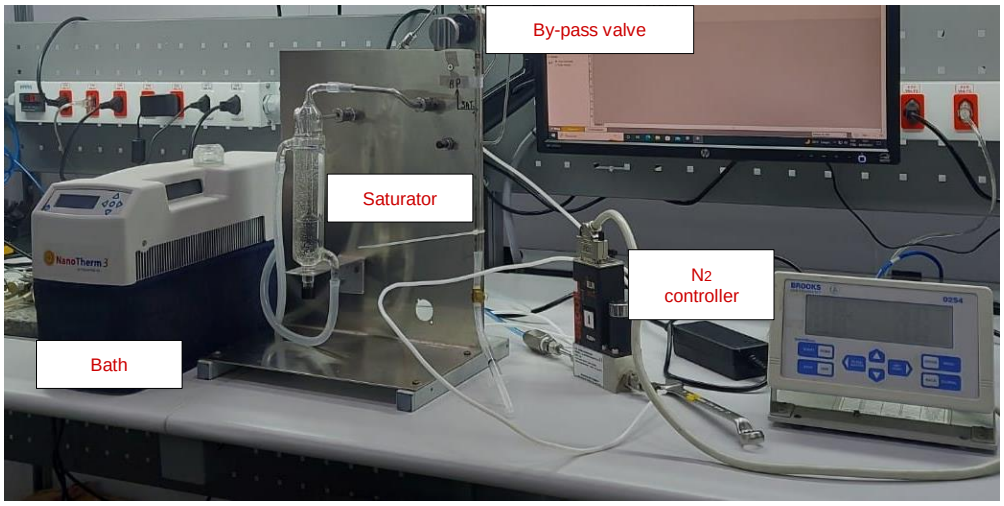

(a) First part

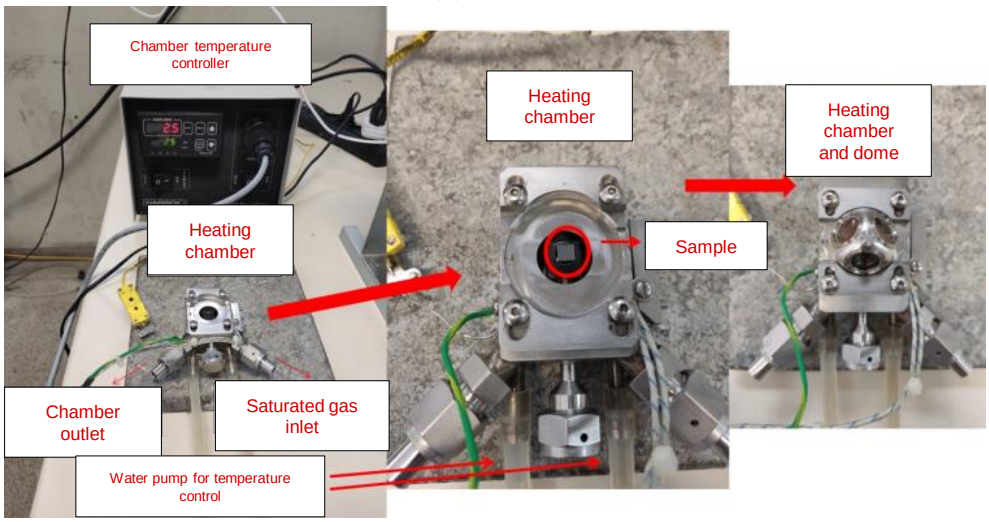

(b) Second part

Figure 3.2: EETPD unit

Once prepared, the sample was placed inside the heating chamber and subjected to a controlled thermal protocol, illustrated in Figure 3.3. Two sets of experiments were conducted using SINS spectroscopy. The first set involved point measurements, while the second focused on area measurements. In Experiment 1, the sample was

initially exposed to 5% EtOH in N_2) for adsorption, followed by a purging step under a flow of pure N_2. Subsequently, successive heating and cooling cycles were carried out, interspersed with spectral acquisitions. In Experiment 2, a similar protocol was applied; however, only a single cycle of heating, cooling, and spectral acquisition was performed.

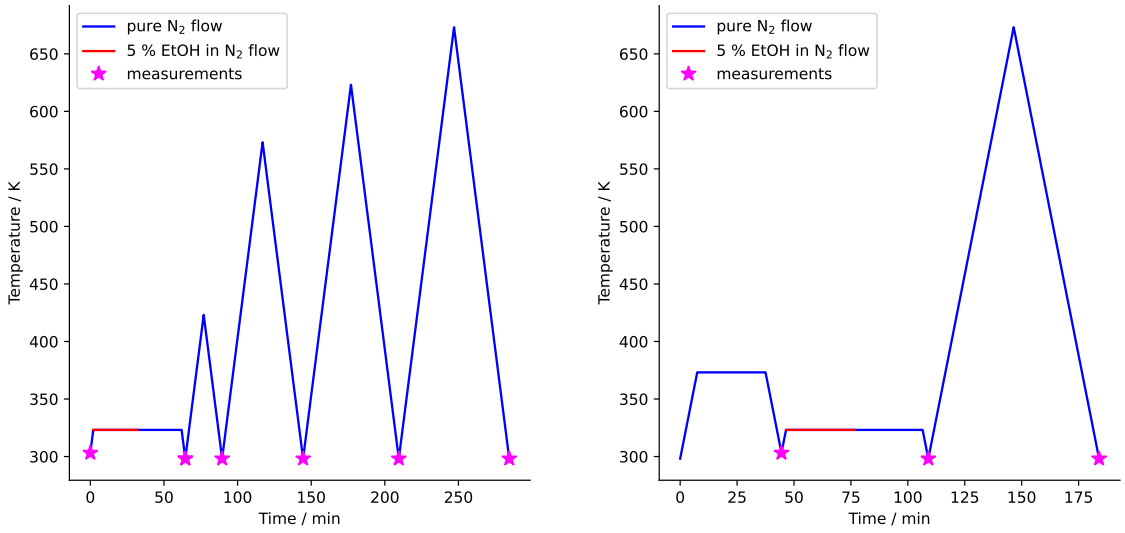

(a) Experiment 1

(b) Experiment 2

Figure 3.3: Temperature profile applied to the sample by EETPD

The experiment includes a linear heating ramp to 323 K, and exposure to 5% EtOH in N_2, surface cleaning, and desorption/reaction, as indicated. The magenta stars indicate the spectral measurements.

3.5.3 Micro-Fourier transform infrared (FTIR)

In order to verify the effectiveness of the adsorption/desorption protocol described in Section 3.5.2, the single-point spectrum was collected — to the MgO-p after EtOH desorption at 673 K — in the 4000–700 cm^{-1} range using an Agilent Cary 620 microscope coupled to an Agilent Cary 670 spectrometer equipped with a Globar source using the reflection mode with a 25× objective lens. This spectrum was normalized by a spectrum obtained from a clean Au wafer surface. The spectral resolution of the equipment guaranteed by the manufacturer is 0.075 cm^{-1}.

3.5.4 s-Scanning Near-Field Optical Microscopy (s-SNOM) combined with nano-Fourier transform infrared (FTIR)

SINS experiments were performed at the IMBUIA beamline at the Brazilian Synchrotron Light Laboratory (LNLS) IR beamline at the Sirius electron

accelerator. The SINS technique combines s-SNOM with a high-brightness broadband synchrotron IR radiation as the excitation source to perform IR spectroscopy with nanometer-sized spatial resolution. Using a commercial s-SNOM microscope (Neaspec GmbH) with typical tips (Arrow with a Pt/Ir-coating, NanoWorld AG), broadband IR images with 100 $\times$ 100 pixels^2 and 2 μm s^{-1} integration speed were acquired. The SINS point-spectra, corresponding to the second harmonic of Ω, were recorded in the frequency window at 900–2000 cm^{-1}, with a spectral resolution of 20 cm^{-1}. These spectra were normalized by the SINS spectrum obtained from a clean Au surface, which was similar to that one utilized for the sample immobilization. The SINS measurements of the samples were conducted immediately after the heat chamber sample's unloading.

The AFM and s-SNOM images were processed with the assistance of the open-source software `Gwyddion` [2] version 2.63.

For the area scans, 49 measurments were collected on particles approximately 0.7 x 0.7 μm in size. EtOH was then adsorbed, after which the same grid region prior to EETPD was located and another measurement was performed. Finally, the procedure was repeated after the sample underwent the EtOH desorption/reaction step.

Due to the large volume of data, we used a baseline correction algorithm based on weighted asymmetric least squares (Asymmetric Least Squares - ALS), with automatic selection of the smoothing parameter. The corresponding code is available in the GitHub repository.

[2] http://gwyddion.net/

Chapter 4

Results and Discussions

4.1 Challenges on the Catalyst synthesis

Regarding the synthesized catalysts, a relevant experimental limitation was observed in the synthesis yields. The low yields obtained by the solvothermal ($\approx$ 14 %) and hydrothermal ($\approx$ 21 %) methods, in comparison with the precipitation method ($\approx$ 60 %), may have resulted from several factors. In solvothermal and hydrothermal processes, significant losses occurred during the centrifugation, washing, and drying steps, along with the possible incomplete conversion of precursors, which led to reduced yields. However, the goal of these syntheses was not to optimize the yield, but to obtain a distinct morphological composition capable of providing different reactive properties to the catalysts. Therefore, the main results related to the local surface characteristics are presented first.

As will be discussed later, hierarchical catalysts exhibit distinct morphologies. For identification purposes, the sample obtained by precipitation, which does not present a well-defined morphology, is referred to as MgO-p. Catalysts with flower-like structures are designated MgO-f, whereas those with wire-like morphology are labeled MgO-w.

4.2 Catalyst Characterization

4.2.1 Crystalline Structure

Figure 4.1 shows the XRD patterns of the MgO-f and MgO-w hierarchical catalysts, compared to the standard MgO-p. Two crystalline phases, brucite ($Mg(OH)_2$, Figure A.1a) and periclase (MgO, Figure A.1b), were identified in all catalysts. The diffractograms confirm the crystalline nature of MgO, with peaks corresponding to its cubic periclase structure (HORNAK, 2021). Periclase can be accurately characterized (COD database code: 9000493) by diffraction peaks located

at approximately 36.8°, 42.7°, 62.1°, 74.4°, and 78.3°, which correspond to the lattice planes [111], [200], [220], [311], and [222], respectively. Brucite, in turn, can also be identified (COD database code: 9002348) by peaks observed at 18.7°, 33.1°, 38.0°, 38.3°, 51.2°, 58.2°, 58.5°, 59.1°, 59.5°, 62.5°, 68.8°, 69.4°, 72.4°, 72.6°, 81.3°, 81.9°, and 87.9°, corresponding to the lattice planes [001], [010], [012], [013], [021], [031], [103], [200], [112], [113], [104], [202], and [113], respectively. It is important to note that the studies that inspired the synthesis method of the hierarchical catalysts reported only the periclase phase after thermal treatment at 723 K (AL-GHAMDI *et al.*, 2012; LEE *et al.*, 2020).

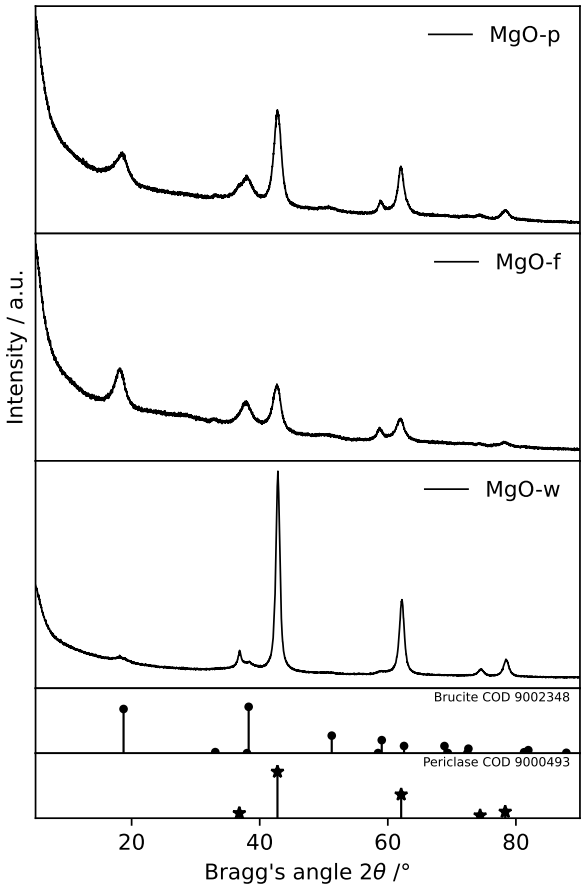

Figure 4.1: PXRD pattern of MgO-p and hierarchical MgO: MgO-f, MgO-w

Although the three structures are composed of pure MgO, the MgO-w catalyst exhibits narrower peaks, which can be associated with larger crystallites, as predicted by the Scherrer model. This suggests potential qualitative differences in the densities of two-dimensional defects. However, based solely on ex situ PXRD, the exact distinctions in the crystalline structures of these materials (particularly on the surface) remain inconclusive. Moreover, the limited number of measured Bragg peaks does not support a full refinement, which, in principle, could provide insights into the isotropy related to peaks broadening.

TGA curves shown in Figure 4.2 have revealed two dehydration events up to 773 K. These events are associated with mass loss due to the dehydroxylation of brucite (IONASHIRO *et al.*, 2014). This suggests that MgO previously treated at 773 K may have undergone hydration during storage in a desiccator, prior to the PXRD measurement.

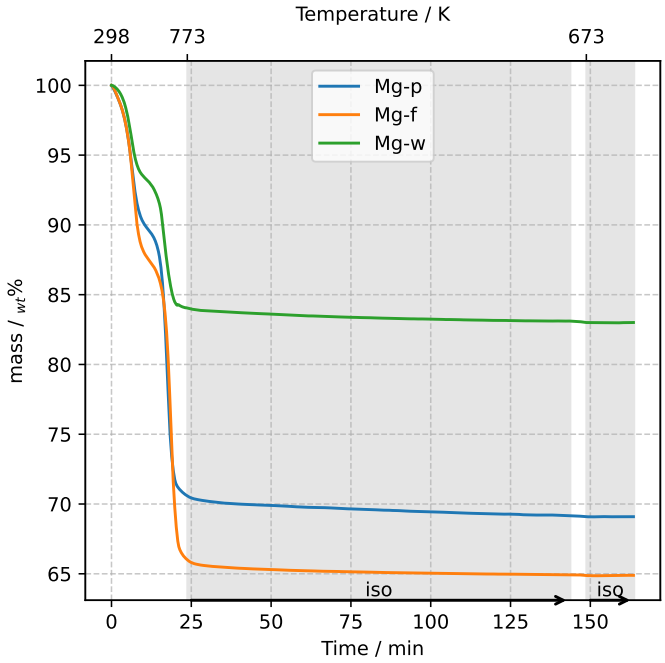

Figure 4.2: TGA curves of MgO catalysts.

Experimental conditions — inert atmosphere (N_2); flow rate of 30 cm^3 min^{-1}; heating rate of 20 K min^{-1} from 298 K to 773 K, followed by a 2 h isothermal step at 773 K; cooling at 20 K min^{-1} to 673 K with a 15 min isothermal step. The MgO-w sample weight used in the experiment was approximately 50 % larger than the others, which explains the delayed thermo-temporal completion of the second decomposition event (IONASHIRO *et al.*, 2014).

The Mg-f sample has exhibited the highest mass loss, approximately 35 %, indicating a significant amount of brucite. The Mg-p sample has shown an intermediate loss of around 30 %, whereas Mg-w has presented the lowest variation, with a mass loss close to 20 %, suggesting a higher degree of conversion to periclase. These results are consistent with the phase's composition trends revealed by Rietveld refinement.

The combined use of PXRD, and TGA allowed the inference that periclase is the predominant phase, at least at the beginning of the catalytic test. Yet, it remained uncertain if the material undergoes rehydration and transformation into brucite following exposure of the material to an EtOH-containing atmosphere. The use of operando PXRD could clarify whether a phase transition between periclase and brucite indeed takes place under reaction conditions.

4.2.2 Area and Porosimetry

N_2 physisorption results are presented in Figure 4.3 and Table 4.1. The MgO-p and MgO-f samples exhibited type II isotherms with an H3 hysteresis loop, while the MgO-w sample showed a behavior closer to type I. Although classified as type I, the MgO-w isotherm shows similarities to type II at the end of the hysteresis loop.

Generally, type II isotherms are associated with the presence of macropores and unrestricted multilayer adsorption, while type I isotherms are typical of microporous solids with relatively small external surfaces (MARTINS and JR., 2024). The H3 hysteresis loop indicates the presence of slit-shaped pores, where adsorption occurs in an unrestricted monolayer (SING, 1985). The nearly horizontal hysteresis loop observed for MgO-w suggests that this sample has a significantly higher amount of micropores compared to the others. Thus, the specific surface area of MgO-w is more appropriately estimated using the t-plot method, while for the other samples, the BET method is more suitable.

The data in Table 4.1 show that the specific surface areas of the catalysts follow the trend MgO-p < MgO-w < MgO-f. Furthermore, the total pore volume of MgO-w is lower than that of the other catalysts, following the trend MgO-w < < MgO-f < MgO-p.

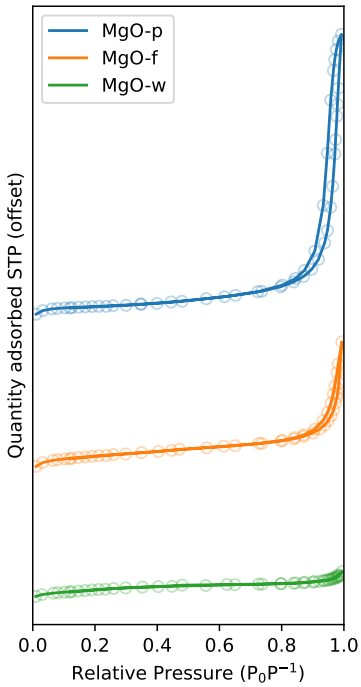

Figure 4.3: N_2 physisorption isotherms

Table 4.1: N_2 physisorption quantification results

Sample	Specific area / $m^2\ g^{-1}$	BJH total pore volume adsorption / $cm^3\ g^{-1}$	BJH total pore volume desorption / $cm^3\ g^{-1}$
MgO-p	134	1.13	1.36
MgO-f	227	0.42	0.53
MgO-w	171 (*)	0.11	0.13

(*) Estimated by the t-plot method

The mesoporosity observed in MgO-p and MgO-f is consistent with that reported by PACHECO (2019) and LEE *et al.* (2020), respectively. However, PACHECO (2019) have reported a specific surface area approximately 68 % lower than that observed for MgO-p, which can be attributed to the more severe thermal treatment conditions employed (873 K for 12 h, compared to 773 K for 3 h in this work).

The microporous structure identified for MgO-w is in agreement with the results obtained by PXRD, since this sample exhibits higher crystallinity, likely associated to a less harsh thermal stress. Considering that all samples were subjected to the same treatment conditions, the observed difference suggests that intrinsic characteristics of the precursor or the synthesis route promoted a more homogeneous sintering process and, consequently, the formation of larger and more ordered crystalline domains in MgO-w.

4.2.3 Microscale Analysis

Figure 4.4 presents the micrographs of the three synthesized catalysts. The MgO obtained by precipitation (MgO-p) did not exhibit a well-defined morphology, showing stacked structures in the form of plates, as seen in Figure 4.4 (a-b). This is in agreement with what was planned, given that no attention was particularly given to tuning this material's morphology. Rather, it was synthesized as to reproduce benchmark protocols for typically reported MgO.

The material synthesized via the hydrothermal method (MgO-f) displayed a morphology resembling a flower — or a dandelion — (Figure 4.4 (c-d)), which is comparable to the structure reported by LEE *et al.* (2020), with average particle size of 714 nm (Figure 4.5 (a)). At first, it is assumed that, similarly to LEE *et al.* (2020), the structure was formed through a hierarchical growth process, resulting in a shell of plates that ultimately led to a hollow structure. This characteristic is noteworthy and may inspire future research aimed at designing more complex catalysts, incorporating transition metals, such as widely studied core-shell catalysts (TAN *et al.*, 2020).

MgO-p and MgO-f suggest surface characteristics different from those of MgO-

w. According to KLABUNDE *et al.* (1996), nanostructured MgO with irregular polyhedral shapes — such as flower-like MgO-f petals — has exhibited a high density of structural defects, such as edge and corner sites, vacancies, and surface terminations with low coordination. These defects have been identified through indirect experimental evidence, including gas adsorption studies (SO_2, CO_2, HCl) and FTIR analysis of surface hydroxyls, which have shown preferential monodentate adsorption and lower Brønsted acidity on defective surfaces.

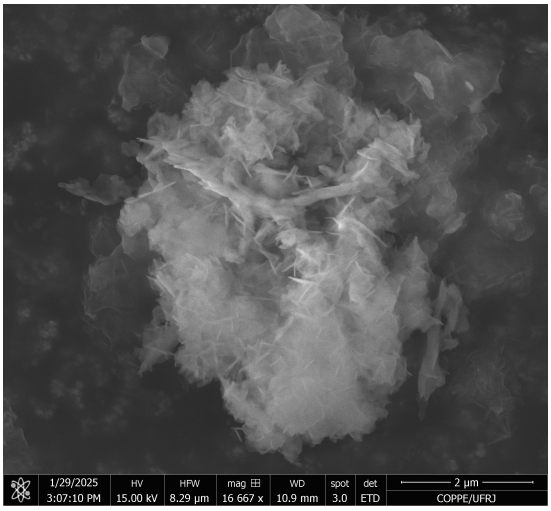

(a) MgO-p - 16,667×

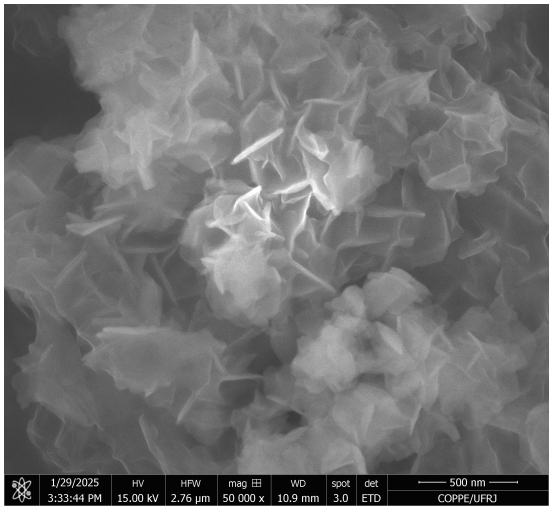

(b) MgO-p - 50,000×

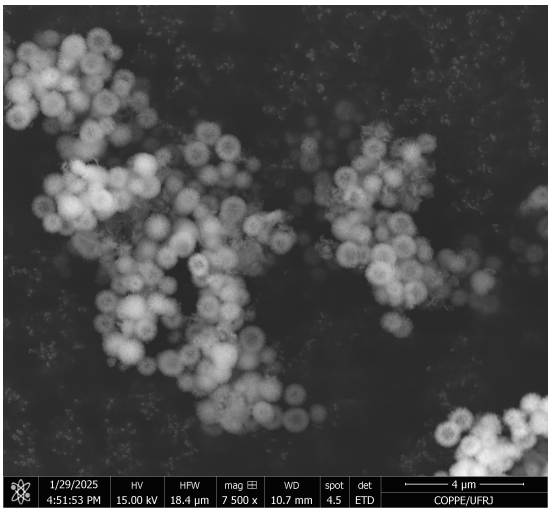

(c) MgO-f -7500×

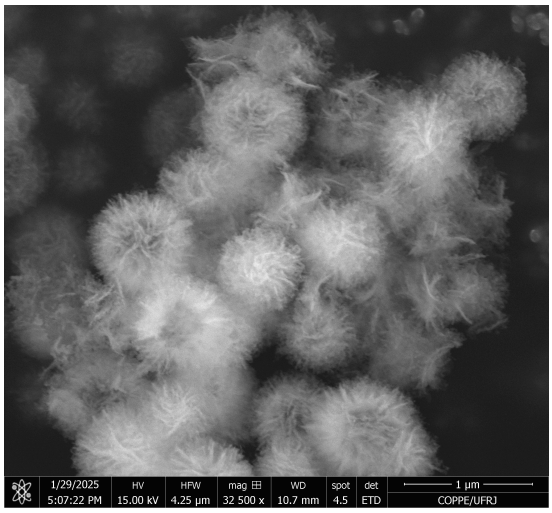

(d) MgO-f - 32,000×

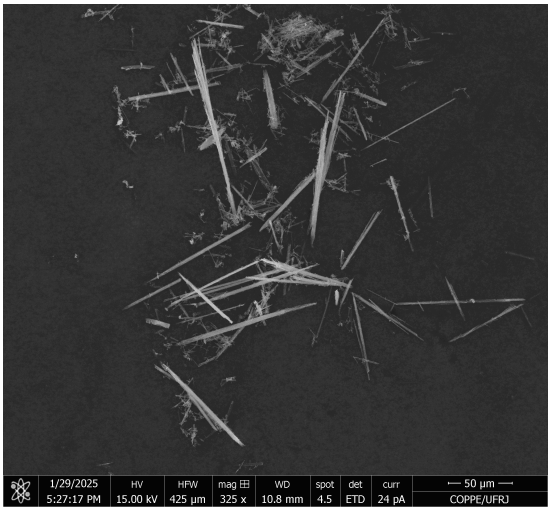

(e) MgO-w - 325 ×

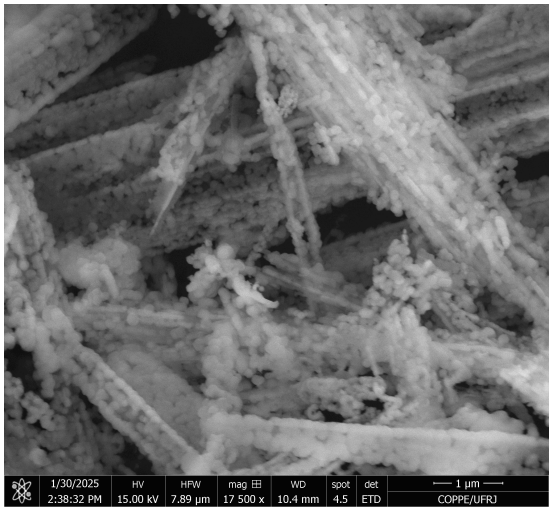

(f) MgO-w - 17,500×

Figure 4.4: SEM images of (a-b) precipitated (MgO-p), (c-d) flower-like (MgO-f), and (e-f) wire-like (MgO-w) MgO

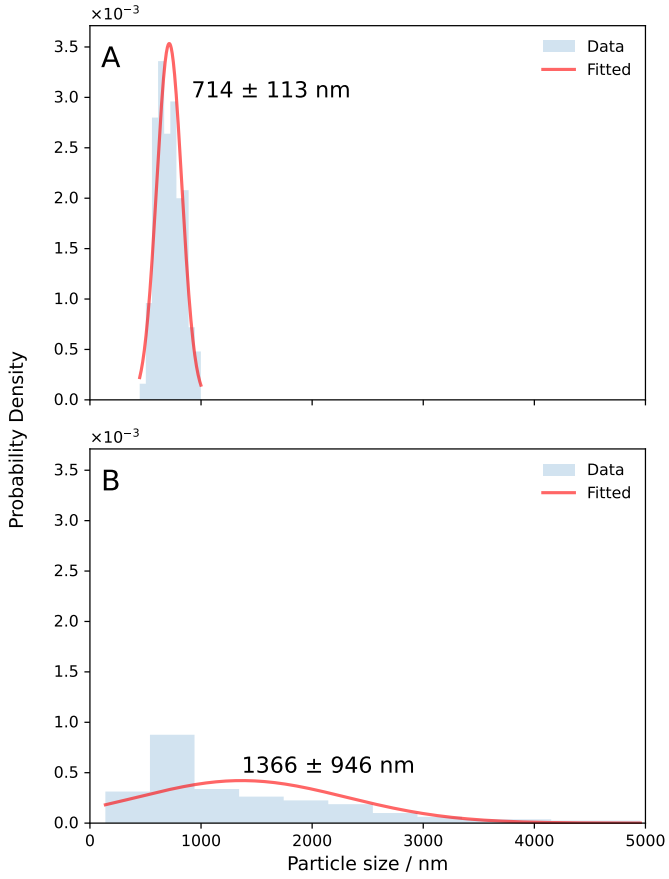

Figure 4.5: Fitted normal distribution function to particle size data for (a) MgO-f, and (b) MgO-w

200 particles were counted

Similarly, ROY *et al.* (2017) have demonstrated that the morphology of Cu–MgO catalysts synthesized by hydrothermal and wet impregnation has significantly influenced the surface area and the accessibility of active sites. Morphologies such as "marigold flower" or "house of cards" have promoted higher porosity due to the self-assembly of nanoparticles into overlapping flakes. In the present study, the MgO-f sample, with its hierarchical flower-like morphology, has shown structural features comparable to the microscopy images reported by ROY *et al.* (2017), suggesting the presence of an interlamellar pore network and a high number of exposed sites, such as edges and vertices. This topography favors reactant adsorption and may increase the density of defects.

The study by SELVAMANI *et al.* (2011) has provided an analysis of structural defects in MgO microflakes obtained from the controlled calcination of hydromagnesite, which resemble the MgO-p and MgO-f catalysts. Based on photoluminescence spectroscopy, FTIR, and temperature-programmed desorption (TPD)-CO_2 analyses, the authors have identified oxygen vacancies (F centers), low-

coordinated O^{2-} ions (O^{2-}_{5C}, O^{2-}_{4C}, O^{2-}_{3C}), and surface-adsorbed hydroxyl groups, all of which have been associated with the basic activity and catalytic reactivity of the surface.

Finally, the catalyst obtained by the solvothermal method exhibited a wire-like morphology (MgO-w) a characteristic also reported in the literature (HADIA and MOHAMED, 2015). The larger wires consist of finer wires, similar to natural fibers composed of fibrils, and these fibrils, in turn, appear to be formed by agglomerates of small spheres or plates (Figures 4.4e, and 4.4f). This structural feature is reflected in the average wire widths (approximately 1.4 μm) and in their distribution (Figure 4.5 (b)), which presents a significantly broader profile compared to the material obtained via the hydrothermal method.

In addition to the distinct morphology observed for the MgO-w sample, it is relevant to consider the possible formation of similar or other structural defects that may influence its catalytic behavior. The SEM images obtained for MgO-w resemble those reported by SUTRADHAR *et al.* (2011). According to the authors, MgO nanostructures have exhibited a high concentration of lattice defects. These defects have been identified through photoluminescence spectroscopy, in which emission bands in the visible range (green to red) served as signatures of low-coordination oxygen species associated with edges, corners, and step terraces. The presence of such sites increases the surface basicity due to the unsaturated electronic environment, promoting the formation of strong Lewis base sites. Consequently, these features have been shown to significantly enhance catalytic activity in base-catalyzed reactions, such as the Claisen–Schmidt condensation, by facilitating the adsorption and activation of reactant molecules. Therefore, it is plausible that similar defect-related phenomena are present in the MgO-w material.

As a final remark in this section, it is important to note that microscopy reveals only a portion of the material's microstructure, which does not necessarily represent the average surface bulk properties. The analyzed regions may exhibit specific features influenced by local heterogeneities. Thus, conclusions drawn from such observations should be interpreted with caution, particularly when extrapolated to the overall behavior of the material.

4.3 Catalytic Performance

4.3.1 Kinetic Regime Assessment

A linear correlation between EtOH conversion and space-time is observed in Figure 4.6, using the most reactive catalyst (MgO-p) and the highest operating temperature applied in this work. Background conversion of EtOH remained below

4 % at 723 K, as reported by SANTOS *et al.* (2025), indicating that the activity without a catalyst is negligible. Based on the method described by BIRKY *et al.* (2013); PACHECO (2019); PINHEIRO *et al.* (2024a), within the range of 0.8 to 2.5 min g_{cat} cm^{-3}, it is assumed that the investigated reaction system operates under kinetic control. Therefore, this indicates that the pore diffusion limitations can be neglected. Moreover, as the linearity could be reasonably extrapolated to the origin (given that the predict model's intercept is 1.5, close enough to 0 given the experimental error), differential reactor behavior was considered; thus, Equation 3.4 was assumed valid.

Later (in subsection 4.3.3), the results of the catalytic tests fitted to the Arrhenius model will be presented. In advance, it is observed that the estimated activation energy (minimum of 67 kJ mol^{-1}) is consistent with processes governed by surface kinetics. If the fit to the model were not satisfactory — especially at higher temperatures — one would expect a significantly lower activation energy, around 30 to 40 kJ mol^{-1}, which is typical of diffusion-controlled systems (I. CHORKENDORFF, 2017b). Therefore, the order of magnitude of the estimated Arrhenius constants also indicates that the reactions are not limited by external diffusion.

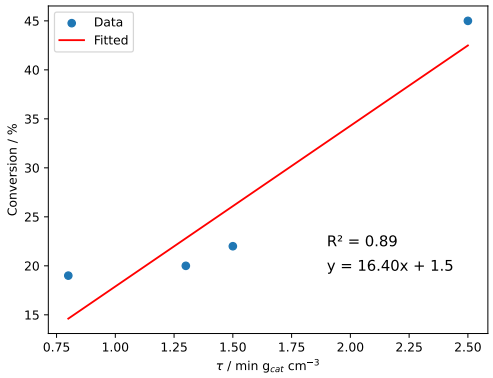

Figure 4.6: Linear relationship of EtOH conversion over p-MgO (TOS = 2 h) proportional to reactor space-time

This result confirms differential reactor behavior for the p-MgO, the most reactive catalyst at the highest investigated temperature (723 K).

4.3.2 Steady-state Reaction

To minimize the effect of textural properties on catalytic activity, the observed conversions were normalized with respect to the specific area determined by N_2 physisorption. This approach has been adopted to enable a fair comparison among the catalysts, considering the difficulty in directly quantifying the actual active sites

present in each evaluated material. Reactions at 648 K - 723 K reach a steady state within the first hours of reaction (TOS = 2 h), as shown in Figures 4.7-4.9. The main products observed were ET, AcO, and BuOH, as presented in appendix B.1. Minor ones include butene isomers, BuO, methane, C_2H_6, C_3H_6, CrO, CrOH, DEE, Me_2CO and ethyl acetate, also presented in appendix B.2.

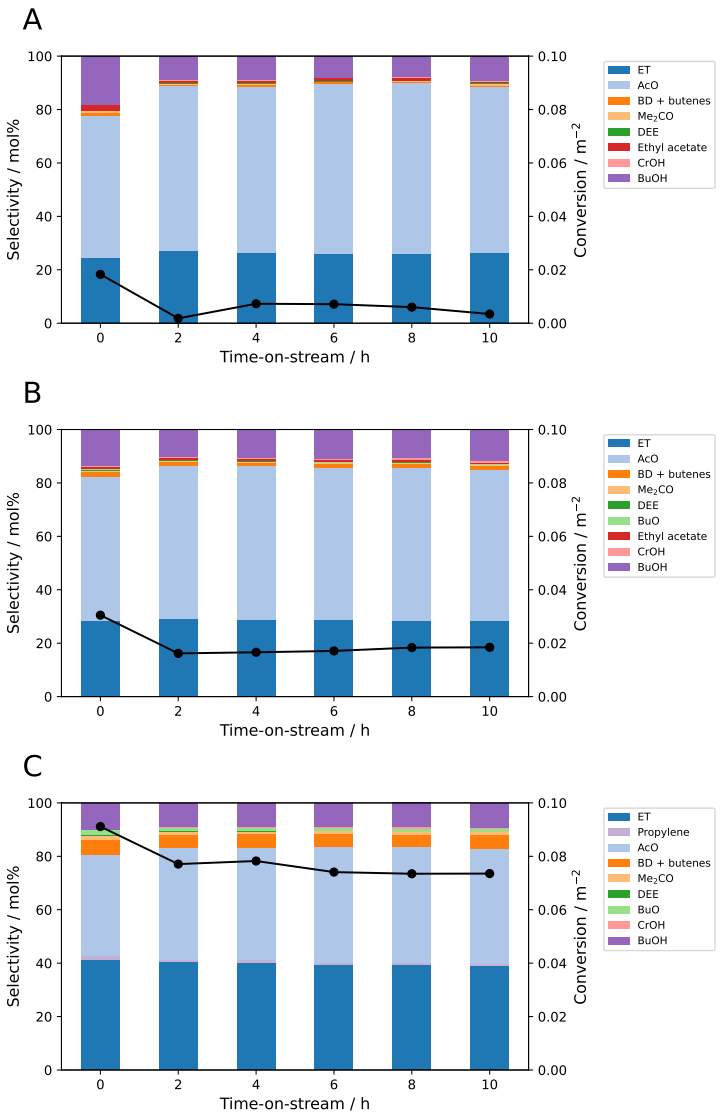

Figure 4.7: Catalytic performance for p at (a) 648 K, (b) 673 K, and (c) 723 K.

1 bar, $\tau = 1.5$ min·mg$_{cat}$·cm^{-3} (50 mg of catalyst, and 33.33 cm^3·min^{-1}), EtOH = 5 mol% in N_2. carbon balance (CB) at 648, 673, and 723 K were 97.3, 91.9, and 68.6 %, respectively.

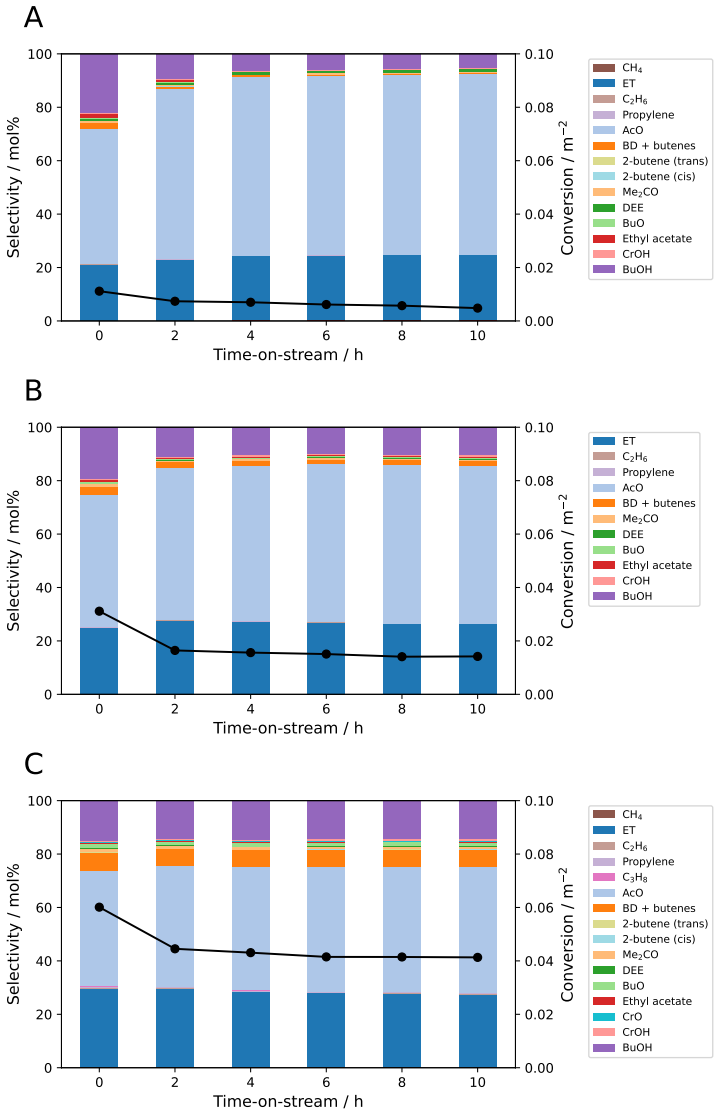

Figure 4.8: Catalytic performance for MgO-f at (a) 648 K, (b) 673 K, and (c) 723 K.

1 bar, $\tau = 1.5$ min·mg$_{cat}$·cm^{-3} (50 mg of catalyst, and 33.33 cm^3·min^{-1}), EtOH = 5 mol% in N_2. CB at 648, 673, and 723 K were 98.3, 93.6, and 94.3 %, respectively.

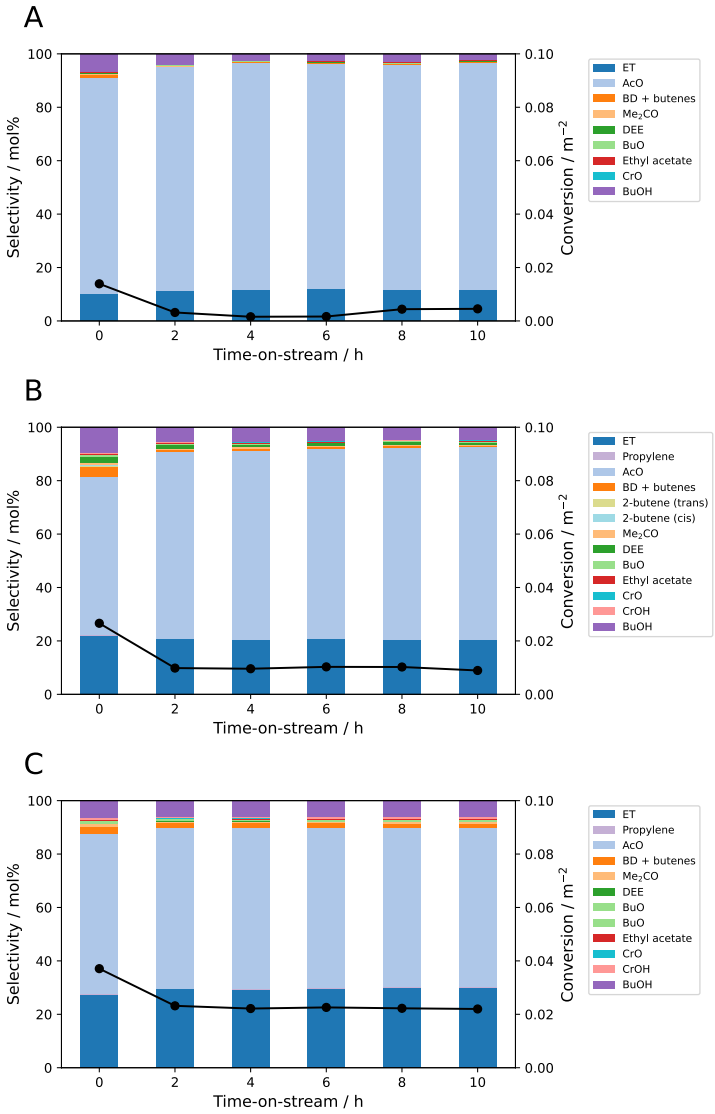

Figure 4.9: Catalytic performance for MgO-w at (a) 648 K, (b) 673 K, and (c) 723 K.

1 bar, $\tau = 1.5$ min·mg$_{cat}$·cm^{-3} (50 mg of catalyst, and 33.33 cm^3·min^{-1}), EtOH = 5 mol% in N_2. CB at 648, 673, and 723 K were 95.3, 99.8, and 91.8 %, respectively.

In general, AcO, formed via dehydrogenation of EtOH, has been the main product for all catalysts. As the conversion increased, the product distribution shifted proportionally with temperature towards both the coupling product (BuOH) and the undesired dehydration product (ET). The linearity of these selectivities with temperature has once again confirmed that the reactor operated under differential conditions with respect to EtOH conversion, as expected for a consecutive reaction network in which AcO acts as an intermediate in the conversion of EtOH to BuOH, as shown in appendix B.3. Selectivity towards ET has also been reported in other studies that have investigated EtOH conversion over MgO at 673 K (BIRKY

et al., 2013; HANSPAL *et al.*, 2015; PACHECO, 2019). Moreover, no significant deactivation has been observed over a reaction time of up to 10 h in all cases. It is worth noting that, although it is known that under these conditions MgO is up to 300 % less active in the coupling of EtOH to BuOH compared to HAP (HANSPAL *et al.*, 2015). HAP has been shown to undergo considerable deactivation, mainly due to the formation of strongly adsorbed polymeric carbon species that irreversibly poison the POH-type acid sites (OSMAN *et al.*, 2019). Therefore, the catalytic stability observed for MgO-based materials reinforces their potential as selective basic sites for directing EtOH conversion.

Figure 4.10 presents the results of the catalytic tests performed at (a) 648 K, (b) 673 K, and (c) 723 K for TOS = 2 h. At lower temperatures, the catalytic activity was minimal (less than 10 %), but increased as the temperature increased. This behavior seems to reflect the exponential influence of the temperature on the overall rate constant, as described by the typical Arrhenius model.

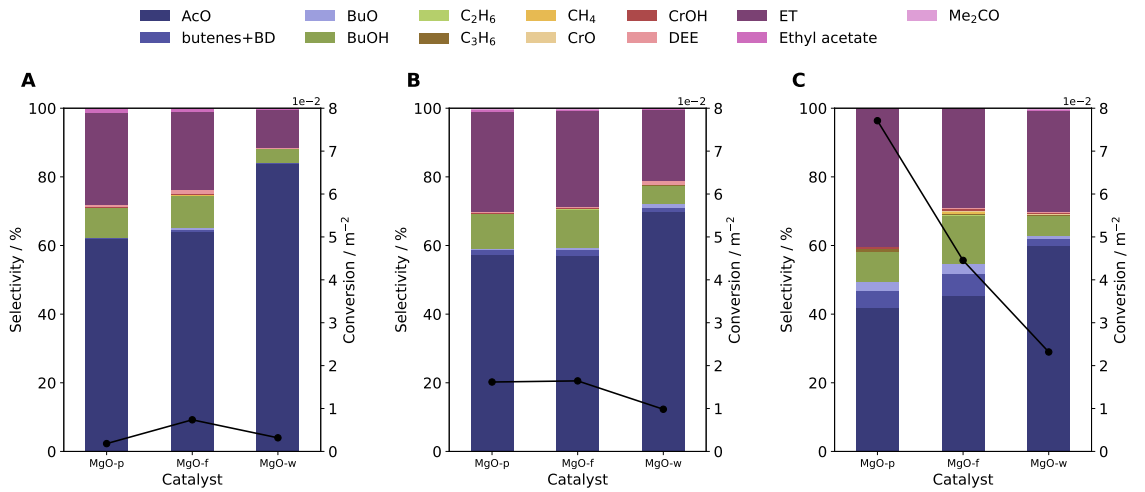

Figure 4.10: Catalytic performance. Selectivity, and specific conversion at (a) 648, (b) 673, and (c) 723 K

1 bar, $\tau = 1.5$ min·mg_{cat}·cm^{-3} (50 mg of catalyst, and 33.33 cm^3·min^{-1}), EtOH = 5 mol% in N_2, TOS = 2 h. CB for p, f, and w, respectively = 97.3, 98.3, and 95.3 % (at 648 K); 91.9, 93.6, and 99.8 % (at 723 K); and 68.6, 94.3, and 91.8 % (at 773 K).

At 648 K and 673 K, all catalysts have shown selectivity below 1 % for minor products. At 773 K, an increase in the formation of some of these by-products, such as butenes, BD, and BuO, has been observed, particularly for MgO-p and MgO-f catalysts, reaching approximately 10 %. In principle, BuO may act as an intermediate in the C–C coupling process of EtOH over MgO. This compound would be formed from CrO or CrOH through intermediate hydrogenation reactions within the Guerbet mechanism. However, at around 673 K, there is sufficient evidence that

BuO is, in fact, a consecutive product derived from BuOH (CHIEREGATO *et al.*, 2015; DE SOUZA *et al.*, 2020; NDOU and COVILLE, 2004; SCALBERT *et al.*, 2014). For instance, calculations reported by DE SOUZA *et al.* (2020) suggest that, along the aldol route, the conversion of BuO into BuOH via the MPV reaction involves barriers as high as 1.00 eV, making this pathway less favorable from an energetic perspective than the direct hydrogenation of CrOH to BuOH. The authors likewise reported experimental evidence revealing that, when feeding the system with BuOH, the major product was BuO and no CrO was detected, further supporting their argument. Therefore, the increased selectivity toward BuO observed here — at a sufficiently high temperature (773 K) — can be explained by: i. an enhanced rate of the hydrogenation reaction from BuOH to BuO; and/or ii. the availability of sufficient energy to promote the aldol route, as shown at the end of the first cycle in Figure 2.5.

Regarding BD, this compound is formed through a pathway parallel to that of BuOH, known as the Lebedev route (Figure 4.11). This mechanism is somewhat similar to the Guerbet route (Figure 2.1) proposed for the formation of BuOH. Both routes involve the initial dehydrogenation of EtOH to AcO, followed by its self-coupling to form an aldol intermediate. This intermediate is then dehydrated to CrO. From this point on, the routes diverge, each leading to a different final product. CrO can be: i. reduced by EtOH via MPV reaction on basic sites (as expected for pure MgO), or by direct hydrogenation on metallic sites, generating AcO and CrOH, which is subsequently dehydrated to BD; or ii. sequentially reduced to BuOH, with or without the formation of BuO, as previously discussed.

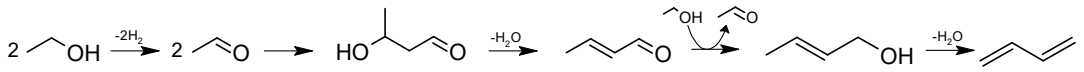

Figure 4.11: Most accepted mechanism regards Lebedev Reaction

Adapted from TAIFAN *et al.* (2017a); YAN *et al.* (2018). Inspired by Toussaint's Aldol condensation mechanism (QUATTLEBAUM *et al.*, 1947)

To conclude the discussion on the mechanisms involved in the formation of minor products, attention is drawn to the butene isomers, which exhibit retention times close to that of BD, making accurate quantification by GC challenging. There are three structural isomers of butene: 1-butene, 2-butene — both displaying *trans* and *cis* geometric isomerism — and 2-methylpropene (*iso*-butene). Based on the products, by-products, and intermediates discussed so far, it is possible to propose a

mechanistic origin of butenes as C_4 products from the conversion of EtOH over MgO. Figure 4.12 presents the proposed reaction network for the conversion of EtOH into butenes, outlining five possible pathways. Among them, three are particularly relevant. The first involves the oligomerization of ET, derived from the dehydration of EtOH (KADAM and SHAMZHY, 2018; YUK *et al.*, 2020). The second corresponds to the direct dehydration of BuOH, which is formed through the Guerbet mechanism (GUNST *et al.*, 2017). The third involves the hydrogenation of BD, generated through the Lebedev route (MICHALAK *et al.*, 2013). For the first case, Figure 4.12 illustrates the mechanism for the formation of 1-butene from EtOH, involving carbenium intermediates in reactions (11) and (12). Outside the proposed network, there is also the possibility of 1-butene isomerization, depending on the stability of the formed carbocation (EAGAN *et al.*, 2019). However, since this is considered a minor pathway, to the best of current knowledge, it has not been reported mechanisms for pure MgO. Such routes have only been observed over catalysts with a pronounced metallic-hydrogenating character, such as Pt and Ag (DAGLE *et al.*, 2020; LIN *et al.*, 2021), as well as Zn- and Zr-based materials (DAGLE *et al.*, 2020; LIN *et al.*, 2021; PINHEIRO *et al.*, 2024b).

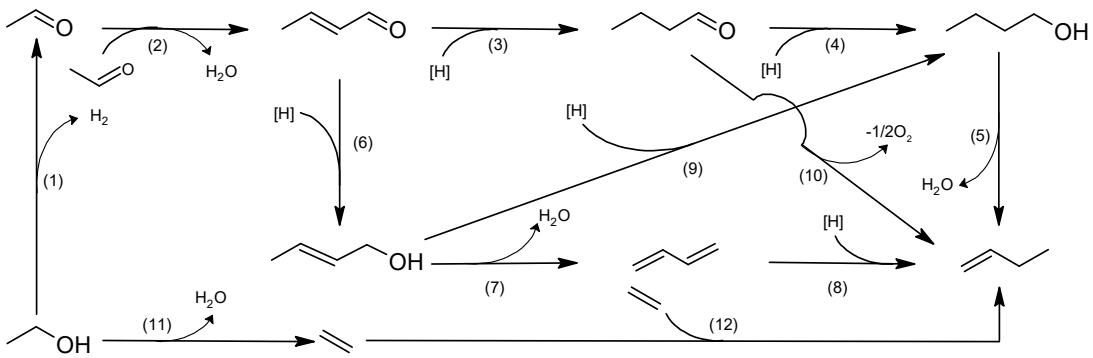

Figure 4.12: Reaction network for the conversion of EtOH to butenes

The reaction network outlines all possible pathways, designated as follows: (11) → (12) (ET dimerization), (3) → (4) → (5) (Guerbet), (6) → (7) → (8) (Lebedev), (6) → (9) → (5) (via CrOH), and (3) → (4) → (10) (via BuO). [H] represents hydrogen from either gas phase H_2 or alcohol hydrogen donors

Adapted from DAGLE *et al.* (2020); EAGAN *et al.* (2019); ZHANG *et al.* (2021).

Depending on the surface properties, such as acidity/basicity, presence of defects, and relative composition, specific reaction pathways may be favored over others (PACHECO, 2019). The MgO-p and MgO-f samples have shown similar product distribution profiles, as shown in Figure 4.10. However, for MgO-w, the

selectivity toward AcO is at least 10 % higher among the three temperatures. This suggests that MgO-w is significantly less active in the coupling reactions that follow the hydrogenation of EtOH to AcO. This difference may be attributed to the lower contribution of low-coordination surface sites on MgO-w. Larger crystallites typically exhibit fewer structural defects, edges, and corners, and tend to be more ordered. In the case of MgO-w, the estimated average crystallite size is at least 77 % larger than that of MgO-p and MgO-f, as discussed in Section 4.2.1.

4.3.3 Microkinetic Interpretation and Compensation Effects

In order to investigate the microkinetics, the effective rate of each compound was calculated as a function of temperature, and then a nonlinear Arrhenius-type model was fitted. The results are presented in Figure 4.13 and Table 4.2.

Microkinetic estimates have shown that the catalytic activity, in terms of specific rate, follows the order MgO-p > MgO-f > MgO-w for all reaction pathways. The MgO-p catalyst has exhibited the highest specific rates, possibly because of its higher density of structural active sites, such as defects and low-coordination sites. In contrast, MgO-w, which shows a larger crystallite size and fewer defects, has shown the lowest reaction rates, particularly for the formation of BuOH, indicating a low efficiency in the coupling route. These results are consistent with experimental observations, in which the higher selectivity toward AcO over MgO-w results from its limited ability to promote subsequent reactions such as coupling and dehydration. This interpretation is supported by the study of DÍEZ *et al.* (2011), which demonstrated that increasing the heat treatment temperature of MgO leads to crystallite growth, a reduction in surface area, and, most notably, to a decrease in the density of low-coordination O^{2-} sites, identified by DRIFTS and TPD using CO_2 as the probe molecule. These sites have been associated with the promotion of RDSs in carbon–carbon coupling reactions, such as aldol condensation, whose formation rates decrease systematically with a reduction in the concentration of these sites. Therefore, the low activity of MgO-w can be rationalized by the limited exposure of unsaturated O^{2-} anions.

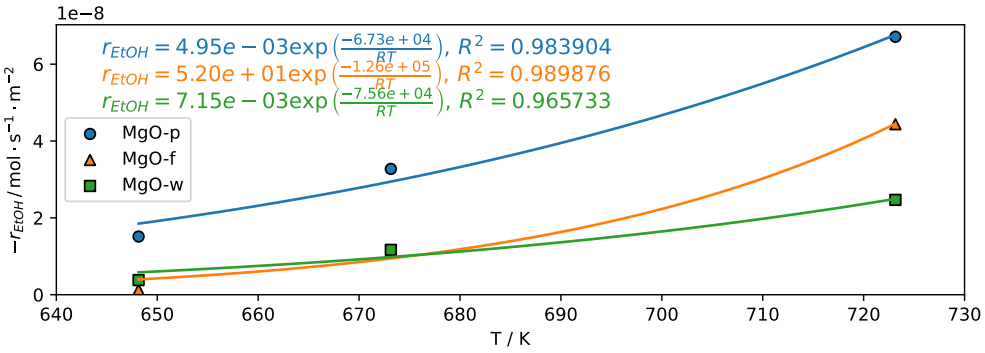

(a) Consumption rate of EtOH

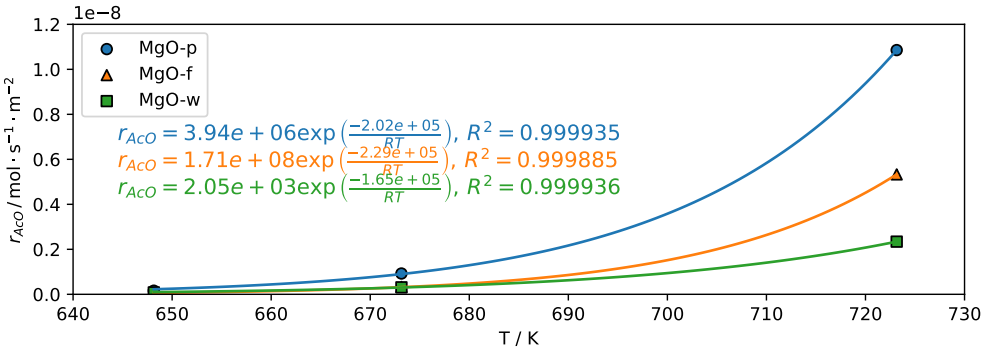

(b) Formation rate of AcO

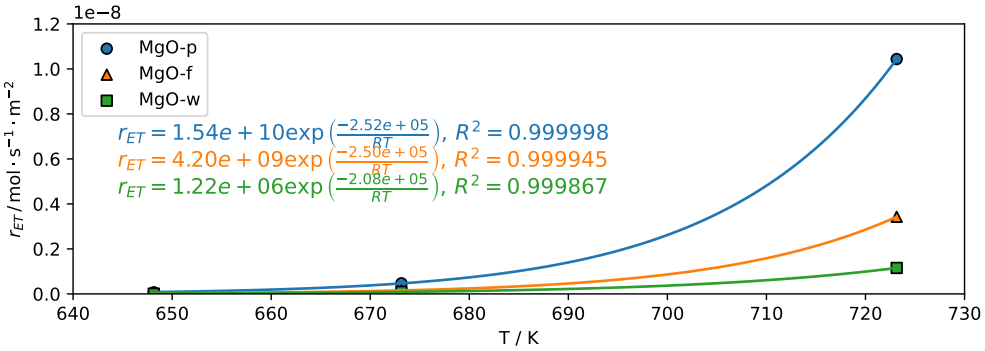

(c) Formation rate of ET

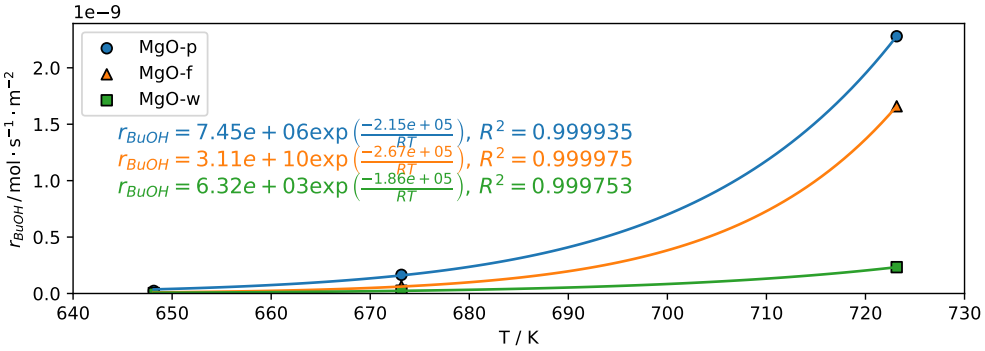

(d) Formation rate of BuOH

Figure 4.13: Non-linear Arrhenius-type model fitting for reaction rate data as a function of temperature.

Table 4.2: Estimated apparent pre-exponential factor and activation Energy for each catalyst

Parameter	**Catalyst**		
	MgO-p	**MgO-f**	**MgO-w**
EtOH			
$\ln\left(\bar{A}/\text{mol}\cdot\text{s}^{-1}\cdot\text{m}^{-2}\right)$	0.38	4.40	0.54
E_{app} / kJ mol^{-1}	67	126	76
AcO			
$\ln\left(\bar{A}/\text{mol}\cdot\text{s}^{-1}\cdot\text{m}^{-2}\right)$	9.28	10.92	6.00
E_{app} / kJ mol^{-1}	202	229	165
ET			
$\ln\left(\bar{A}/\text{mol}\cdot\text{s}^{-1}\cdot\text{m}^{-2}\right)$	12.88	12.31	8.77
E_{app} / kJ mol^{-1}	252	250	208
BuOH			
$\ln\left(\bar{A}/\text{mol}\cdot\text{s}^{-1}\cdot\text{m}^{-2}\right)$	7.56	11.18	4.49
E_{app} / kJ mol^{-1}	215	267	186

Note: The results presented here are the same as in Figure 4.13.

The significance of the estimated parameters can be considered satisfactory, as the coefficients of determination between the data and the model are close to 1, as seen in Figure 4.13. However, it is essential to highlight that the experiments do not have replicates, which introduces uncertainties associated with the measurements and, consequently, with the inferred parameters (PINTO and SCHWAAB, 2007). In practice, the absence of replicates in such experiments is justified by the high experimental load. Nevertheless, it is assumed here that the experiments were well done, and thus the observed results are representative and close to the true population mean.

Based on the premise described in the last paragraphs, a phenomenological interpretation of these estimated parameters according to TST is proposed. The following discussion addresses the essential aspects and considerations for understanding the model, its parameters and, primarily, regarding the thermodynamic information that they convey.

The expression of the kinetic rate in the context of TST, derived from thermodynamic principles, is given by the following:

$$r = \underbrace{\left(\frac{k_B T}{h}\right) e^{\frac{\Delta S_0^{\ddagger}}{R}} e^{\frac{-\Delta H_0^{\ddagger}}{RT}}}_{k_{\mathrm{TST}}} \cdot f(C_i) \tag{4.1}$$

where k_{TST} highlights the contribution of activation entropy and enthalpy (I. CHORKENDORFF, 2017a; NØRSKOV *et al.*, 2014). Here, $\Delta S_0^{\ddagger}$ and $\Delta H_0^{\ddagger}$ correspond to the standard entropy and enthalpy changes associated with the formation of the transition state, while R is the universal gas constant. According to classical thermodynamics, these quantities define the standard Gibbs free energy of activation through the relation $\Delta G_0^{\ddagger} = \Delta H_0^{\ddagger} - T\Delta S_0^{\ddagger}$, which governs the height of the energetic barrier that reactants must overcome to reach the transition state. The first term in Equation 4.1, $\frac{k_B T}{h}$, represents the pre-exponential factor associated with the frequency of molecular collisions, where k_B and h are the Boltzmann and Planck constants, respectively. This part of the equation indicates how many species per unit of time attempt to reach the transition state. The factor $e^{\frac{\Delta S_0^{\ddagger}}{R}}$, in turn, reflects the influence of the activation entropy, showing that an increase in the change of entropy of the reactants towards the transition state increases the pre-exponential factor, thus increasing the rate. The term $e^{\frac{-\Delta H_0^{\ddagger}}{RT}}$ expresses the direct exponential dependence of the enthalpy of the transition state on the rate. The function $f(C_i)$ represents the dependence of the medium composition on the concentrations of the reacting species, which varies according to the reaction mechanism involved.

Comparing Equation 4.1 with the empirical Arrhenius equation:

$$k = \nu_{\mathrm{eff}} \cdot e^{-\frac{E_{\mathrm{act}}}{RT}} \tag{4.2}$$

it is possible to identify the corresponding kinetic parameters in terms of the thermodynamic quantities from TST (VAN SANTEN and NIEMANTSVERDRIET, 1995):

$$\nu_{\mathrm{eff}} = \frac{k_B T}{h} \cdot e^{\frac{\Delta S_{\mathrm{act}}}{R}} \tag{4.3}$$

$$E_{\mathrm{act}} = \Delta H_0^{\ddagger} + RT \tag{4.4}$$

where $\Delta S_{\mathrm{act}} = \Delta S_0^{\ddagger} + R$. The larger the difference between the activation complex and that of the reactant, the larger the rate of the reation. When the activation energy is low, the rate of reaction is maximum when the entropy of the activated complex in the transition state is maximum (VAN SANTEN and NIEMANTSVERDRIET, 1995). These relations establish a direct connection between the experimentally derived kinetic parameters and the thermodynamic

properties of the transition state. While ν_{eff} reflects the effective frequency with which reactants access the transition state — modulated by entropy —, the activation energy E_{act} is slightly higher than the enthalpy of activation due to the temperature dependence of the pre-exponential term. A full derivation of E_{act} and ν_{eff} is provided in Appendix C.

It is essential to emphasize that *a priori* the 4.3 and 4.4 relations are derived for elementary reactions in which the reaction occurs in a single step. Indeed, when measuring the overall rate of a process involving multiple competing elementary steps, significant variations are observed in activation barriers and experimental prexponential factors compared to the corresponding values in individual elementary steps (NØRSKOV *et al.*, 2014). In the studied case, for example, the reaction involves multiple elementary steps including a plethora of competing and sequential reactions, potentially leading to deviations from the predicted behavior, particularly in the interpretation of pre-exponential factors. In fact, based on Equations 4.1 and 4.3, the pre-exponential factor A assumes the form in Equation 4.5.

$$r = v_{\text{eff}} \cdot f(C_i) \cdot e^{-\frac{E_{\text{act}}}{RT}} = Ae^{-\frac{E_{\text{act}}}{RT}} \tag{4.5}$$

Hence, $\bar{A}$ depends on the individual ν_{eff} — consequently, on their respective entropies of each transition state, and T — and on the mechanism, as described in Equation 4.6.

$$\ln \bar{A} = \ln g \left(\nu_{\text{eff}}^{TS1}, \nu_{\text{eff}}^{TS2}, ..., \nu_{\text{eff}}^{TSN}, f(C_i)\right) \tag{4.6}$$

where $\bar{A}$ is the prexponencial factor estimated for a non-elemetary reaction. Although no explicit functional form for g has been established in the literature, the effective prefactors $\nu_{\text{eff}}^{TS_i}$ were presented to be intrinsically related to the activation entropies of the respective transition states ($i = 1, \ldots, N$), as expressed in Equation 4.3 (VAN SANTEN and NIEMANTSVERDRIET, 1995). On the other hand, the parameter E_{app} — an estimated (or observed) parameter for a non-elementary reaction — appears to be associated exclusively with the activation enthalpies of the transition states, corrected by RT. For this parameter in particular, MAO and CAMPBELL (2019) have derived an intuitive and applicable expression for complex mechanisms with multiple steps, as presented in Equation 4.7.

$$E_{\text{app}} = RT + \sum_i X_i H_i^0 \tag{4.7}$$

The second term corresponds to the sum of the standard state enthalpies of all species present in the reaction mechanism (intermediates, transition states, and products), each weighted by its own Degree of Rate Control (DRC) – X_i. DRC

quantifies the sensitivity of the net reaction rate with respect to the standard-state Gibbs free energy of species i, and is defined as:

$$X_i = \left(\frac{\partial \ln r}{\partial \left(-G_i^\circ / RT\right)} \right)_{G_{j \neq i}^\circ} \tag{4.8}$$

where r is the net reaction rate, G_i° is the standard-state Gibbs free energy of species i, and T is the temperature. This partial derivative is evaluated while keeping the standard-state Gibbs free energies of all other species constant.

Table 4.2 shows that the estimated activation energy for the formation of the main products AcO, ET and BuOH is lower for the catalyst MgO-w, while for the other catalysts E_{app} are around 250 kJ mol^{-1}. Assuming that the mechanism leading to these products is the same for all catalysts, catalyst MgO-w appears to exhibit lower individual enthalpy contributions for the species with the highest coverage, according to Equation 4.7. Initially, this result may seem unexpected, as a reaction with lower activation energy would typically be expected to proceed at a higher rate. However, catalyst MgO-w is the least active among the three, as shown in Figure 4.10. This behavior can be explained by the compensatory effect observed among the estimated constants presented in Table 4.2: the higher the E_{app}, the higher the $\bar{A}$. This suggests that the low rate observed for Mg-w is due to a reduction in entropic function g.

The Kinetic Compensation Effect (KCE) between the two Arrhenius parameters is relatively common and has already been reported by MCKENZIE *et al.* (1992) for isopropanol dehydrogenation over HTO. However, the criteria for classifying the different types of KCE remain poorly defined. As discussed by GALWEY and MORTIMER (2006), distinct forms of KCE may arise from sets of heterogeneous reactions that share chemical features but differ in catalysts, reactants, or experimental conditions. In the present case, three distinct catalysts (MgO-p, MgO-f, and MgO-w) — composed exclusively of pure MgO — have been employed for the same reaction under constant conditions, and a direct correlation between the parameters has been observed. According to the classification proposed by GALWEY and MORTIMER (2006), this behavior corresponds to a type 1HC KCE, in which different catalysts promote the same reaction. This indicates that the compensation effect may reflect systematic variations in the pre-exponential factors associated with surface differences among the catalysts.

It is understood that the KCEs are thermodynamically explained within the framework of TST due to the strong correlation between the two Arrhenius parameters. That is, the link between the entropy and enthalpy parameters is the fundamental Gibbs free energy relation, as suggested during the derivation of expressions 4.3 and 4.4, and this may explain the observed correlation between the

parameters.

SCHWAAB *et al.* (2008) argues that variable correlation should only be considered when it can be evaluated experimentally, independently of the parameter estimation procedure. Therefore, the experimental determination of the covariance matrix through replicate measurements should be considered for future studies, as it allows for the independent definition of the experimental error structure and the determination of confidence regions for the estimated parameters.

At this stage, the structure of MgO-w appears to have reduced the entropy variation of one or more transition states, which may have hindered reactions such as the dehydrogenation of EtOH to AcO and C–C coupling. This is once again understood by the fact that this material exhibits fewer structural defects and greater isotropy along the crystal lattice.

4.4 Surface Reactivity

This section presents and discusses the DRIFTS-MS results for the MgO-p and MgO-w catalysts, focusing on their comparison due to the similar catalytic behavior between MgO-f and MgO-p. The discussion is divided into two parts: (i) analysis of surface hydroxyl groups, (ii) the remaining vibrational modes.

4.4.1 Hydroxyl groups

The DRIFTS spectra results for MgO-p and MgO-w are presented in Figure 4.14. The bands for both cases are somewhat similar. At 303 K, with freshly adsorbed EtOH, the spectra exhibit broad and weakly intense bands around 3500 cm^{-1} – 3100 cm^{-1}, assigned to non-dissociated EtOH interacting via hydrogen bonding (CHIEREGATO *et al.*, 2015; DE SOUZA *et al.*, 2020; TAIFAN *et al.*, 2017b), known as molecular hydroxyls. In the adjacent region, both cases display a broad band in the 3700 cm^{-1} – 3400 cm^{-1} range, attributed to hydrogen-bonded multi-coordinated hydroxyls (TAIFAN *et al.*, 2017b). In the higher energy region, at least three peaks (3750 cm^{-1}, 3733 cm^{-1}, and 3715 cm^{-1}) are observed for MgO-p, and a similar pattern appears for MgO-w, assigned to more basic hydroxyl groups (TAIFAN *et al.*, 2017b).

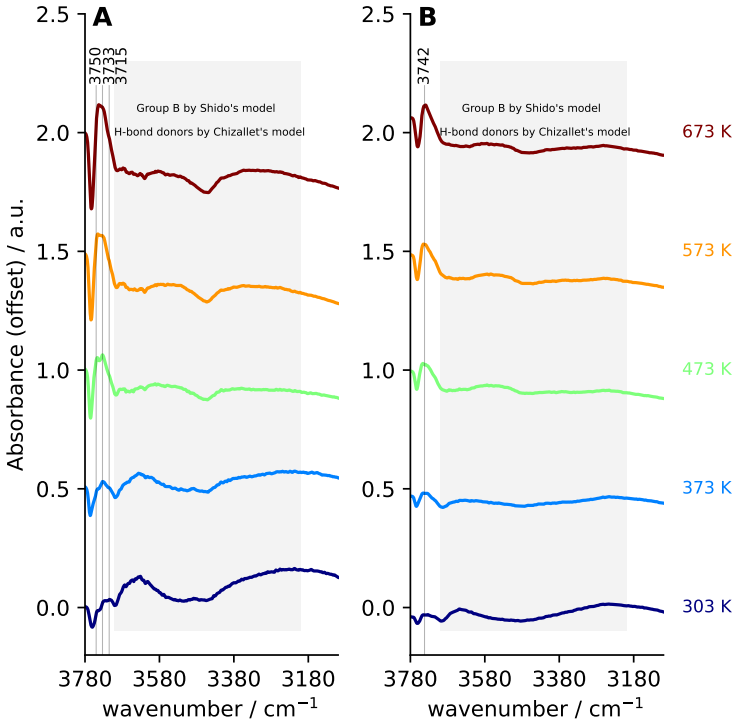

Figure 4.14: DRIFTS spectra (3780 cm^{-1} – 3100 cm^{-1}) as a function of temperature for a) MgO-p, and b) MgO-w

Notes: Highlighted bands represent the discussed features.

All vibrational modes observed at 303 K, although present in the spectrum obtained for MgO-w, are more prominent in MgO-p. This finding is somewhat intriguing, as it suggests that EtOH adsorbs differently on each of the two structures. All bands are identified as stretching vibrational modes of hydroxyl groups ($\bar{\nu}(OH)$) (CHIZALLET *et al.*, 2007; DE SOUZA *et al.*, 2020), although their exact assignment has been debated since the 1960s in studies involving water adsorption/desorption over MgO (ANDERSON *et al.*, 1965; CHIZALLET *et al.*, 2007; COLUCCIA *et al.*, 1988, 1987; KNÖZINGER *et al.*, 1993; MORROW, 1990; SHIDO *et al.*, 1989; TSYGANENKO and FILIMONOV, 1973). For instance, most classic works assume the presence of only two types of OH groups, as illustrated in Anderson-Shido's model (Figure 4.15). Group A corresponds to the sharp peaks above 3700 cm^{-1}, assigned to hydroxyls bound to Mg^{2+}. Group B, in turn, in the 3700 cm^{-1} – 3200 cm^{-1} range, corresponds to hydroxyl groups bound to O^{2-} ions (ANDERSON *et al.*, 1965; SHIDO *et al.*, 1989). Due to their proximity to the surface, group B hydroxyls are more sensitive to hydrogen bonding (TAIFAN *et al.*, 2017a).

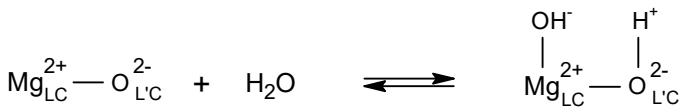

Figure 4.15: Representation of A and B hydroxyl groups based on Anderson-Shido's model

Notes: A with L=5, 4 or 3, and B with L'= 3, 4, 5. CHIZALLET *et al.* (2007); SHIDO *et al.* (1989)

In this work, a progressive increase in the intensity of type A hydroxyls is observed up to 573 K, accompanied by a corresponding decrease in type B hydroxyls. Additionally, the higher-frequency portion of group B shifts to lower wavenumbers (red shift), whereas the lower-frequency portion shifts to higher wavenumbers (blue shift). According to the model proposed by SHIDO *et al.* (1989), the wavenumbers of hydroxyl bands in group B can be correlated with the coordination of the surface O^{2-}_{LC} ion on which they are formed, as follows:

$$\bar{\nu}(O_{3C}{-}H) > \bar{\nu}(O_{4C}{-}H) > \bar{\nu}(O_{5C}{-}H) \tag{4.9}$$

In this context, Figure 4.14 reveals that as the temperature increases moderately coordinated hydroxyls, such as O_{4C}-H, become predominant. A similar analysis can be applied to the triplet around 3700 cm^{-1}, since the trend for type A hydroxyls follows:

$$\bar{\nu}(Mg_{5C}O - H) > \bar{\nu}(Mg_{4C}O - H) > \bar{\nu}(Mg_{3C}O - H) \tag{4.10}$$

Thus, the results indicate an increase in the presence of Mg_{5C}-OH and Mg_{4C}-OH hydroxyls with increasing temperature.

The same trend observed up to 573 K, as previously discussed, also occurs for catalyst MgO-w, although in a much more subtle manner. Catalyst MgO-p, therefore, exhibits a higher concentration of moderately coordinated group B hydroxyls (L' = 4) and highly coordinated type A hydroxyls (L = 5 and 4). This difference might be related to differences in surface defects between the two structures, which is consistent with the PXRD results.

For MgO-p, at higher temperatures (573 K and 673 K), an increase is observed in the band attributed to molecular hydroxyls — and/or O_{4C}-H —, which is likely related to surface products (or intermediates) containing this functional group, while for MgO-w this band is almost absent. Furthermore, the in situ mass desorption profiles (Figure 4.16) show that the desorption of C_4 oxygenated products — such as BuOH and (E)-CrO — is slightly higher for MgO-p than for MgO-w, confirming its

greater reactivity. These results are also consistent with those obtained in catalytic tests, where MgO-w is significantly less active for these products than MgO-p.

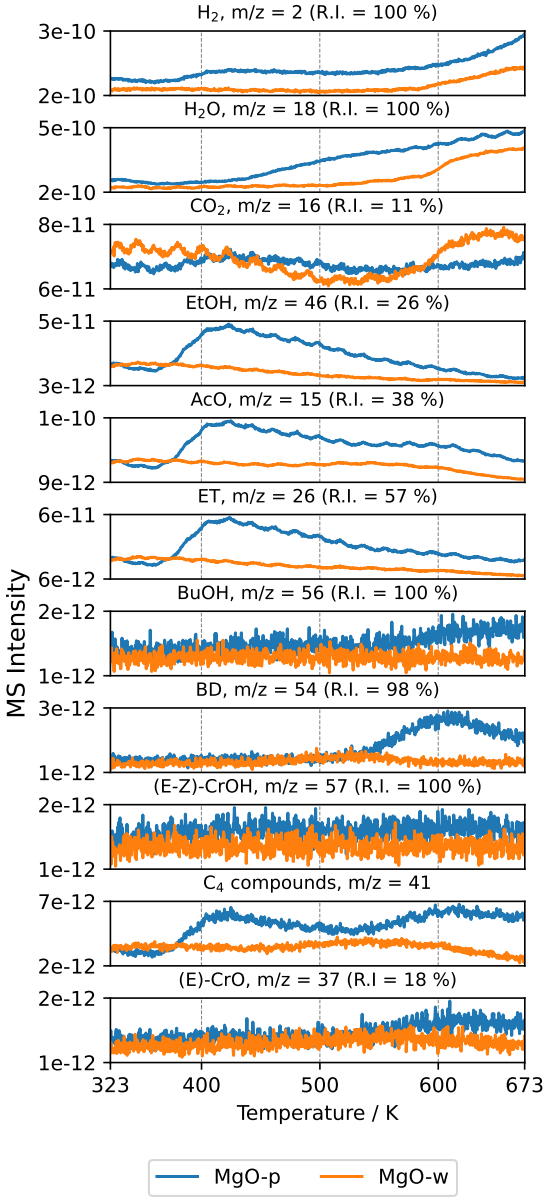

Figure 4.16: Intensity profiles of mass signals (DRIFTS-MS in situ) during the desorption and reaction of EtOH over catalysts MgO-p and MgO-w.
R.I. (relative intensity) corresponds to the relative intensity observed for an ion with a specific mass-to-charge ratio (m/z) in a mass spectrum. This value is expressed as a percentage of the intensity of the most intense peak in the spectrum, which is defined as 100%. Thus, an R.I. of 100% indicates that the corresponding ion is the most abundant in the spectrum. The selection of fingerprint fragments for each product was based on a preliminary analysis of Figure D.1. Many products share similar fragments, and thus, they were omitted here. C_4 products represent a pool of compounds: mainly butenes + BuO + CrOH.

It is important to note that there are more recent models than those proposed by ANDERSON *et al.* (1965); SHIDO *et al.* (1989). For instance, the model

proposed by CHIZALLET *et al.* (2007) considers that the type B OH groups from the Anderon-Shido' model are hydrogen bond donors, meaning that the hydrogen atom participates in a hydrogen bond with another hydroxyl group. Furthermore, CHIZALLET *et al.* (2007) argues that the correlation between coordination number and the wavenumber of the bands is not as straightforward as suggested by ANDERSON *et al.* (1965); SHIDO *et al.* (1989).

All hydrogen-bond donor OH groups are characterized by low frequencies and correspond to the broad band observed experimentally, as indicated in Figure 4.14. These groups include: O_{3C}–H (located at corners), O_{4C}–H (found at steps and corners), and O_{5C}–H (present in valleys). In contrast, the hydrogen-bond acceptor OH groups, such as O_{1C}–H and O_{2C}–H, are associated with a narrow high-energy band (around 3750 cm^{-1}) and involve only isolated OH groups (O_{2C}–H, O_{3C}–H, and O_{4C}–H). This contradicts the previously accepted interpretation shown in Equation 4.10, which suggested that only "linear" O_{1C}–H groups exhibit high frequencies.

Considering the previous assignments, it is observed that, as the temperature increases, the MgO-p catalyst appears to contain a higher concentration of hydrogen-bond donor groups associated with corners, steps, and valleys, which explains its higher reactivity comparing to MgO-w. This observation is consistent with the calculations by DE SOUZA *et al.* (2020), which indicate that low-coordinated sites located at kink-corner and step-side positions are energetically more favorable for EtOH activation. The supercell used in DFT calculation contains O_{4C} anions, which act as Brønsted basic sites during the dissociation of EtOH, promoting the formation of ethoxide and the OH group (O_{4C}–H), identified as a hydrogen donor by CHIZALLET *et al.* (2007), and as B group by SHIDO *et al.* (1989).

4.4.2 Remaining Vibrational Modes

The remaining DRIFTS spectra are shown in Figure 4.17 and reveal similar vibrational modes for MgO-p and MgO-w. At 303 K, the first region displays bands between 3000–2700 cm^{-1}, assigned to symmetric and asymmetric stretching modes of methyl and methylene groups (DAVYDOV, 2003a; PACHECO, 2019; SILVERSTEIN *et al.*, 2010), associated with non-dissociated EtOH and surface ethoxide.

In the second region, the precise assignment of vibrational modes is complex. At 303 K, between 1050 cm^{-1} and 1150 cm^{-1}, three bands are observed, attributed to $\bar{\nu}$(CC), $\bar{\nu}$(CO), and $\bar{\nu}$(CCO) modes of ethoxide (BIRKY *et al.*, 2013; CARVALHO *et al.*, 2013; CHIEREGATO *et al.*, 2015; PACHECO, 2019). However, CHIEREGATO *et al.* (2015) did not detect the band at 1146 cm^{-1} (for freshly adsorbed EtOH) at 303 K, only at higher temperatures. This led the authors to

propose that this mode corresponds to a reaction intermediate other than ethoxide. DFT calculations in that study suggest the 1146 cm^{-1} mode represents $\bar{\nu}$(CO) of a carbanion species formed via proton abstraction from the methyl group. This is counterintuitive, since it is unlikely that such a reactive species would form at such a low temperature. Moreover, the authors reported that at 673 K the band undergoes a blue-shift to 1124 cm^{-1} (CHIEREGATO *et al.*, 2015), consistent with the spectrum of MgO-w (Figure 4.17b) but not with MgO-p (Figure 4.17a).

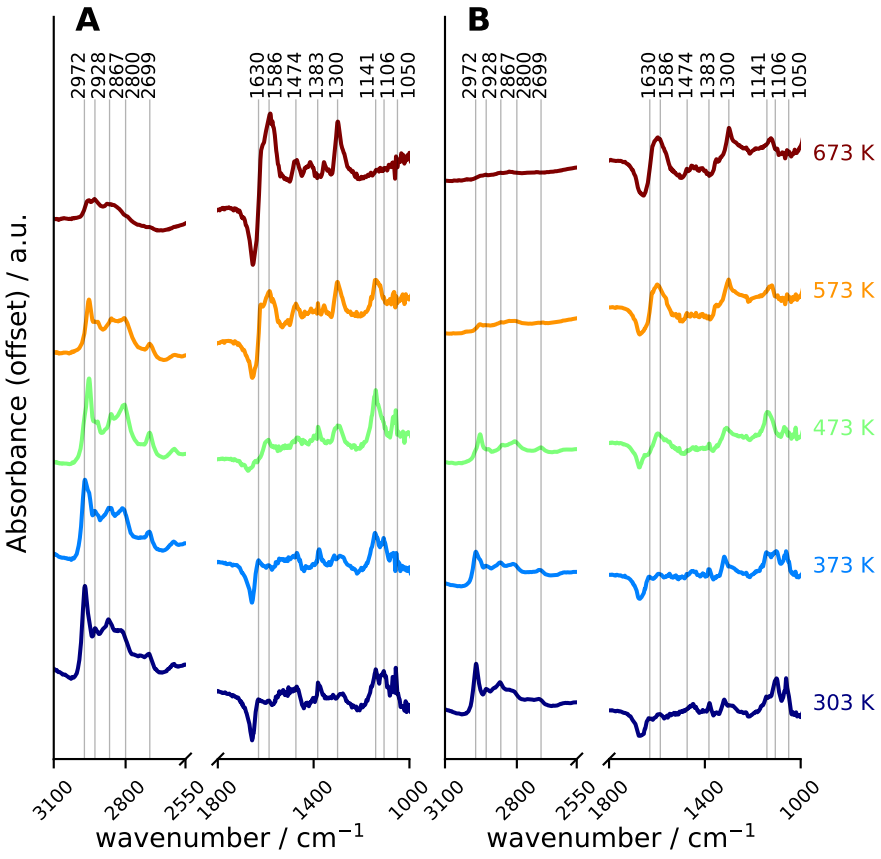

Figure 4.17: DRIFTS spectra (3100-1000 cm^{-1}) as a function of temperature for a) p-, and b) w-MgO

Highlighted bands represent the discussed features.

As the temperature increases (373 K – 673 K), the stretching bands associated with methyl and methylene groups gradually decrease for both MgO-p and MgO-w. This trend suggests the desorption of EtOH and/or the reaction of ethoxide species into products that desorb from the surface, in agreement with the detection of certain products (e.g., CrOH, (E)-CrO, AcO) at this temperature in the mass spectrum (Figure 4.16). However, at 573 K, only a few CH_2 and CH_3-containing species remain on the surface of MgO-w. This observation suggests that the bands around 1474 cm^{-1} and 1383 cm^{-1} can be attributed, respectively, to the asymmetric and symmetric bending modes of the CH_3, since these bands, as well as the stretching

modes of the same group, remain pronounced for MgO-p but not for MgO-w at 673 K. In general terms, this result corroborates the lower surface reactivity of MgO-w compared to MgO-p.

In the range of 473 K to 673 K, CHIEREGATO *et al.* (2015); DE SOUZA *et al.* (2020) have attributed the broad band around 1600 cm^{-1} to the formation of surface species containing C=C bonds, such as CrOH and CrO. CHIEREGATO *et al.* (2015) experimentally observed a band near 1620 cm^{-1} above 523 K in adsorption experiments of CrOH on MgO. The increase in intensity of this band with rising temperature has been associated with the formation of unsaturated intermediates, a hypothesis supported by high-temperature adsorption experiments and subsequent product detection by DRIFTS-MS. Later, DE SOUZA *et al.* (2020) complemented these findings through theoretical simulations of vibrational spectra, identifying C=C vibrational modes at 1509 cm^{-1} (CrO) and 1647 cm^{-1} (CrOH), which are 17 cm^{-1} higher than those observed here for MgO-p and MgO-w. Moreover, both the in situ mass spectra (Figure 4.16) and the catalytic test results (Figure B.2) indicate the formation of unsaturated by-products such as BD, CrOH, and CrO. The formation of these species has been more pronounced for the MgO-p sample compared to MgO-w, especially above 573 K in the mass spectra and at 723 K in the catalytic test. These results are consistent with the higher intensity of the C=C stretching band observed in the in situ spectra for MgO-p, indicating that this sample favors reaction pathways involving the formation of unsaturated intermediates.

4.5 Nanoscale Probing of Local Chemical Composition

4.5.1 Localized Measurements

This subsection presents the localized measurements obtained by SINS for the MgO catalysts. Due to the specific morphological features of the wire-like sample (MgO-w), this technique could not be applied to this material. The tip oscillation height required for proper operation was incompatible with the vertical extension of the wire structures, preventing effective signal acquisition.

4.5.1.1 MgO-p

SINS enabled the analysis of samples using the s-SNOM method, resulting in near-field images. Then, IR spectra were obtained from small regions of these same images, each about 20 nm in size. Figure 4.18 displays the topography of MgO-p obtained by AFM throughout the steps of the EETPD method on Au substrate.

The corresponding images of near-field reflectivity are adjacent. MgO-p particles can be identified by the higher areas in the AFM and also by the lower reflection of the sample compared to the highly reflective background of the Au substrate.

In Figure 4.18, the square-marked areas (not scaled) represent the selected regions for point spectral scanning. Figure 4.19 presents the respective point spectra associated with the highlighted square regions. In order to properly process the results, both the amplitude and phase spectra must be evaluated simultaneously, especially the phase spectrum. Phase spectrum is what actually contains the vibrational modes equivalent to the conventional far-field spectra (HUTH *et al.*, 2012; MESTER *et al.*, 2020). Mathematically, phase $\varphi_n(\omega)$ represents the imaginary part of the scattering coefficient $\Im[\sigma_n(\omega)]$, which relates the scattered field $E(\omega)$ to the incident field E_i according to $E(\omega) = \sigma(\omega)E_i(\omega)$. The amplitude $S_n(\omega)$, on the other hand, corresponds to the real part $\Re[\sigma_n(\omega)]$. Hence, the amplitude spectrum is usually correlated with the phase spectrum and assists in identifying relevant phase bands by observing the amplitude valleys.

The spectrum at 323 K in Figure 4.19 corresponds to the MgO-p sample immediately after EtOH adsorption. So far, there is no clear evidence regarding the vibration modes related to absorbed EtOH. However, the exact same sample shown vibrational features associated with organic species bonded to MgO by micro-FTIR measurement, even after desorption up to 673 K, as illustrated in the attached Figure E.1. This result suggests that either the SINS probed region did not adsorb EtOH, or due to a very low concentration, the vibrational modes attributed to ethoxide, between 1050^{-1} and 1150 cm^{-1} were not sufficient to produce a detectable spectral signal, even when using synchrotron radiation.

The absence of EtOH vibrations is unsurprising since the SINS uses a small sample amount compared to more common bulk spectroscopic methods such as DRIFTS. This implies significantly fewer vibrational contributions for SINS compared to the other mid-IR characterizations due to the smaller sample amount. Thus, the amount of sample — and consequently, less pronounced bands — imposes a limitation on the technique. However, as mentioned earlier, the advantage of the SINS technique is the potential for local probing, but only if there are significant molecular vibrations to be excited in the probed region.

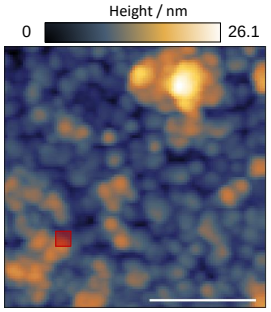

(a) 673 K, SB: 400 nm

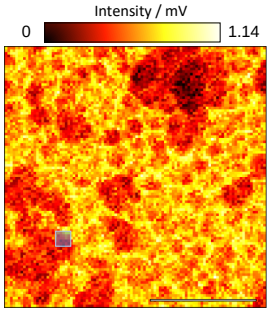

(b) 673 K, SB: 400 nm

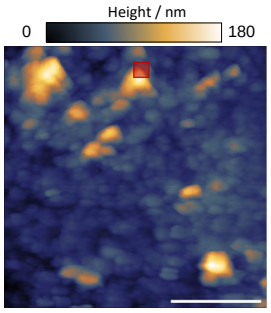

(c) 623 K, SB: 1000 nm

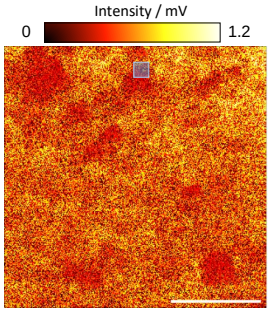

(d) 623 K, SB: 1000 nm

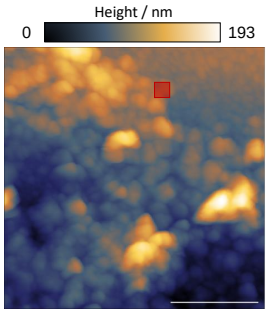

(e) 573 K, SB: 1000 nm

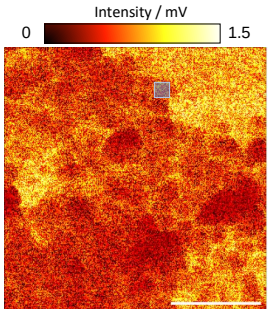

(f) 573 K, SB: 1000 nm

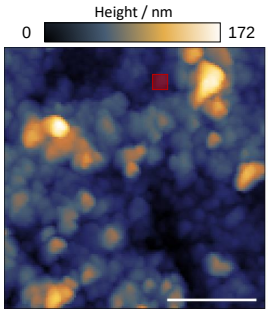

(g) 423 K, SB: 1000 nm

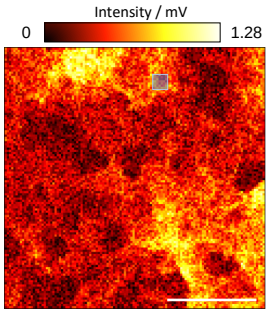

(h) 423 K, SB: 1000 nm

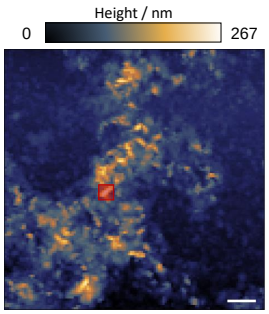

(i) 323 K, SB: 1000 nm

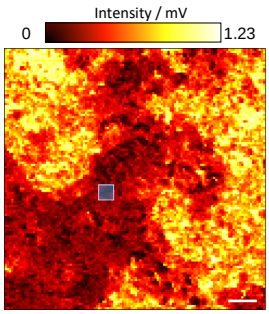

(j) 323 K, SB: 1000 nm

Figure 4.18: AFM topography (left) and broadband near-field reflectivity $|S_2|$ (right) images for MgO-p

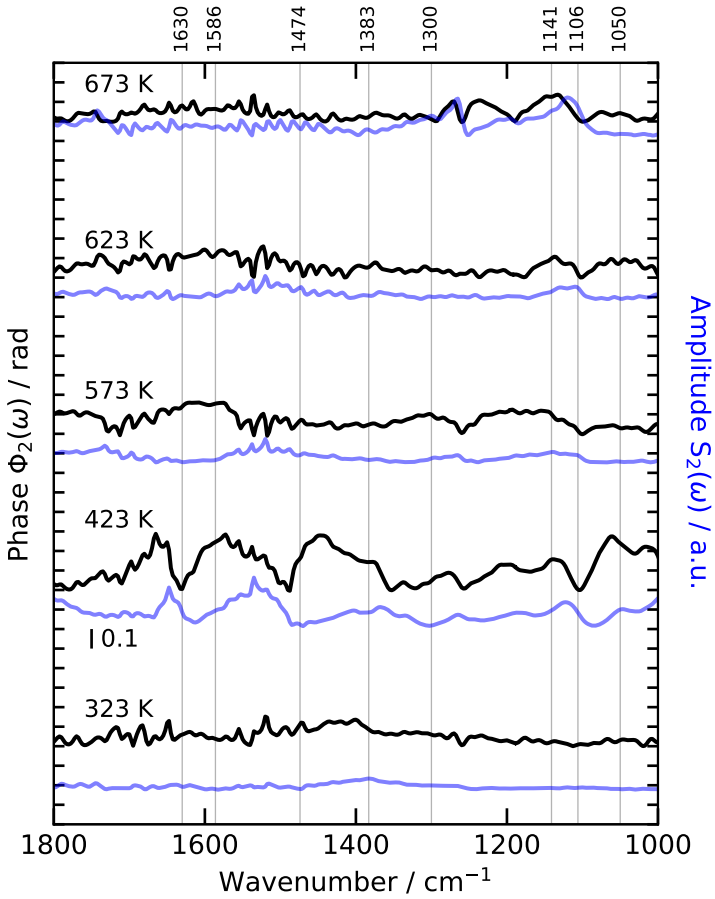

Figure 4.19: SINS phase and amplitude spectra for MgO-p exposed to the EETPD protocol - experiment 1

Highlighted wavenumbers represent the discussed features in the second part of the DRIFTS spectra presented in Figure 4.17a.

The spectrum recorded after the treatment at 423 K reveals some vibrational features. The range of 1300 cm^{-1} – 1500 cm^{-1} cm^{-1}, distinct bands at approximately ≈1360 cm^{-1} and ≈1300 cm^{-1} can be attributed to the bending and wagging frequencies of C–H_3 and C–H bonds, respectively. DE SOUZA *et al.* (2020) simulated spectra of adsorbed EtOH and AcO dimers, as well as of a new H bond-activated intermediate, referred to as oxametallacycle-like intermediates. Among these, in the simulated spectrum of the AcO dimer, the wavenumber regions at 1332 cm^{-1} and 1350 cm^{-1} can be attributed to the bending modes of C–H and C–H_3, respectively. Examining spectra taken at temperatures above 423 K, one can observe the absence of the previously mentioned bands between 1300 cm^{-1} and 1500 cm^{-1}. However, it should be noted that this assignment is not very precise, as the phase spectrum obtained by SINS commonly exhibits a slightly different band profile compared to both the far field FTIR spectra and the simulated ones.

The low-frequency bands (1050 cm^{-1} – 1150 cm^{-1}) can also be assigned to the

stretching modes expected for ethoxide, as observed in the DRIFTS spectrum. It is noted that the intensity in this region is relatively low compared to the surrounding regions, as shown in Figure 4.18g. Therefore, the SINS spectrum obtained from the this particle is considered the only one that exhibited an interpretable organic vibrational response. It is known that vertical variation in the AFM affects both the intensity and the spectral position of the vibrational peaks detected by nano-FTIR (KRUTOKHVOSTOV *et al.*, 2012; MESTER *et al.*, 2020). These variations do not arise from chemical changes, but rather from the probing depth and the near-field profile of the s-SNOM. Additionally, signal modulation at different harmonics (n = 3, 4) strongly depends on the oscillation amplitude, affecting both the probing depth and the spectral resolution. MESTER *et al.* (2020) have demonstrated that surface and subsurface layers can be distinguished by analyzing the ratio of peak heights obtained at different demodulation orders n. Since the sample in the present study exhibits a markedly heterogeneous height profile, it is expected that the spectral response differs for a second-order harmonic.

4.5.1.2 MgO-f

The same analysis was performed for the MgO-f catalysts. Figure 4.20 depicts all the topography and s-SNOM images after the EETPD steps. The point spectra appear to differ from those observed for MgO-p material, such as the two prominent peaks at 423 K and 573 K. However, this band seems too broad to be a set of vibrational modes and has thus been disregarded, as it may result from overlapping signals, background contributions, or surface interactions.

After adsorption, vibrational patterns centered at 1200 cm^{-1} and 1000 cm^{-1} have been observed. Once again, assigning these bands to expected vibrational modes of EtOH adsorbed on MgO remains uncertain. This limitation also applies to other analyzed spectra. The only signal that appears to correspond to a well-defined vibrational absorption event is a peak observed between 1300 cm^{-1} and 1200 cm^{-1} after desorption at 423 K. However, this feature could not be assigned to any specific vibrational mode based on the literature.

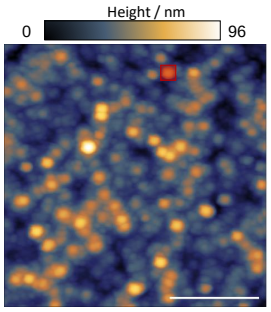

(a) 673 K, SB: 1000 nm

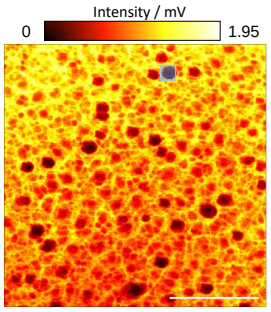

(b) 673 K, SB: 1000 nm

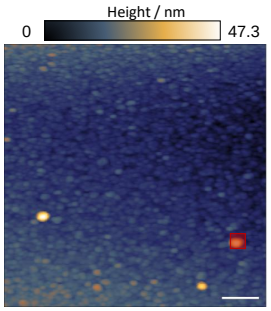

(c) 623 K, SB: 400 nm

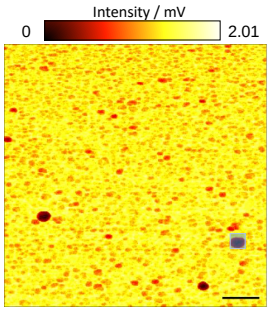

(d) 623 K, SB: 400 nm

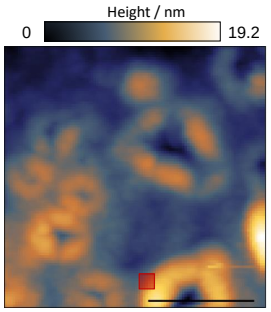

(e) 573 K, SB: 400 nm

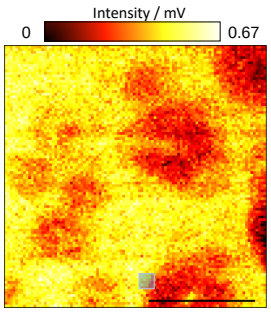

(f) 573 K, SB: 400 nm

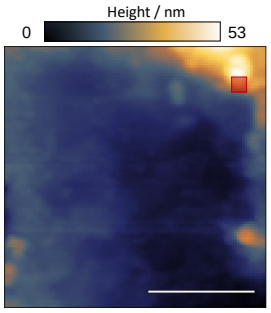

(g) 423 K, SB: 400 nm

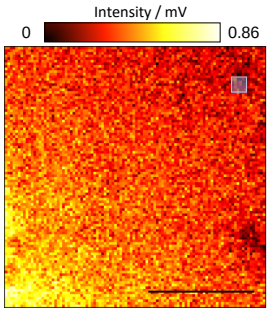

(h) 423 K, SB: 400 nm

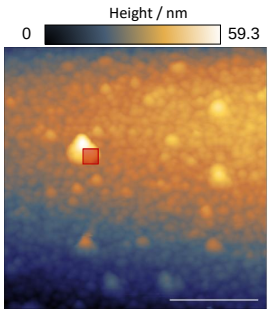

(i) 323 K, SB: 1000 nm

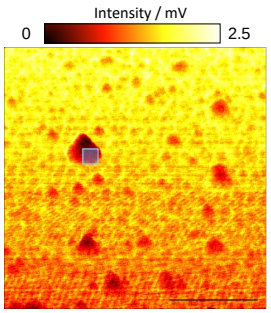

(j) 323 K, SB: 1000 nm

Figure 4.20: AFM topography (left) and broadband near-field reflectivity $|S_2|$ (right) images for MgO-f

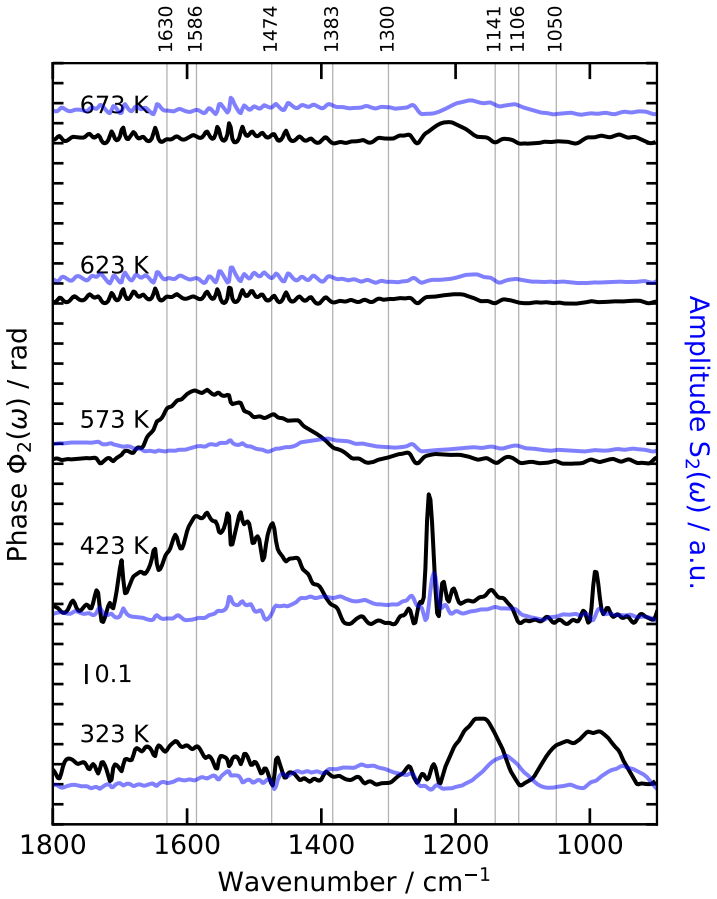

Figure 4.21: SINS phase and amplitude spectra for MgO-f exposed to the EETPD protocol - experiment 1

Highlighted wavenumbers represent the discussed features in the second part of the DRIFTS spectra presented in Figure 4.17a.

4.5.2 Surface Mappings

The previous experiment indicated that few vibrational modes were captured. The main explanation for this is the probe's small order of magnitude: $\approx$ 20 nm. That is, without area probing, it is difficult to correlate the vibrational mode with the structural characteristics, such as the shape and topographic features of the probed particle. Therefore, new EETPD experiments were performed, this time conducting SINS measurements over a 700 nm x 700 nm region.

Figure 4.22a shows an MgO particle after the EtOH adsorption protocol, while Figure 4.22b displays the spectra from the first image, specifically those from row 2 indicated in Figure 4.22a. Only two vibrational features are observed in these measurements: between 1800 cm^{-1} and 1400 cm^{-1}, related to vibrational modes attributed to atmospheric water vapor absorption; and the broad band between 1200 cm^{-1} and 1000 cm^{-1}, assigned to the Si substrate (BECHTEL *et al.*, 2020; HAVA

et al., 2001). Both signals are difficult to suppress with background discount. In other words, it is not possible to ascribe any vibrational modes to organic surface species related to the chemisorption of EtOH. For registration purposes, Appendix F contains all the SINS measurements along the particle shown in Figure 4.22a.

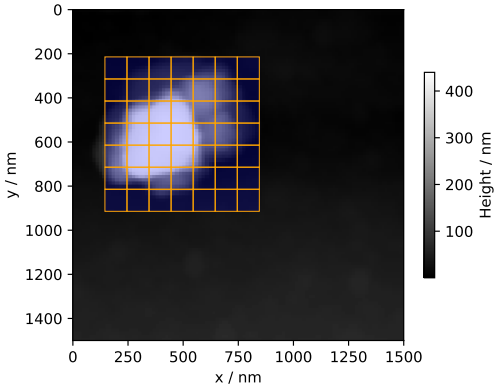

(a) AFM

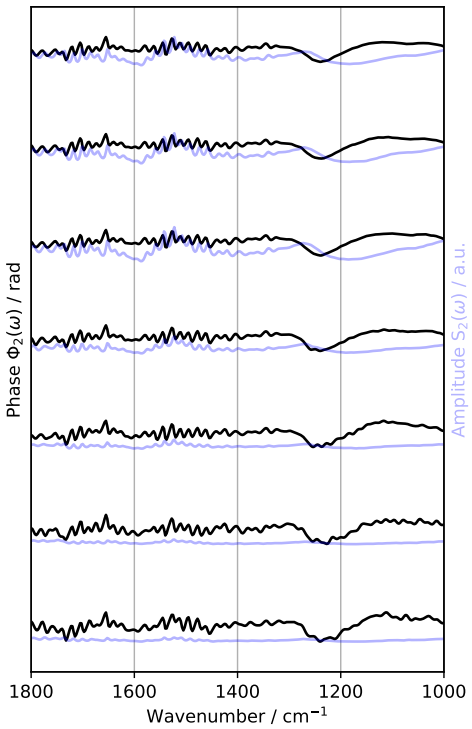

(b) SINS measurements. Spectra (bottom to top) correspond to square positions (left to right) in the second row highlighted in subfigure 4.22a.

Figure 4.22: Mapping by SINS of an MgO-p particle after EtOH adsorption using the EETPD method.

The area measurements required a relatively long acquisition time, totaling approximately five hours for the 49 collected spectra. Initially, the particle was located using AFM, and a spectrum was subsequently recorded for each selected region. Due to instrumental limitations, it was not possible to simultaneously monitor both the microscopic and spectroscopic signals in real time. As a result, there was no direct confirmation that the spectral acquisition occurred precisely over the particle. Although simultaneous measurements were not feasible, the equipment setup provided height data at the end of each scan, offering an indirect indication of whether the spectrum was collected from the intended region. Figure 4.23 presents the height profiles obtained before and after the SINS experiments. The observed height variations suggest that the measurements were not performed directly on the particle, which may explain the absence of characteristic vibrational modes

associated with EtOH adsorbed on MgO.

Finally, it is important to highlight that the measurements presented in this thesis were carried out on relatively large (700 nm x 700 nm x 400 nm) particles of polycrystalline MgO, a powdered material — the same material as what is employed in catalytic tests and other characterization methods — suspended in water and deposited onto an Au substrate. Studies in heterogeneous catalysis that have employed SINS usually adopt sophisticated methodologies for preparing model catalysts (SAY *et al.*, 2022; SZOSTAK *et al.*, 2019; WU *et al.*, 2017), using materials specifically developed for the experiment. This may contribute to the limited adoption of this type of characterization in catalytic studies (LI *et al.*, 2023).

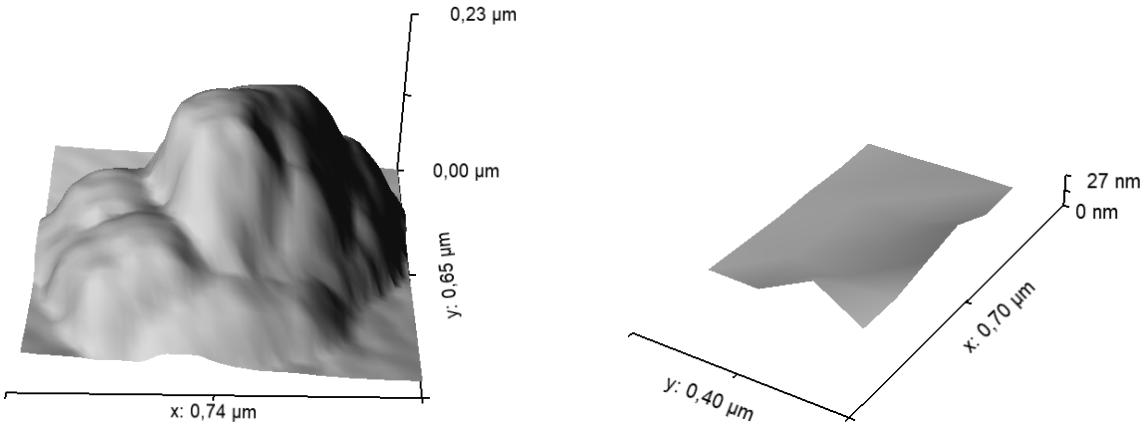

(a) Before spectral measurements

(b) After spectral measurements

Figure 4.23: AFM images of the particle (a) before and (b) after the spectral measurements.

Note: The height after the SINS measurement is inconsistent with the first image. It is therefore likely that the measurements were not performed on the originally selected particle, preventing a reliable analysis.

Chapter 5

Conclusions

This thesis investigated the influence of the morphology of pure MgO catalysts on the EtOH upgrading to BuOH and other products. Three catalysts with distinct structural characteristics were prepared: flower-like particles (MgO-f), wire-like structures (MgO-w), and a reference material with no controlled morphology (MgO-p). Detailed physicochemical characterization showed that morphology directly affects the crystalline structure, surface area, and defect distribution. This was especially evident in MgO-p, which exhibited the highest specific surface area and the smallest average crystallite size, possibly due to the absence of morphological control during its preparation – a factor that also resulted in broader XRD peaks and increased structural disorder.

Catalytic tests demonstrated that morphology affects BuOH yield, and these variations can be linked to the structural differences observed. MgO-p and MgO-f exhibited BuOH specific yields of 1.65×10^{-3} and 1.79×10^{-3} m^{-2}, respectively, which represent increases of approximately 205 % and 231 % compared to MgO-w (5.41×10^{-4} m^{-2}). The EtOH-to-BuOH reaction over MgO is structure-sensitive. This observation is consistent with predictions from first-principles theoretical studies. This is because the specific catalytic performance varied among the samples, reflecting the direct influence of structural defects such as dislocations and edge terminations, which may stabilize key intermediates or lower activation barriers. The microkinetic analysis, based on TST, enabled the estimation of activation energy and pre-exponential factor, revealing compensation effects between activation enthalpy and entropy embedded in these parameters.

In situ DRIFTS-MS revealed bands associated with hydroxyl groups, which are descriptors of surface atom coordination. Additionally, the origin of reaction intermediates was discussed, allowing inferences on coupling and dehydration mechanisms between MgO-p and MgO-w. However, some vibrational modes remain unknown, such as the two bands observed around 1600 cm^{-1}, whose assignment remains ambiguous and requires further investigation.

SINS results did not allow for a detailed discussion of the local reactivity of the catalysts, as originally intended. This limitation is mainly due to methodological challenges, including low spectral reproducibility across different regions of the sample and the complexity of distinguishing topographic and chemical contributions in phase and amplitude measurements. Overall, the absence of well-defined vibrational bands hindered the unequivocal identification of reaction intermediates with spatial resolution, limiting the progress of local analysis.

The results reinforce that the morphological structure of MgO catalysts directly affects their performance, not only by modifying the textural properties but also by altering the surface acid-base balance and the distribution of active sites through the insertion of defects. This work contributes to understanding the structural sensitivity of the EtOH coupling reaction, its mechanisms, and to the development of new catalysts with improved selectivity and efficiency, emphasizing that rational catalyst design must consider not only composition and crystallinity, but also morphology-driven defect engineering.

5.1 Suggestions for Upcoming Works

It is suggested that future investigations using the SINS technique be conducted on samples with oriented surfaces. There are reports in the literature on the preparation of single crystals oriented along the <100> (AMODEO *et al.*, 2018). Experiments using oriented MgO crystals EETPD and SINS could reveal via AFM measurements specific regions of low coordination, allowing for a more accurate identification of active sites and providing mechanistic insights into surface defects that remained partially unresolved in this work, particularly dislocation cores or step edges.

Another key point is the adoption of *operando* XRD experiments in order to determine whether phase transformations between periclase and brucite occur under reaction conditions, which may lead to the deactivation of active sites, for example, through the formation of hydroxylated layers that suppress basicity or active surface terminations.

Additionally, the simulation of IR spectra based on DFT calculations, combined with the development of new hierarchical catalysts, is recommended for elucidating the vibrational features of surface intermediates. This is especially relevant for interpreting the hidden modes in the fingerprint region of the mid-IR spectra — a region where overlapping bands hinder the unambiguous assignment of key oxygenates, such as enolates, unsaturated aldehydes, or alkoxide species.

References

ABDULRAZZAQ, H. T., SCHWARTZ, T. J., 2019, "Catalytic conversion of ethanol to commodity and specialty chemicals", *Ethanol*, pp. 3–24.

AL-GHAMDI, A. A., AL-HAZMI, F., ALNOWAISER, F., et al., 2012, "A new facile synthesis of ultra fine magnesium oxide nanowires and optical properties", *Journal of electroceramics*, v. 29, pp. 198–203.

AMODEO, J., MERKEL, S., TROMAS, C., et al., 2018, "Dislocations and Plastic Deformation in MgO Crystals: A Review", *Crystals*, v. 8, n. 6. ISSN: 2073-4352. doi: 10.3390/cryst8060240. Disponível em: <https://www.mdpi.com/2073-4352/8/6/240>.

ANDERSON, P. J., HORLOCK, R. F., OLIVER, J. F., 1965, "Interaction of water with the magnesium oxide surface", *Trans. Faraday Soc.*, v. 61, pp. 2754–2762. doi: 10.1039/TF9656102754. Disponível em: <http://dx.doi.org/10.1039/TF9656102754>.

BECHTEL, H. A., MULLER, E. A., OLMON, R. L., et al., 2014, "Ultrabroadband infrared nanospectroscopic imaging", *Proceedings of the National Academy of Sciences*, v. 111, n. 20, pp. 7191–7196.

BECHTEL, H. A., JOHNSON, S. C., KHATIB, O., et al., 2020, "Synchrotron infrared nano-spectroscopy and -imaging", *Surface Science Reports*, v. 75, n. 3, pp. 100493. ISSN: 0167-5729. doi: https://doi.org/10.1016/j.surfrep.2020.100493. Disponível em: <https://www.sciencedirect.com/science/article/pii/S0167572920300145>.

BIRKY, T. W., KOZLOWSKI, J. T., DAVIS, R. J., 2013, "Isotopic transient analysis of the ethanol coupling reaction over magnesia", *Journal of Catalysis*, v. 298, pp. 130–137. ISSN: 0021-9517. doi: https://doi.org/10.1016/j.jcat.2012.11.014. Disponível em: <https://www.sciencedirect.com/science/article/pii/S002195171200365X>.

BOUDART, M., 1969, "Catalysis by Supported Metals". In: Eley, D., Pines, H., Weisz, P. B. (Eds.), *Advances in Catalysis*, v. 20, *Advances in*

Catalysis, Academic Press, pp. 153–166. doi: https://doi.org/10.1016/S0360-0564(08)60271-0. Disponível em: <https://www.sciencedirect.com/science/article/pii/S0360056408602710>.

BRANDA, M. M., RODRÍGUEZ, A. H., BELELLI, P. G., et al., 2009, "Ethanol adsorption on MgO surface with and without defects from a theoretical point of view", *Surface Science*, v. 603, n. 8, pp. 1093–1098. ISSN: 0039-6028. doi: https://doi.org/10.1016/j.susc.2009.02.021. Disponível em: <https://www.sciencedirect.com/science/article/pii/S0039602809001824>.

BRANDA, M., FERULLO, R., BELELLI, P., et al., 2003, "Methanol adsorption on magnesium oxide surface with defects: a DFT study", *Surface Science*, v. 527, n. 1, pp. 89–99. ISSN: 0039-6028. doi: https://doi.org/10.1016/S0039-6028(03)00010-4. Disponível em: <https://www.sciencedirect.com/science/article/pii/S0039602803000104>.

BRASIL, H., BITTENCOURT, A. F., YOKOO, K. C., et al., 2021, "Synthesis modification of hydroxyapatite surface for ethanol conversion: The role of the acidic/basic sites ratio", *Journal of Catalysis*. doi: 10.1016/j.jcat.2021.08.050. Disponível em: <https://doi.org/10.1016/j.jcat.2021.08.050>. Received 26 June 2021, Revised 25 August 2021, Accepted 30 August 2021.

BREHM, M., TAUBNER, T., HILLENBRAND, R., et al., 2006, "Infrared Spectroscopic Mapping of Single Nanoparticles and Viruses at Nanoscale Resolution", *Nano Letters*, v. 6, n. 7, pp. 1307–1310. doi: 10.1021/nl0610836. Disponível em: <https://doi.org/10.1021/nl0610836>. PMID: 16834401.

CARVALHO, D. L., DE AVILLEZ, R. R., RODRIGUES, M. T., et al., 2012, "Mg and Al mixed oxides and the synthesis of n-butanol from ethanol", *Applied Catalysis A: General*, v. 415-416, pp. 96–100. ISSN: 0926-860X. doi: https://doi.org/10.1016/j.apcata.2011.12.009. Disponível em: <https://www.sciencedirect.com/science/article/pii/S0926860X11007137>.

CARVALHO, D. L., BORGES, L. E., APPEL, L. G., et al., 2013, "In situ infrared spectroscopic study of the reaction pathway of the direct synthesis of n-butanol from ethanol over MgAl mixed-oxide catalysts", *Catalysis Today*, v. 213, pp. 115–121. ISSN: 0920-5861. doi: https://doi.org/10.1016/j.cattod.2013.03.034. Disponível em: <https://www.sciencedirect.com/science/article/

pii/S0920586113001478>. Selected contributions of the XXIII Iberoamerican Congress on Catalysis.

CAVANI, F., TRIFIRÒ, F., VACCARI, A., 1991, "Hydrotalcite-type anionic clays: Preparation, properties and applications." *Catalysis Today*, v. 11, n. 2, pp. 173–301. ISSN: 0920-5861. doi: https://doi.org/10.1016/0920-5861(91)80068-K. Disponível em: <https://www.sciencedirect.com/science/article/pii/092058619180068K>.

CHATTOT, R., BORDET, P., MARTENS, I., et al., 2020, "Building Practical Descriptors for Defect Engineering of Electrocatalytic Materials", *ACS Catalysis*, v. 10, n. 16, pp. 9046–9056. doi: 10.1021/acscatal.0c02144. Disponível em: <https://doi.org/10.1021/acscatal.0c02144>.

CHIEREGATO, A., VELASQUEZ OCHOA, J., BANDINELLI, C., et al., 2015, "On the Chemistry of Ethanol on Basic Oxides: Revising Mechanisms and Intermediates in the Lebedev and Guerbet reactions", *ChemSusChem*, v. 8, n. 2, pp. 377–388. doi: https://doi.org/10.1002/cssc.201402632. Disponível em: <https://chemistry-europe.onlinelibrary.wiley.com/doi/abs/10.1002/cssc.201402632>.

CHIZALLET, C., COSTENTIN, G., CHE, M., et al., 2007, "Infrared Characterization of Hydroxyl Groups on MgO: A Periodic and Cluster Density Functional Theory Study", *Journal of the American Chemical Society*, v. 129, n. 20, pp. 6442–6452. doi: 10.1021/ja068720e. Disponível em: <https://doi.org/10.1021/ja068720e>. PMID: 17465545.

CHIZALLET, C., COSTENTIN, G., CHE, M., et al., 2006, "Revisiting Acido-basicity of the MgO Surface by Periodic Density Functional Theory Calculations: Role of Surface Topology and Ion Coordination on Water Dissociation", *The Journal of Physical Chemistry B*, v. 110, n. 32, pp. 15878–15886. doi: 10.1021/jp060840l. Disponível em: <https://doi.org/10.1021/jp0608401>. PMID: 16898740.

CHOI, H., HAN, J., LEE, J., 2021, "Renewable Butanol Production via Catalytic Routes", *International Journal of Environmental Research and Public Health*, v. 18, n. 22. ISSN: 1660-4601. doi: 10.3390/ijerph182211749. Disponível em: <https://www.mdpi.com/1660-4601/18/22/11749>.

CIOLA, R., 1981, *Fundamentos da catálise*. São Paulo, Ed. da USP.

COLUCCIA, S., LAVAGNINO, S., MARCHESE, L., 1988, "The hydroxylated surface of MgO powders and the formation of surface sites",

Materials Chemistry and Physics, v. 18, n. 5, pp. 445–464. ISSN: 0254-0584. doi: https://doi.org/10.1016/0254-0584(88)90016-8. Disponível em: <https://www.sciencedirect.com/science/article/pii/0254058488900168>.

COLUCCIA, S., MARCHESE, L., LAVAGNINO, S., et al., 1987, "Hydroxyls on the surface of MgO powders", *Spectrochimica Acta Part A: Molecular Spectroscopy*, v. 43, n. 12, pp. 1573–1576. ISSN: 0584-8539. doi: https://doi.org/10.1016/S0584-8539(87)80050-8. Disponível em: <https://www.sciencedirect.com/science/article/pii/S0584853987800508>.

DAGLE, V. L., WINKELMAN, A. D., JAEGERS, N. R., et al., 2020, "Single-Step Conversion of Ethanol to n-Butene over Ag-ZrO2/SiO2 Catalysts", *ACS Catalysis*, v. 10, n. 18, pp. 10602–10613. doi: 10.1021/acscatal.0c02235. Disponível em: <https://doi.org/10.1021/acscatal.0c02235>.

DAVYDOV, A., 2003a, *Molecular Spectroscopy of Oxide Catalyst Surfaces*. Chichester, UK, John Wiley & Sons, Ltd. ISBN: 9780471987314. doi: 10.1002/0470867981. Disponível em: <https://doi.org/10.1002/0470867981>. First published: 17 April 2003.

DAVYDOV, A., 2003b, "The Nature of Oxide Surface Centers". In: *Molecular Spectroscopy of Oxide Catalyst Surfaces*, cap. 2, pp. 27–179, Unknown Address, John Wiley & Sons, Ltd, b. ISBN: 9780470867983. doi: https://doi.org/10.1002/0470867981.ch2. Disponível em: <https://onlinelibrary.wiley.com/doi/abs/10.1002/0470867981.ch2>.

DE SOUZA, E. F., PACHECO, H. P., MIYAKE, N., et al., 2020, "Computational and Experimental Mechanistic Insights into the Ethanol-to-Butanol Upgrading Reaction over MgO", *ACS Catalysis*, v. 10, n. 24, pp. 15162–15177. doi: 10.1021/acscatal.0c04616. Disponível em: <https://doi.org/10.1021/acscatal.0c04616>.

DI COSIMO, J., DIEZ, V., XU, M., et al., 1998, "Structure and Surface and Catalytic Properties of Mg-Al Basic Oxides", *Journal of Catalysis*, v. 178, n. 2, pp. 499–510. ISSN: 0021-9517. doi: https://doi.org/10.1006/jcat.1998.2161. Disponível em: <https://www.sciencedirect.com/science/article/pii/S0021951798921613>.

DI COSIMO, J., APESTEGU&ÍA, C., GIEES, M., et al., 2000, "Structural Requirements and Reaction Pathways in Condensation Reactions of Alcohols on MgyAlOx Catalysts", *Journal of Catalysis*, v. 190, n. 2,

pp. 261–275. ISSN: 0021-9517. doi: https://doi.org/10.1006/jcat.1999.2734. Disponível em: <https://www.sciencedirect.com/science/article/pii/S0021951799927343>.

DIETZ, W. A., 1967, "Response Factors for Gas Chromatographic Analyses", *Journal of Chromatographic Science*, v. 5, n. 2 (02), pp. 68–71. ISSN: 0021-9665. doi: 10.1093/chromsci/5.2.68. Disponível em: <https://doi.org/10.1093/chromsci/5.2.68>.

DÍEZ, V., FERRETTI, C., TORRESI, P., et al., 2011, "Effect of MgO activation conditions on its catalytic properties for base-catalyzed reactions", *Catalysis Today*, v. 173, n. 1, pp. 21–27. ISSN: 0920-5861. doi: https://doi.org/10.1016/j.cattod.2011.02.060. Disponível em: <https://www.sciencedirect.com/science/article/pii/S0920586111002264>. CAFC9, 9th Congress on Catalysis Applied to Fine Chemicals (Zaragoza, Spain, September 13th -16th 2010).

EAGAN, N. M., KUMBHALKAR, M. D., BUCHANAN, J. S., et al., 2019, "Chemistries and processes for the conversion of ethanol into middle-distillate fuels", *Nature Reviews Chemistry*, v. 3, pp. 223–249. doi: 10.1038/s41570-019-0084-4. Disponível em: <https://doi.org/10.1038/s41570-019-0084-4>.

EPE, 2021. "Cenários de oferta de etanol e demanda Ciclo Otto 2022 – 2035". Disponível em: <www.epe.gov.br>.

FENG, S.-H., LI, G.-H., 2017, "Chapter 4 - Hydrothermal and Solvothermal Syntheses". In: Xu, R., Xu, Y. (Eds.), *Modern Inorganic Synthetic Chemistry (Second Edition)*, second edition ed., Elsevier, pp. 73–104, Amsterdam. ISBN: 978-0-444-63591-4. doi: https://doi.org/10.1016/B978-0-444-63591-4.00004-5. Disponível em: <https://www.sciencedirect.com/science/article/pii/B9780444635914000045>.

FREITAS, R. O., MAIA, F. C. B., DENEKE, C., et al., 2017, "Infrared Nanospectroscopy at the LNLS: Current Status and Ongoing Developments", *Synchrotron Radiation News*, v. 30, n. 4, pp. 24–30. doi: 10.1080/08940886.2017.1338420. Disponível em: <https://doi.org/10.1080/08940886.2017.1338420>.

GABRIËLS, D., HERNÁNDEZ, W. Y., SELS, B., et al., 2015, "Review of catalytic systems and thermodynamics for the Guerbet condensation reaction and

challenges for biomass valorization", *Catal. Sci. Technol.*, v. 5, pp. 3876–3902. doi: 10.1039/C5CY00359H. Disponível em: <http://dx.doi.org/10.1039/C5CY00359H>.

GALWEY, A. K., MORTIMER, M., 2006, "Compensation effects and compensation defects in kinetic and mechanistic interpretations of heterogeneous chemical reactions", *International Journal of Chemical Kinetics*, v. 38, n. 7, pp. 464–473. doi: https://doi.org/10.1002/kin.20176. Disponível em: <https://onlinelibrary.wiley.com/doi/abs/10.1002/kin.20176>.

GINES, M. J., IGLESIA, E., 1998, "Bifunctional Condensation Reactions of Alcohols on Basic Oxides Modified by Copper and Potassium", *Journal of Catalysis*, v. 176, n. 1, pp. 155–172. ISSN: 0021-9517. doi: https://doi.org/10.1006/jcat.1998.2009. Disponível em: <https://www.sciencedirect.com/science/article/pii/S0021951798920097>.

GUERBET, M., 1909, "Condensation de l'alcool isopropylique avec son dérivé sodé; formation du méthylisobutylcarbinol et du diméthyl-2.4-heptanol-6", *CR Acad. Sci. Paris*, v. 149, pp. 129–132.

GUNST, D., ALEXOPOULOS, K., VAN DER BORGHT, K., et al., 2017, "Study of butanol conversion to butenes over H-ZSM-5: Effect of chemical structure on activity, selectivity and reaction pathways", *Applied Catalysis A: General*, v. 539, pp. 1–12. ISSN: 0926-860X. doi: https://doi.org/10.1016/j.apcata.2017.03.036. Disponível em: <https://www.sciencedirect.com/science/article/pii/S0926860X1730145X>.

GURULE, A. C., GAIKWAD, S. S., KAJALE, D. D., et al., 2025, "Synthesis of magnesium oxide nanoparticles via hydrothermal and sol-gel methods: Charaterization and their application for H2S and NO2 gas sensing", *Journal of the Indian Chemical Society*, v. 102, n. 1, pp. 101496. ISSN: 0019-4522. doi: https://doi.org/10.1016/j.jics.2024.101496. Disponível em: <https://www.sciencedirect.com/science/article/pii/S0019452224003765>.

HADIA, N., MOHAMED, H. A.-H., 2015, "Characteristics and optical properties of MgO nanowires synthesized by solvothermal method", *Materials Science in Semiconductor Processing*, v. 29, pp. 238–244. ISSN: 1369-8001. doi: https://doi.org/10.1016/j.mssp.2014.03.049. Disponível em: <https://www.sciencedirect.com/science/article/

pii/S1369800114001905>. Special Topical Issue on Wide-Bandgap Semiconductor Materials.

HANSPAL, S., YOUNG, Z. D., SHOU, H., et al., 2015, "Multiproduct Steady-State Isotopic Transient Kinetic Analysis of the Ethanol Coupling Reaction over Hydroxyapatite and Magnesia", *ACS Catalysis*, v. 5, n. 3, pp. 1737–1746. doi: 10.1021/cs502023g. Disponível em: <https://doi.org/10.1021/cs502023g>.

HANSPAL, S., YOUNG, Z. D., PRILLAMAN, J. T., et al., 2017, "Influence of surface acid and base sites on the Guerbet coupling of ethanol to butanol over metal phosphate catalysts", *Journal of Catalysis*, v. 352, pp. 182–190. ISSN: 0021-9517. doi: https://doi.org/10.1016/j.jcat.2017.04.036. Disponível em: <https://www.sciencedirect.com/science/article/pii/S0021951717301574>.

HAVA, S., IVRI, J., AUSLENDER, M., 2001, "Wavenumber-modulated patterns of transmission through one- and two-dimensional gratings on a silicon substrate", *Journal of Optics A: Pure and Applied Optics*, v. 3, n. 6 (oct), pp. S190. doi: 10.1088/1464-4258/3/6/370. Disponível em: <https://dx.doi.org/10.1088/1464-4258/3/6/370>.

HERMANN, P., HOEHL, A., ULRICH, G., et al., 2014, "Characterization of semiconductor materials using synchrotron radiation-based near-field infrared microscopy and nano-FTIR spectroscopy", *Optics express*, v. 22, n. 15, pp. 17948–17958.

HO, C. R., SHYLESH, S., BELL, A. T., 2016, "Mechanism and Kinetics of Ethanol Coupling to Butanol over Hydroxyapatite", *ACS Catalysis*, v. 6, n. 2, pp. 939–948. doi: 10.1021/acscatal.5b02672. Disponível em: <https://doi.org/10.1021/acscatal.5b02672>.

HORNAK, J., 2021, "Synthesis, Properties, and Selected Technical Applications of Magnesium Oxide Nanoparticles: A Review", *International Journal of Molecular Sciences*, v. 22, n. 23. ISSN: 1422-0067. doi: 10.3390/ijms222312752. Disponível em: <https://www.mdpi.com/1422-0067/22/23/12752>.

HUTH, F., GOVYADINOV, A., AMARIE, S., et al., 2012, "Nano-FTIR Absorption Spectroscopy of Molecular Fingerprints at 20 nm Spatial Resolution", *Nano Letters*, v. 12, n. 8, pp. 3973–3978. doi: 10.1021/nl301159v. Disponível em: <https://doi.org/10.1021/nl301159v>. PMID: 22703339.

I. CHORKENDORFF, N. J. W., 2017a, "Kinetics". In: *Concepts of Modern Catalysis and Kinetics*, cap. 2, pp. 23–78, Germany, John Wiley & Sons, Ltd, a. ISBN: 9783527602650. doi: https://doi.org/10.1002/3527602658.ch2. Disponível em: <https://onlinelibrary.wiley.com/doi/abs/10.1002/3527602658.ch2>.

I. CHORKENDORFF, N. J. W., 2017b, "Solid Catalysts". In: *Concepts of Modern Catalysis and Kinetics*, cap. 5, pp. 167–214, Germany, John Wiley & Sons, Ltd, b. ISBN: 9783527602650. doi: https://doi.org/10.1002/3527602658.ch5. Disponível em: <https://onlinelibrary.wiley.com/doi/abs/10.1002/3527602658.ch5>.

IONASHIRO, M., CAIRES, F. J., GOMES, D. J. C., 2014, *Giolito: Fundamentos da Termogravimetria e Análise Térmica Diferencial / Calorimetria Exploratória Diferencial*. 2 ed. São Paulo, Giz Editorial. ISBN: 978-85-7855-222-0.

IVANOV, V., BACHELIER, J., AUDRY, F., et al., 1994, "Study of the Meerwein—Pondorff—Verley reaction between ethanol and acetone on various metal oxides", *Journal of Molecular Catalysis*, v. 91, n. 1, pp. 45–59. ISSN: 0304-5102. doi: https://doi.org/10.1016/0304-5102(94)00017-4. Disponível em: <https://www.sciencedirect.com/science/article/pii/0304510294000174>.

JABŁOŃSKA, M., NOTHDURFT, K., NOCUŃ, M., et al., 2017, "Redox-performance correlations in Ag–Cu–Mg–Al, Ce–Cu–Mg–Al, and Ga–Cu–Mg–Al hydrotalcite derived mixed metal oxides", *Applied Catalysis B: Environmental*, v. 207, pp. 385–396. ISSN: 0926-3373. doi: https://doi.org/10.1016/j.apcatb.2017.01.079. Disponível em: <https://www.sciencedirect.com/science/article/pii/S0926337317300966>.

KADAM, S. A., SHAMZHY, M. V., 2018, "IR Operando study of ethanol dehydration over MFI zeolite", *Catalysis Today*, v. 304, pp. 51–57. ISSN: 0920-5861. doi: https://doi.org/10.1016/j.cattod.2017.09.020. Disponível em: <https://www.sciencedirect.com/science/article/pii/S0920586117306272>. 7th Czech-Italian-Spanish Symposium on Zeolites and Catalysis.

KAFLE, B. P., 2020, "Chapter 6 - Introduction to nanomaterials and application of UV–Visible spectroscopy for their characterization". In: Kafle, B. P. (Ed.), *Chemical Analysis and Material Characterization by Spectrophotometry*,

Elsevier, pp. 147–198. ISBN: 978-0-12-814866-2. doi: https://doi.org/10.1016/B978-0-12-814866-2.00006-3. Disponível em: <https://www.sciencedirect.com/science/article/pii/B9780128148662000063>.

KAMIENIAK, J., BERNALTE, E., FOSTER, C. W., et al., 2016, "High Yield Synthesis of Hydroxyapatite (HAP) and Palladium Doped HAP via a Wet Chemical Synthetic Route", *Catalysts*, v. 6, n. 8. ISSN: 2073-4344. doi: 10.3390/catal6080119. Disponível em: <https://www.mdpi.com/2073-4344/6/8/119>.

KHORSAND ZAK, A., ABD. MAJID, W., ABRISHAMI, M., et al., 2011, "X-ray analysis of ZnO nanoparticles by Williamson–Hall and size–strain plot methods", *Solid State Sciences*, v. 13, n. 1, pp. 251–256. ISSN: 1293-2558. doi: https://doi.org/10.1016/j.solidstatesciences.2010.11.024. Disponível em: <https://www.sciencedirect.com/science/article/pii/S1293255810004607>.

KLABUNDE, K. J., STARK, J., KOPER, O., et al., 1996, "Nanocrystals as Stoichiometric Reagents with Unique Surface Chemistry", *The Journal of Physical Chemistry*, v. 100, n. 30, pp. 12142–12153. doi: 10.1021/jp960224x. Disponível em: <https://doi.org/10.1021/jp960224x>.

KNÖZINGER, E., JACOB, K.-H., SINGH, S., et al., 1993, "Hydroxyl groups as IR active surface probes on MgO crystallites", *Surface Science*, v. 290, n. 3, pp. 388–402. ISSN: 0039-6028. doi: https://doi.org/10.1016/0039-6028(93)90721-U. Disponível em: <https://www.sciencedirect.com/science/article/pii/003960289390721U>.

KOLESINSKA, B., FRACZYK, J., BINCZARSKI, M., et al., 2019, "Butanol Synthesis Routes for Biofuel Production: Trends and Perspectives", *Materials*, v. 12, n. 3. ISSN: 1996-1944. doi: 10.3390/ma12030350. Disponível em: <https://www.mdpi.com/1996-1944/12/3/350>.

KOZLOWSKI, J. T., DAVIS, R. J., 2013, "Heterogeneous Catalysts for the Guerbet Coupling of Alcohols", *ACS Catalysis*, v. 3, n. 7, pp. 1588–1600. doi: 10.1021/cs400292f. Disponível em: <https://doi.org/10.1021/cs400292f>.

KRUTOKHVOSTOV, R., GOVYADINOV, A. A., STIEGLER, J. M., et al., 2012, "Enhanced resolution in subsurface near-field optical microscopy", *Opt. Express*, v. 20, n. 1 (Jan), pp. 593–600. doi: 10.1364/OE.20.000593. Disponível em: <https://opg.optica.org/oe/abstract.cfm?URI=oe-20-1-593>.

LEE, J. H., JEON, H., PARK, J. T., et al., 2020, "Synthesis of hierarchical flower-shaped hollow MgO microspheres via ethylene-glycol-mediated process as a base heterogeneous catalyst for transesterification for biodiesel production", *Biomass and Bioenergy*, v. 142, pp. 105788. ISSN: 0961-9534. doi: https://doi.org/10.1016/j.biombioe.2020.105788. Disponível em: <https://www.sciencedirect.com/science/article/pii/S0961953420303238>.

LEÓN, M., DÍAZ, E., ORDÓÑEZ, S., 2011, "Ethanol catalytic condensation over Mg–Al mixed oxides derived from hydrotalcites", *Catalysis Today*, v. 164, n. 1, pp. 436–442. ISSN: 0920-5861. doi: https://doi.org/10.1016/j.cattod.2010.10.003. Disponível em: <https://www.sciencedirect.com/science/article/pii/S0920586110005912>. Innovations driven by catalysis - Selected papers from TOCAT6 / APCAT5.

LI, J., LIANG, J., LAN, M.-H., et al., 2023, "Atomic Force Microscopy-Based Nanoscale Infrared Techniques for Catalysis", *The Journal of Physical Chemistry Letters*, v. 14, n. 50, pp. 11318–11323. doi: 10.1021/acs.jpclett.3c02937. Disponível em: <https://doi.org/10.1021/acs.jpclett.3c02937>. PMID: 38064367.

LIN, F., DAGLE, V. L., WINKELMAN, A. D., et al., 2021, "Understanding the Deactivation of Ag-ZrO2/SiO2 Catalysts for the Single-step Conversion of Ethanol to Butenes", *ChemCatChem*, v. 13, n. 3, pp. 999–1008. doi: https://doi.org/10.1002/cctc.202001488. Disponível em: <https://chemistry-europe.onlinelibrary.wiley.com/doi/abs/10.1002/cctc.202001488>.

LUO, Y., WU, Y., 2023, "Defect Engineering of Nanomaterials for Catalysis", *Nanomaterials*, v. 13, n. 6. ISSN: 2079-4991. doi: 10.3390/nano13061116. Disponível em: <https://www.mdpi.com/2079-4991/13/6/1116>.

MAO, Z., CAMPBELL, C. T., 2019, "Apparent Activation Energies in Complex Reaction Mechanisms: A Simple Relationship via Degrees of Rate Control", *ACS Catalysis*, v. 9, n. 10, pp. 9465–9473. doi: 10.1021/acscatal.9b02761. Disponível em: <https://doi.org/10.1021/acscatal.9b02761>.

MARCU, I.-C., TANCHOUX, N., FAJULA, F., et al., 2013, "Catalytic conversion of ethanol into butanol over M–Mg–Al mixed oxide catalysts (M= Pd, Ag, Mn, Fe, Cu, Sm, Yb) obtained from LDH precursors", *Catalysis letters*, v. 143, pp. 23–30.

MARTINS, L. P., JR., C. L. C., 2024, *Catalisadores heterogêneos porosos: definições, propriedades, caracterizações, sínteses e aplicações*. Geral. 1 ed. Curitiba, Appris. ISBN: 978-65-250-6778-0.

MCKENZIE, A. L., FISHEL, C. T., DAVIS, R. J., 1992, "Investigation of the surface structure and basic properties of calcined hydrotalcites", *Journal of Catalysis*, v. 138, n. 2, pp. 547–561. ISSN: 0021-9517. doi: https://doi.org/10.1016/0021-9517(92)90306-3. Disponível em: <https://www.sciencedirect.com/science/article/pii/0021951792903063>.

MESTER, L., GOVYADINOV, A. A., CHEN, S., et al., 2020, "Subsurface chemical nanoidentification by nano-FTIR spectroscopy", *Nature communications*, v. 11, n. 1, pp. 3359.

MICHALAK, W. D., KRIER, J. M., KOMVOPOULOS, K., et al., 2013, "Structure Sensitivity in Pt Nanoparticle Catalysts for Hydrogenation of 1,3-Butadiene: In Situ Study of Reaction Intermediates Using SFG Vibrational Spectroscopy", *The Journal of Physical Chemistry C*, v. 117, n. 4, pp. 1809–1817. doi: 10.1021/jp311772p. Disponível em: <https://doi.org/10.1021/jp311772p>.

MORROW, B. A., 1990, "Surface groups on oxides". In: *Studies in Surface Science and Catalysis*, v. 57, Elsevier, pp. 161–222.

MÜCK, J., KOCÍK, J., HÁJEK, M., et al., 2021, "Transition metals promoting Mg-Al mixed oxides for conversion of ethanol to butanol and other valuable products: Reaction pathways", *Applied Catalysis A: General*, v. 626, pp. 118380. ISSN: 0926-860X. doi: https://doi.org/10.1016/j.apcata.2021.118380. Disponível em: <https://www.sciencedirect.com/science/article/pii/S0926860X2100394X>.

NDOU, A., COVILLE, N., 2004, "Self-condensation of propanol over solid-base catalysts", *Applied Catalysis A: General*, v. 275, n. 1, pp. 103–110. ISSN: 0926-860X. doi: https://doi.org/10.1016/j.apcata.2004.07.025. Disponível em: <https://www.sciencedirect.com/science/article/pii/S0926860X04006672>.

NDOU, A., PLINT, N., COVILLE, N., 2003, "Dimerisation of ethanol to butanol over solid-base catalysts", *Applied Catalysis A: General*, v. 251, n. 2, pp. 337–345. ISSN: 0926-860X. doi: https://doi.org/10.1016/S0926-860X(03)00363-6. Disponível em: <https://www.sciencedirect.com/science/article/pii/S0926860X03003636>.

NØRSKOV, J. K., STUDT, F., ABILD-PEDERSEN, F., et al., 2014, "Kinetics". In: *Fundamental Concepts in Heterogeneous Catalysis*, cap. 5, pp. 68–84, United States of America, John Wiley & Sons, Ltd. ISBN: 9781118892114. doi: https://doi.org/10.1002/9781118892114.ch5. Disponível em: <https://onlinelibrary.wiley.com/doi/abs/10.1002/9781118892114.ch5>.

OSMAN, M. B., KRAFFT, J.-M., THOMAS, C., et al., 2019, "Importance of the Nature of the Active Acid/Base Pairs of Hydroxyapatite Involved in the Catalytic Transformation of Ethanol to n-Butanol Revealed by Operando DRIFTS", *ChemCatChem*, v. 11, n. 6, pp. 1765–1778. doi: https://doi.org/10.1002/cctc.201801880. Disponível em: <https://chemistry-europe.onlinelibrary.wiley.com/doi/abs/10.1002/cctc.201801880>.

PACHECO, H. P., DE SOUZA, E. F., LANDI, S. M., et al., 2019, "Ru Promoted MgO and Al-Modified MgO for Ethanol Upgrading", *Topics in Catalysis*, v. 62, n. 9–11 (September), pp. 894–907. doi: 10.1007/s11244-019-01177-y. Disponível em: <https://doi.org/10.1007/s11244-019-01177-y>.

PACHECO, H. P., 2019, *Investigation Of The Mechanism Of Ethanol Upgrading On Mgo-Based Catalysts*. Tese de Doutorado, UFRJ/COPPE, 2019.

PINHEIRO, C. H., BALDANZA, M. A. S., SMARZARO, J., et al., 2024a, "Fischer–Tropsch Synthesis Model Involving the Living Growth of Carbon Chains", *Industrial & Engineering Chemistry Research*, v. 63, n. 7, pp. 2980–2990. doi: 10.1021/acs.iecr.3c03898. Disponível em: <https://doi.org/10.1021/acs.iecr.3c03898>.

PINHEIRO, M. G. S., DE SOUZA, E. F., CHAGAS, L. H., et al., 2024b, "The role of oxygen vacancies and Zn in isobutene synthesis from ethanol employing Zn, Zr-based catalysts", *Catal. Sci. Technol.*, v. 14, pp. 2794–2805. doi: 10.1039/D4CY00230J. Disponível em: <http://dx.doi.org/10.1039/D4CY00230J>.

PINTO, J. C., SCHWAAB, M., 2007, *Análise de Dados Experimentais: I. Fundamentos de Estatística e Estimação de Parâmetros*. Rio de Janeiro, Editora E-papers.

POLLARD, B., MULLER, E. A., HINRICHS, K., et al., 2014, "Vibrational nano-spectroscopic imaging correlating structure with intermolecular coupling and dynamics", *Nature Communications*, v. 5, n. 1, pp. 3587.

QUATTLEBAUM, W. M., TOUSSAINT, W. J., DUNN, J. T., 1947, "Deoxygenation of Certain Aldehydes and Ketones: Preparation of Butadiene and Styrene1", *Journal of the American Chemical Society*, v. 69, n. 3, pp. 593–599. doi: 10.1021/ja01195a040. Disponível em: <https://doi.org/10.1021/ja01195a040>.

RABENAU, A., 1985, "The Role of Hydrothermal Synthesis in Preparative Chemistry", *Angewandte Chemie International Edition in English*, v. 24, n. 12, pp. 1026–1040. doi: https://doi.org/10.1002/anie.198510261. Disponível em: <https://onlinelibrary.wiley.com/doi/abs/10.1002/anie.198510261>.

RAMGIR, N. S., HWANG, Y. K., MULLA, I. S., et al., 2006, "Effect of particle size and strain in nanocrystalline SnO2 according to doping concentration of ruthenium", *Solid State Sciences*, v. 8, n. 3, pp. 359–362. ISSN: 1293-2558. doi: https://doi.org/10.1016/j.solidstatesciences.2006.02.008. Disponível em: <https://www.sciencedirect.com/science/article/pii/S1293255806000276>. Special issue in honour of A.K.Cheetham.

RECHI SIQUEIRA, M., MICALI PERRONE, O., METZKER, G., et al., 2019, "Highly selective 1-butanol obtained from ethanol catalyzed by mixed metal oxides: Reaction optimization and catalyst structure behavior", *Molecular Catalysis*, v. 476, pp. 110516. ISSN: 2468-8231. doi: https://doi.org/10.1016/j.mcat.2019.110516. Disponível em: <https://www.sciencedirect.com/science/article/pii/S246882311930358X>.

RICHARDS, D., ZAYATS, A., KEILMANN, F., et al., 2004, "Near-field microscopy by elastic light scattering from a tip", *Philosophical Transactions of the Royal Society of London. Series A: Mathematical, Physical and Engineering Sciences*, v. 362, n. 1817, pp. 787–805. doi: 10.1098/rsta.2003.1347. Disponível em: <https://royalsocietypublishing.org/doi/abs/10.1098/rsta.2003.1347>.

ROGERS, K., DANIELS, P., 2002, "An X-ray diffraction study of the effects of heat treatment on bone mineral microstructure", *Biomaterials*, v. 23, n. 12, pp. 2577–2585. ISSN: 0142-9612. doi: https://doi.org/10.1016/S0142-9612(01)00395-7. Disponível em: <https://www.sciencedirect.com/science/article/pii/S0142961201003957>.

ROY, B., PANDA, A. B., CHATTOPADHYAY, A. P., 2017, "Controlled Synthesis of Different Morphologies of Cu–MgO and Their Application as Catalysts in Synthesis of 1,2,3-Triazoles Following Different Pathways",

ChemistrySelect, v. 2, n. 24, pp. 7340–7352. doi: https://doi.org/10.1002/slct.201701517. Disponível em: <https://chemistry-europe.onlinelibrary.wiley.com/doi/abs/10.1002/slct.201701517>.

SANTOS, M. L., PACHECO, H. P., TONIOLO, F. S., 2025, "Tuning acid and basic features on MgxAlOy-SiO2 impacted ethanol upgrading to 1,3-butadiene", *Catalysis Today*, v. 444, pp. 115017. ISSN: 0920-5861. doi: https://doi.org/10.1016/j.cattod.2024.115017. Disponível em: <https://www.sciencedirect.com/science/article/pii/S092058612400511X>.

SAY, Z., KAYA, M., KADEROĞLU, Ç., et al., 2022, "Unraveling Molecular Fingerprints of Catalytic Sulfur Poisoning at the Nanometer Scale with Near-Field Infrared Spectroscopy", *Journal of the American Chemical Society*, v. 144, n. 19, pp. 8848–8860. doi: 10.1021/jacs.2c03088. Disponível em: <https://doi.org/10.1021/jacs.2c03088>. PMID: 35486918.

SCALBERT, J., THIBAULT-STARZYK, F., JACQUOT, R., et al., 2014, "Ethanol condensation to butanol at high temperatures over a basic heterogeneous catalyst: How relevant is acetaldehyde self-aldolization?" *Journal of Catalysis*, v. 311, pp. 28–32. ISSN: 0021-9517. doi: https://doi.org/10.1016/j.jcat.2013.11.004. Disponível em: <https://www.sciencedirect.com/science/article/pii/S0021951713003813>.

SCHEID, A. J., BARBOSA-COUTINHO, E., SCHWAAB, M., et al., 2019, "Mechanism and Kinetic Modeling of Ethanol Conversion to 1-Butanol over Mg and Al Oxide Derived from Hydrotalcites", *Industrial & Engineering Chemistry Research*, v. 58, n. 29, pp. 12981–12995. doi: 10.1021/acs.iecr.9b01491. Disponível em: <https://doi.org/10.1021/acs.iecr.9b01491>.

SCHERRER, P., 1918, "Bestimmung der Größe und der inneren Struktur von Kolloidteilchen mittels Röntgenstrahlen", *Nachrichten von der Gesellschaft der Wissenschaften zu Göttingen, Math. Klasse*, pp. 98–100.

SCHLÖGL, R., 2009, "Chapter 5 X-ray Diffraction: A Basic Tool for Characterization of Solid Catalysts in the Working State". In: *Advances in Catalysis*, v. 52, *Advances in Catalysis*, Academic Press, pp. 273–338. doi: https://doi.org/10.1016/S0360-0564(08)00005-9. Disponível em: <https://www.sciencedirect.com/science/article/pii/S0360056408000059>.

SCHWAAB, M., BISCAIA, JR., E. C., MONTEIRO, J. L., et al., 2008, "Nonlinear parameter estimation through particle swarm optimization", *Chemical Engineering Science*, v. 63, n. 6, pp. 1542–1552. ISSN: 0009-2509. doi: https://doi.org/10.1016/j.ces.2007.11.024. Disponível em: <https://www.sciencedirect.com/science/article/pii/S0009250907008755>.

SELVAMANI, T., SINHAMAHAPATRA, A., BHATTACHARJYA, D., et al., 2011, "Rectangular MgO microsheets with strong catalytic activity", *Materials Chemistry and Physics*, v. 129, n. 3, pp. 853–861. ISSN: 0254-0584. doi: https://doi.org/10.1016/j.matchemphys.2011.05.055. Disponível em: <https://www.sciencedirect.com/science/article/pii/S0254058411004615>.

SHARMA, A., KUMARI, S., SHARMA, S., et al., 2023, "Layered double hydroxides: an insight into the role of hydrotalcite-type anionic clays in energy and environmental applications with current progress and recent prospects", *Materials Today Sustainability*, v. 22, pp. 100399. ISSN: 2589-2347. doi: https://doi.org/10.1016/j.mtsust.2023.100399. Disponível em: <https://www.sciencedirect.com/science/article/pii/S2589234723000854>.

SHIDO, T., ASAKURA, K., IWASAWA, Y., 1989, "The hydrogen exchange reaction of surface deuteroxyl groups on MgO with H2", *J. Chem. Soc., Faraday Trans. 1*, v. 85, pp. 441–453. doi: 10.1039/F19898500441. Disponível em: <http://dx.doi.org/10.1039/F19898500441>.

SILVERSTEIN, R. M., WEBSTER, F. X., KIEMLE, D. J., 2010, *Identificação espectrométrica de compostos orgánicos (7a.* Rio de Janeiro, Grupo Gen-LTC.

SING, K. S., 1985, "Reporting physisorption data for gas/solid systems with special reference to the determination of surface area and porosity (Recommendations 1984)", *Pure and applied chemistry*, v. 57, n. 4, pp. 603–619.

STIEGLER, J. M., ABATE, Y., CVITKOVIC, A., et al., 2011, "Nanoscale Infrared Absorption Spectroscopy of Individual Nanoparticles Enabled by Scattering-Type Near-Field Microscopy", *ACS Nano*, v. 5, n. 8, pp. 6494–6499. doi: 10.1021/nn2017638. Disponível em: <https://doi.org/10.1021/nn2017638>. PMID: 21770439.

SUTRADHAR, N., SINHAMAHAPATRA, A., ROY, B., et al., 2011, "Preparation of MgO nano-rods with strong catalytic activity via hydrated basic magnesium carbonates", *Materials Research Bulletin*, v. 46, n. 11, pp. 2163–2167. ISSN: 0025-5408. doi: https://doi.org/10.1016/j.materresbull.2011.02.024. Disponível em: <https://www.sciencedirect.com/science/article/pii/S0025540811000754>.

SZOSTAK, R., SILVA, J. C., TURREN-CRUZ, S.-H., et al., 2019, "Nanoscale mapping of chemical composition in organic-inorganic hybrid perovskite films", *Science Advances*, v. 5, n. 10, pp. eaaw6619. doi: 10.1126/sciadv.aaw6619. Disponível em: <https://www.science.org/doi/abs/10.1126/sciadv.aaw6619>.

TAIFAN, W. E., BUČKO, T., BALTRUSAITIS, J., 2017a, "Catalytic conversion of ethanol to 1,3-butadiene on MgO: A comprehensive mechanism elucidation using DFT calculations", *Journal of Catalysis*, v. 346, pp. 78–91. ISSN: 0021-9517. doi: https://doi.org/10.1016/j.jcat.2016.11.042. Disponível em: <https://www.sciencedirect.com/science/article/pii/S0021951716303062>.

TAIFAN, W. E., YAN, G. X., BALTRUSAITIS, J., 2017b, "Surface chemistry of MgO/SiO2 catalyst during the ethanol catalytic conversion to 1,3-butadiene: in-situ DRIFTS and DFT study", *Catal. Sci. Technol.*, v. 7, pp. 4648–4668. doi: 10.1039/C7CY01556A. Disponível em: <http://dx.doi.org/10.1039/C7CY01556A>.

TAN, L., WANG, F., ZHANG, P., et al., 2020, "Design of a core–shell catalyst: an effective strategy for suppressing side reactions in syngas for direct selective conversion to light olefins", *Chem. Sci.*, v. 11, pp. 4097–4105. doi: 10.1039/C9SC05544D. Disponível em: <http://dx.doi.org/10.1039/C9SC05544D>.

TAUBNER, T., HILLENBRAND, R., KEILMANN, F., 2004, "Nanoscale polymer recognition by spectral signature in scattering infrared near-field microscopy", *Applied Physics Letters*, v. 85, n. 21, pp. 5064–5066.

TSUCHIDA, T., SAKUMA, S., TAKEGUCHI, T., et al., 2006, "Direct Synthesis of n-Butanol from Ethanol over Nonstoichiometric Hydroxyapatite", *Industrial & Engineering Chemistry Research*, v. 45, n. 25, pp. 8634–8642. doi: 10.1021/ie0606082. Disponível em: <https://doi.org/10.1021/ie0606082>.

TSUCHIDA, T., KUBO, J., YOSHIOKA, T., et al., 2008, "Reaction of ethanol over hydroxyapatite affected by Ca/P ratio of catalyst", *Journal of Catalysis*, v. 259, n. 2, pp. 183–189. ISSN: 0021-9517. doi: https://doi.org/10.1016/j.jcat.2008.08.005. Disponível em: <https://www.sciencedirect.com/science/article/pii/S0021951708003102>.

TSYGANENKO, A., FILIMONOV, V., 1973, "Infrared spectra of surface hydroxyl groups and crystalline structure of oxides", *Journal of Molecular Structure*, v. 19, pp. 579–589. ISSN: 0022-2860. doi: https://doi.org/10.1016/0022-2860(73)85136-1. Disponível em: <https://www.sciencedirect.com/science/article/pii/0022286073851361>.

VAN SANTEN, R. A., NIEMANTSVERDRIET, J. W., 1995, *Chemical Kinetics and Catalysis*. Fundamental and Applied Catalysis. New York and London, Plenum Press.

VIKÁR, A., LÓNYI, F., MAKOYE, A., et al., 2023, "Ethanol Coupling Reactions over MgO–Al2O3 Mixed Oxide-Based Catalysts for Producing Biofuel Additives", *Molecules*, v. 28, n. 9, pp. 3788. doi: 10.3390/molecules28093788. Disponível em: <https://www.mdpi.com/1420-3049/28/9/3788>.

WANG, S.-C., CENDEJAS, M. C., HERMANS, I., 2020, "Insights into Ethanol Coupling over Hydroxyapatite using Modulation Excitation Operando Infrared Spectroscopy", *ChemCatChem*, v. 12, n. 16, pp. 4167–4175. doi: https://doi.org/10.1002/cctc.202000331. Disponível em: <https://chemistry-europe.onlinelibrary.wiley.com/doi/abs/10.1002/cctc.202000331>.

WU, C.-Y., WOLF, W. J., LEVARTOVSKY, Y., et al., 2017, "High-spatial-resolution mapping of catalytic reactions on single particles", *Nature*, v. 541, n. 7638, pp. 511–515.

WU, X., FANG, G., TONG, Y., et al., 2018, "Catalytic Upgrading of Ethanol to n-Butanol: Progress in Catalyst Development", *ChemSusChem*, v. 11, n. 1, pp. 71–85. doi: https://doi.org/10.1002/cssc.201701590. Disponível em: <https://chemistry-europe.onlinelibrary.wiley.com/doi/abs/10.1002/cssc.201701590>.

XU, M., IGLESIA, E., 1998, "Initial carbon–carbon bond formation during synthesis gas conversion to higher alcohols on K–Cu–Mg 5 CeO x catalysts", *Catalysis letters*, v. 51, pp. 47–52.

XU, X. G., RANG, M., CRAIG, I. M., et al., 2012, "Pushing the Sample-Size Limit of Infrared Vibrational Nanospectroscopy: From Monolayer toward Single Molecule Sensitivity", *The Journal of Physical Chemistry Letters*, v. 3, n. 13, pp. 1836–1841. doi: 10.1021/jz300463d. Disponível em: <https://doi.org/10.1021/jz300463d>. PMID: 26291869.

YAN, T., DAI, W., WU, G., et al., 2018, "Mechanistic Insights into One-Step Catalytic Conversion of Ethanol to Butadiene over Bifunctional Zn–Y/Beta Zeolite", *ACS Catalysis*, v. 8, n. 4, pp. 2760–2773. doi: 10.1021/acscatal.8b00014. Disponível em: <https://doi.org/10.1021/acscatal.8b00014>.

YANG, C., MENG, Z., 1993, "Bimolecular Condensation of Ethanol to 1-Butanol Catalyzed by Alkali Cation Zeolites", *Journal of Catalysis*, v. 142, n. 1, pp. 37–44. ISSN: 0021-9517. doi: https://doi.org/10.1006/jcat.1993.1187. Disponível em: <https://www.sciencedirect.com/science/article/pii/S0021951783711875>.

YANG, G., PARK, S.-J., 2019, "Conventional and Microwave Hydrothermal Synthesis and Application of Functional Materials: A Review", *Materials*, v. 12, n. 7. ISSN: 1996-1944. doi: 10.3390/ma12071177. Disponível em: <https://www.mdpi.com/1996-1944/12/7/1177>.

YOUNG, Z. D., DAVIS, R. J., 2018, "Hydrogen transfer reactions relevant to Guerbet coupling of alcohols over hydroxyapatite and magnesium oxide catalysts", *Catal. Sci. Technol.*, v. 8, pp. 1722–1729. doi: 10.1039/C7CY01393K. Disponível em: <http://dx.doi.org/10.1039/C7CY01393K>.

YOUNG, Z. D., HANSPAL, S., DAVIS, R. J., 2016, "Aldol Condensation of Acetaldehyde over Titania, Hydroxyapatite, and Magnesia", *ACS Catalysis*, v. 6, n. 5, pp. 3193–3202. doi: 10.1021/acscatal.6b00264. Disponível em: <https://doi.org/10.1021/acscatal.6b00264>.

YUK, S. F., LEE, M.-S., COLLINGE, G., et al., 2020, "Mechanistic Understanding of Catalytic Conversion of Ethanol to 1-Butene over 2D-Pillared MFI Zeolite", *The Journal of Physical Chemistry C*, v. 124, n. 52, pp. 28437–28447. doi: 10.1021/acs.jpcc.0c05585. Disponível em: <https://doi.org/10.1021/acs.jpcc.0c05585>.

ZHANG, J., WEGENER, E. C., SAMAD, N. R., et al., 2021, "Isolated Metal Sites in Cu–Zn–Y/Beta for Direct and Selective Butene-Rich C3+ Olefin

Formation from Ethanol", *ACS Catalysis*, v. 11, n. 15, pp. 9885–9897. doi: 10.1021/acscatal.1c02177. Disponível em: <https://doi.org/10.1021/acscatal.1c02177>.

Appendix A

Crystalline Phases

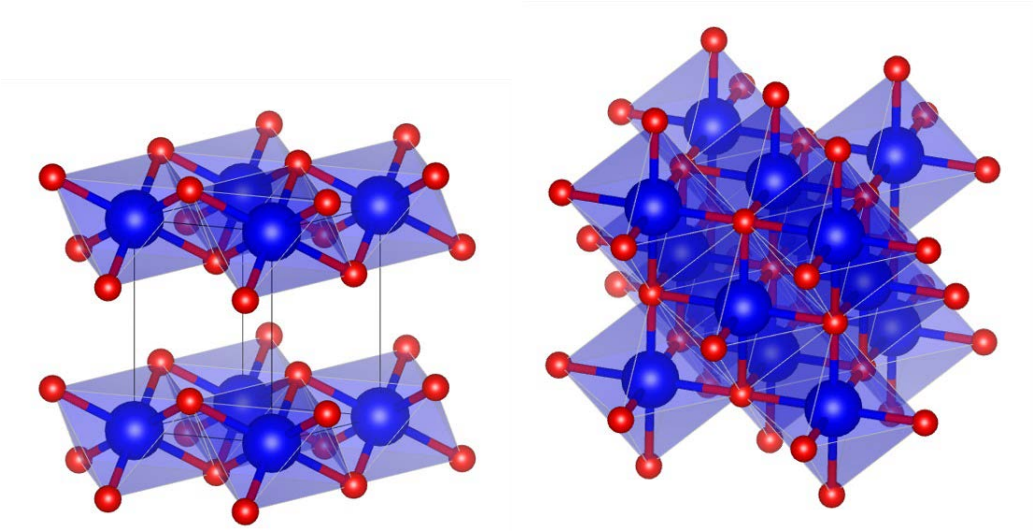

(a) Brucite (b) Periclase

Figure A.1: Illustration of crystal phases found for MgO-p, MgO-f, and MgO-w. Created using VESTA software

Appendix B

Product Yield

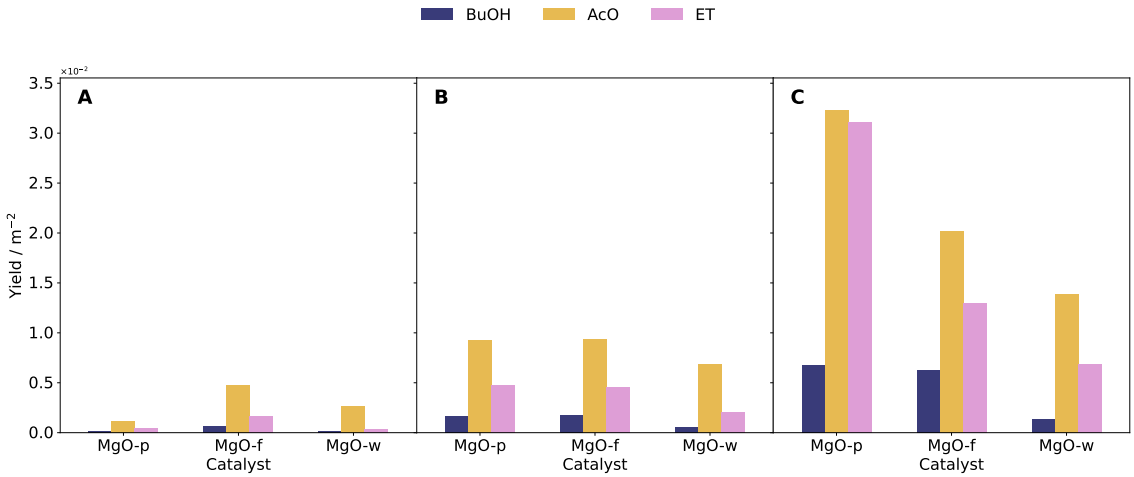

Figure B.1: Catalytic performance. Major products specific yield at (a) 648 K, (b) 673 K, and (c) 723 K

1 bar, $\tau = 1.5$ min·mg_{cat}·cm^{-3} (50 mg of catalyst, and 33.33 cm^3·min^{-1}), EtOH = 5 mol% in N_2, TOS = 2 h. CB for MgO-p, MgO-f, and MgO-w, respectively = 97.3, 98.3, and 95.3 % (at 648 K); 91.9, 93.6, and 99.8 % (at 723 K); and 68.6, 94.3, and 91.8 % (at 773 K).

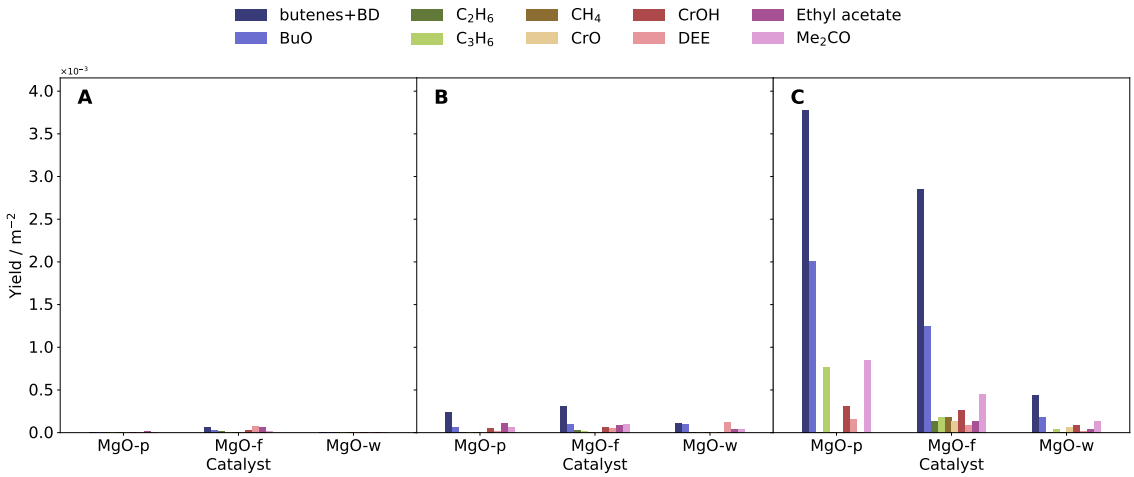

Figure B.2: Catalytic performance. Minor products specific yield at (a) 648 K, (b) 673 K, and (c) 723 K

1 bar, $\tau = 1.5$ min·mg_{cat}·cm^{-3} (50 mg of catalyst, and 33.33 cm^3·min^{-1}), EtOH = 5 mol% in N_2, TOS = 2 h. CB for MgO-p, MgO-f, and MgO-w, respectively = 97.3, 98.3, and 95.3 % (at 648 K); 91.9, 93.6, and 99.8 % (at 723 K); and 68.6, 94.3, and 91.8 % (at 773 K).

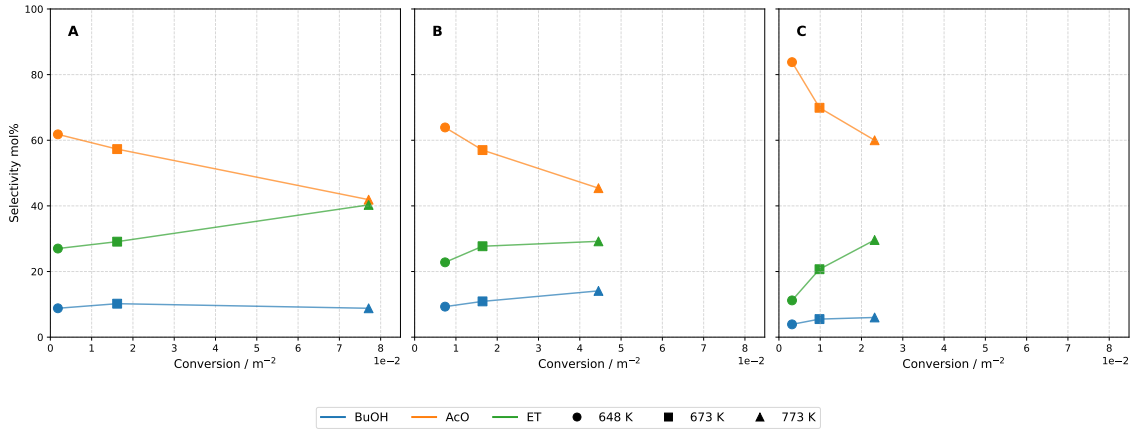

Figure B.3: Selectivity of main reaction products as a function of conversion for different catalysts and temperatures

Graphs A, B, and C represent catalysts MgO-p, MgO-f, and MgO-w, respectively. Different markers indicate reaction temperatures: circles (648 K), squares (673 K), and triangles (773 K). 1 bar, $\tau = 1.5$ min·mg_{cat}·cm^{-3} (50 mg of catalyst, and 33.33 cm^3·min^{-1}), EtOH = 5 mol% in N_2, TOS = 2 h. CB for MgO-p, MgO-f, and MgO-w, respectively = 97.3, 98.3, and 95.3 % (at 648 K); 91.9, 93.6, and 99.8 % (at 723 K); and 68.6, 94.3, and 91.8 % (at 773 K).

Appendix C

Derivation of E_{act} and ν_{eff} according to TST

Starting from the expression for the rate constant predicted by TST:

$$k_{\text{TST}} = \frac{k_B T}{h} \cdot e^{\Delta S_0^{\ddagger}/R} \cdot e^{-\Delta H_0^{\ddagger}/RT} \tag{C.1}$$

Taking the natural logarithm:

$$\ln k_{\text{TST}} = \ln\left(\frac{k_B T}{h}\right) + \frac{\Delta S_0^{\ddagger}}{R} - \frac{\Delta H_0^{\ddagger}}{RT} \tag{C.2}$$

Expanding the first term:

$$\ln\left(\frac{k_B T}{h}\right) = \ln\left(\frac{k_B}{h}\right) + \ln T \tag{C.3}$$

Thus:

$$\ln k_{\text{TST}} = \ln\left(\frac{k_B}{h}\right) + \ln T + \frac{\Delta S_0^{\ddagger}}{R} - \frac{\Delta H_0^{\ddagger}}{RT} \tag{C.4}$$

The apparent activation energy is defined as (MAO and CAMPBELL, 2019):

$$E_{\text{act}} = RT^2 \cdot \frac{\partial \ln k}{\partial T} \tag{C.5}$$

Applying this definition to Equation (C.4), we take the derivative term by term with respect to T:

- $\ln(k_B/h)$ and $\Delta S_0^{\ddagger}/R$ are constants: derivative is zero.
- $\frac{\partial \ln T}{\partial T} = \frac{1}{T}$
- $\frac{\partial}{\partial T}\left(-\frac{\Delta H_0^{\ddagger}}{RT}\right) = \frac{\Delta H_0^{\ddagger}}{RT^2}$

Therefore:

$$\frac{\partial \ln k_{\mathrm{TST}}}{\partial T} = \frac{1}{T} + \frac{\Delta H_0^{\ddagger}}{RT^2} \tag{C.6}$$

Substituting into Equation (C.5):

$$E_{\mathrm{act}} = RT^2 \left(\frac{1}{T} + \frac{\Delta H_0^{\ddagger}}{RT^2} \right) = RT + \Delta H_0^{\ddagger} \tag{C.7}$$

We now identify the effective frequency ν_{eff}, which corresponds to the pre-exponential factor of the Arrhenius expression written as:

$$k = \nu_{\mathrm{eff}} \cdot e^{-E_{\mathrm{act}}/RT} \tag{C.8}$$

From Equation (C.1), and using $\Delta H_0^{\ddagger} = E_{\mathrm{act}} - RT$, we can rewrite:

$$k_{\mathrm{TST}} = \frac{k_B T}{h} \cdot e^{\Delta S_0^{\ddagger}/R} \cdot e^{-(E_{\mathrm{act}} - RT)/RT} = \frac{k_B T}{h} \cdot e^{\Delta S_0^{\ddagger}/R} \cdot e \cdot e^{-E_{\mathrm{act}}/RT}$$

Grouping the pre-exponential terms:

$$k_{\mathrm{TST}} = \left(\frac{k_B T}{h} \cdot e^{\frac{\Delta S_0^{\ddagger}}{R} + 1} \right) \cdot e^{-E_{\mathrm{act}}/RT}$$

We define the activation entropy as:

$$\Delta S_{\mathrm{act}} = \Delta S_0^{\ddagger} + R \tag{C.9}$$

Thus, the effective frequency is given by:

$$\nu_{\mathrm{eff}} = \frac{k_B T}{h} \cdot e^{\Delta S_{\mathrm{act}}/R} \tag{C.10}$$

Appendix D

Chosen Fragments for Mass Spectra Analysis

m/z	H_2	CO	CO_2	H_2O	ET	AcO	Acetone	EtOH	1-BT	(E)-2-BT	(Z)-2-BT	i-BT	BD	BuO	(E)-Cro-OH	(Z)-Cro-OH	BuOH	3-Bu-2-OH	(E)-CRO	(Z)-CRO	DEE
2	100																				
12		5	11												28	71	39				
14						11											43				
15						38										14					
16			11																		
17				21																	
18				100																	
26					57			11					18						18		
27					62			23		35	23	20	50	60			20	30	49		19
28		100	11		100				43	33	25	20	38	15							
29						100		30	20	20	14			55				28	39		43
30								10									11				
31								100													100
37																			18		
38																12	14		29		
39									60	35	32	52	100	23	12	14		4	98	85	
40															24	29	83		28		
41									100	100	100	100		61	29	55	26		100		
42						16													30		
43						49	100	12						79				73			
44			100			83								100							
45								51							23	29	98	32			46
46								23													
50													28		23	43	50				
51													27			11					
53													70								
54													98								
55									38								30				
56										47	59	45					100				
57														25	100	100					
58							25														
59																					70
69															26	41	59		65	45	
70																13		100	81	100	
71																		8			
72														75	34	21					
74																					45

Figure D.1: Main mass fragments (m/z) associated with the expected products and intermediates from EtOH reaction over MgO, identified by MS. *Source:* NIST

The listed fragments were used for qualitative compound identification during the reactivity experiments.

Appendix E

Micro-FTIR

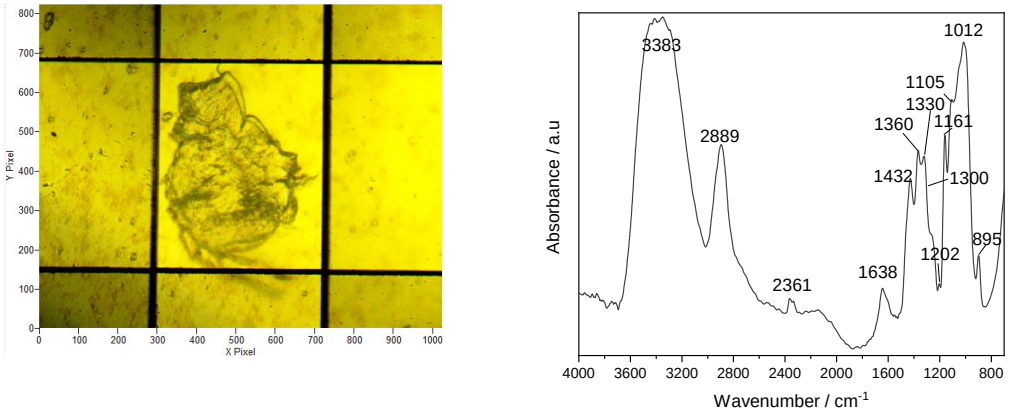

(a) optical image of a single particle (b) local FTIR absorbance spectrum

Figure E.1: FTIR spectrum of the MgO-p particle after EETPD procedure at 673 K

Appendix F

SINS area-spectra

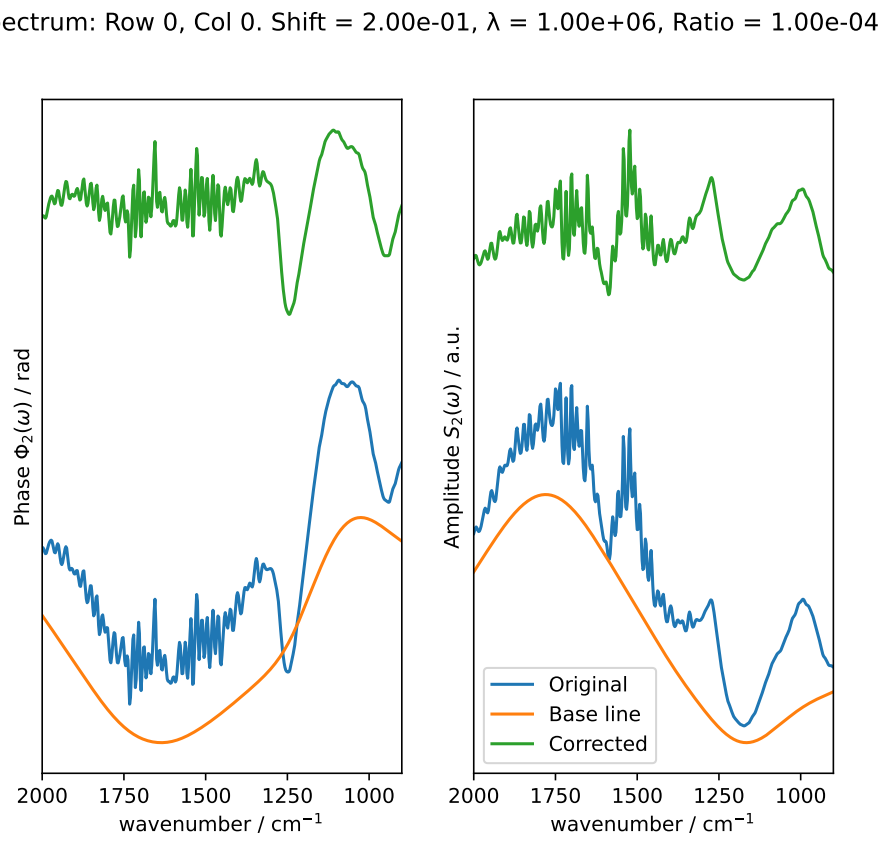

Figure F.1: SINS baseline spectrum for position (0,0).

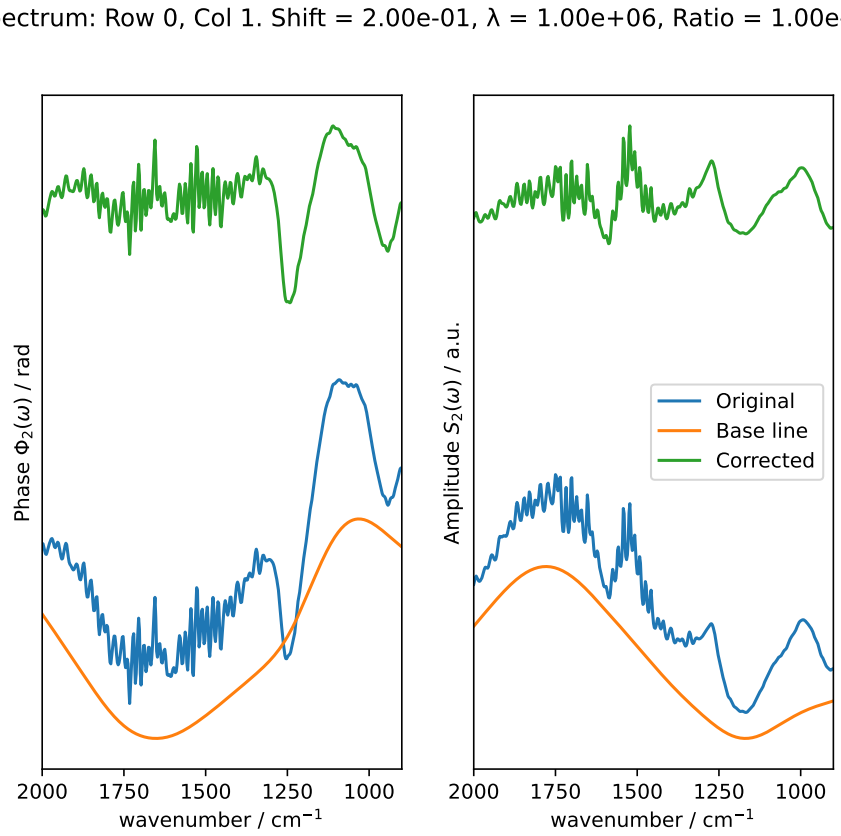

Figure F.2: SINS baseline spectrum for position (0,1).

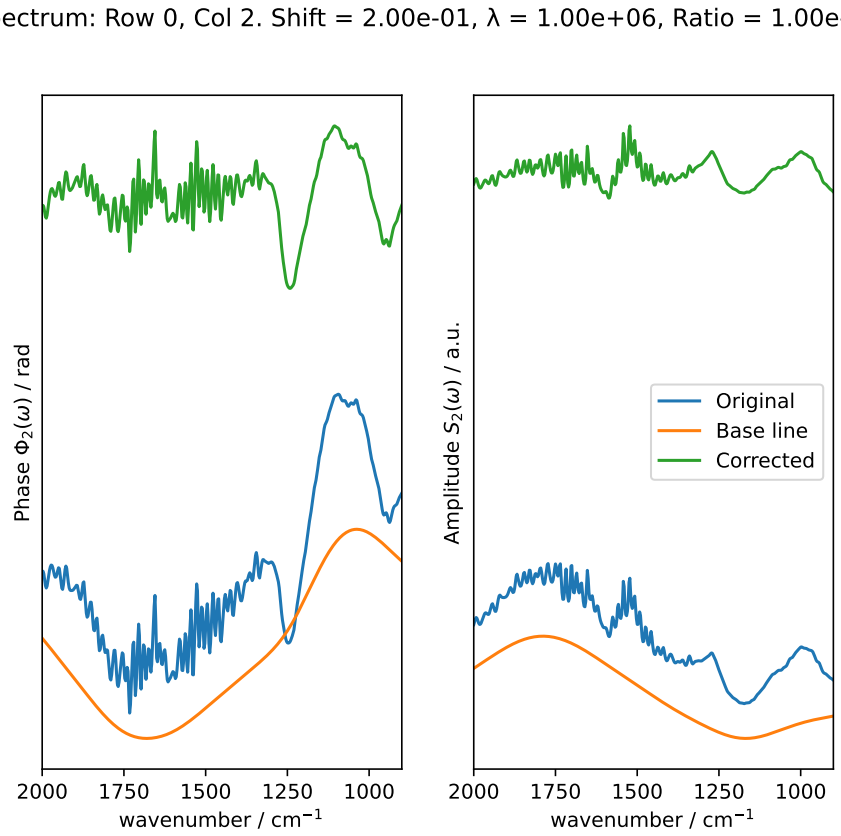

Figure F.3: SINS baseline spectrum for position (0,2).

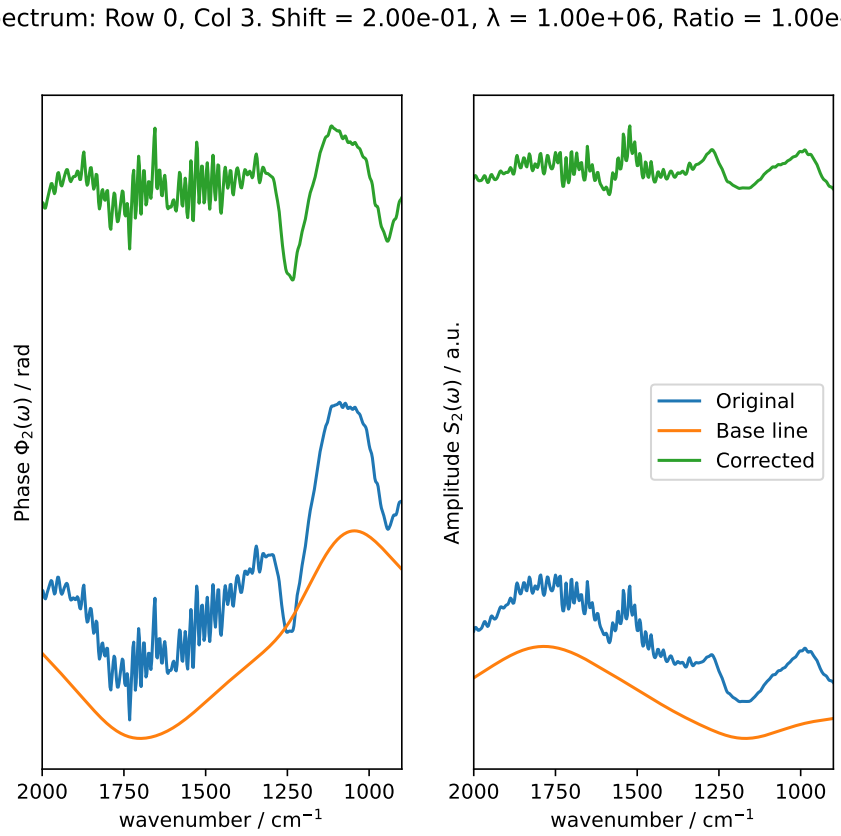

Figure F.4: SINS baseline spectrum for position (0,3).

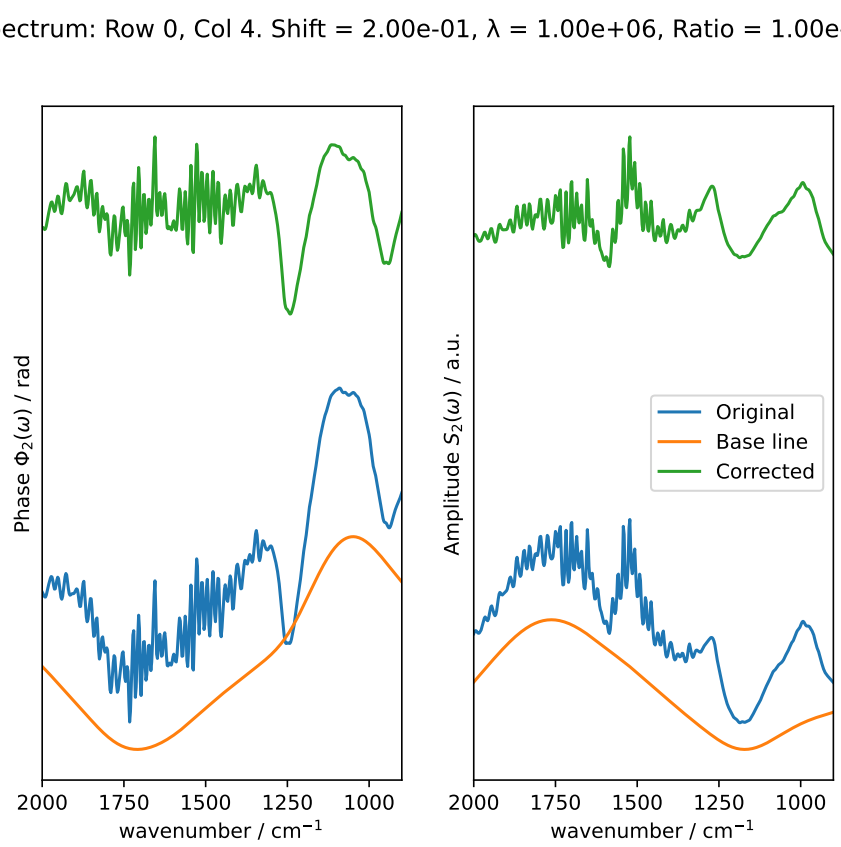

Figure F.5: SINS baseline spectrum for position (0,4).

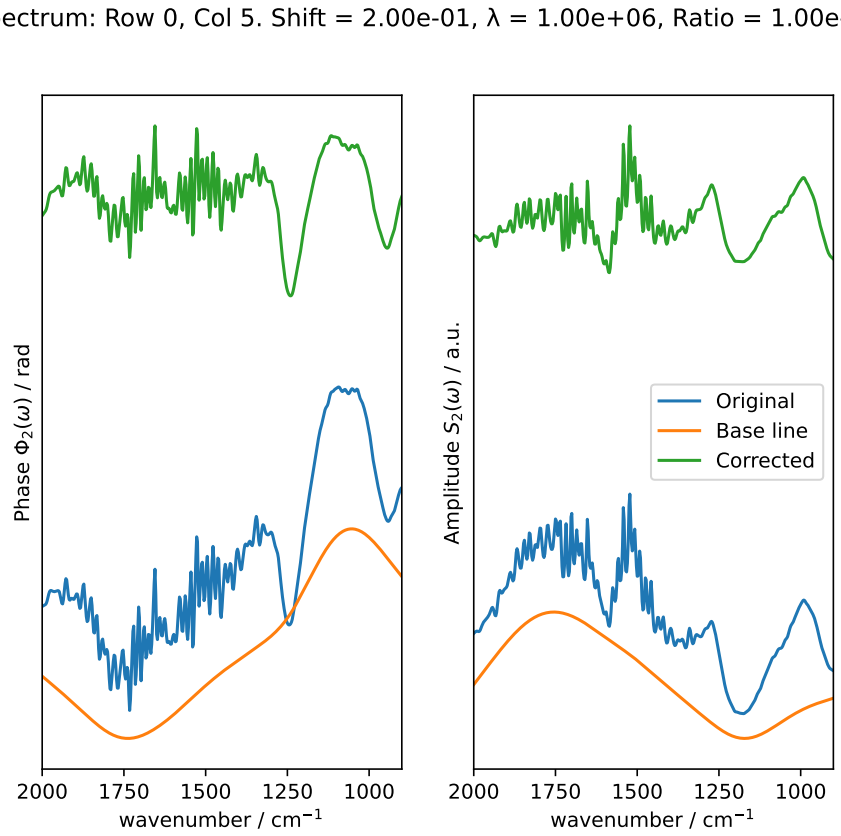

Figure F.6: SINS baseline spectrum for position (0,5).

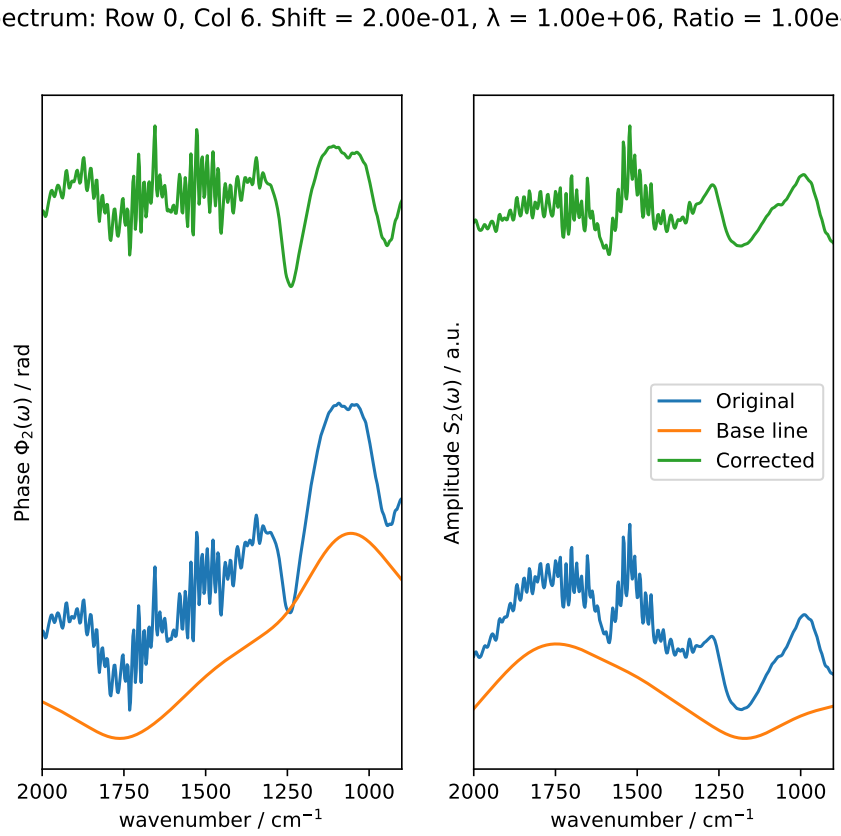

Figure F.7: SINS baseline spectrum for position (0,6).

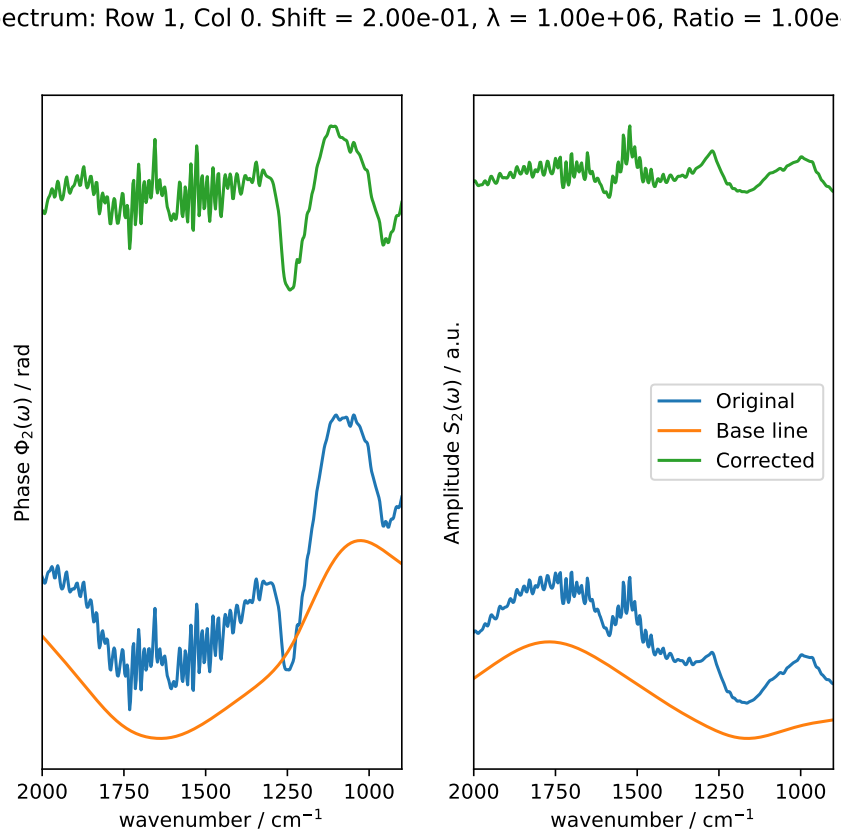

Figure F.8: SINS baseline spectrum for position (1,0).

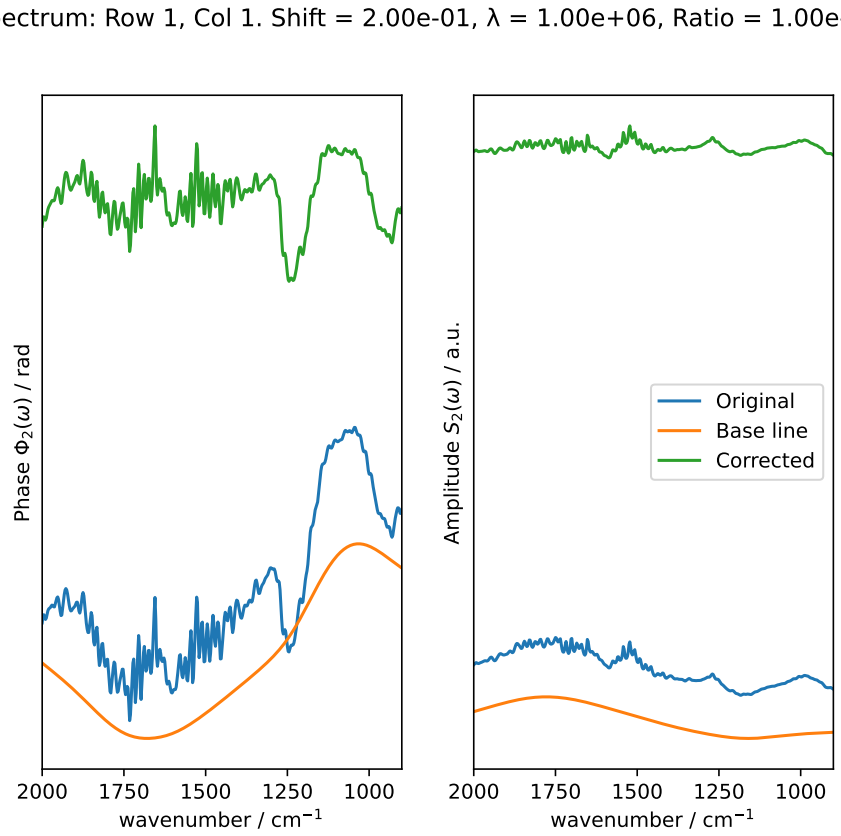

Figure F.9: SINS baseline spectrum for position (1,1).

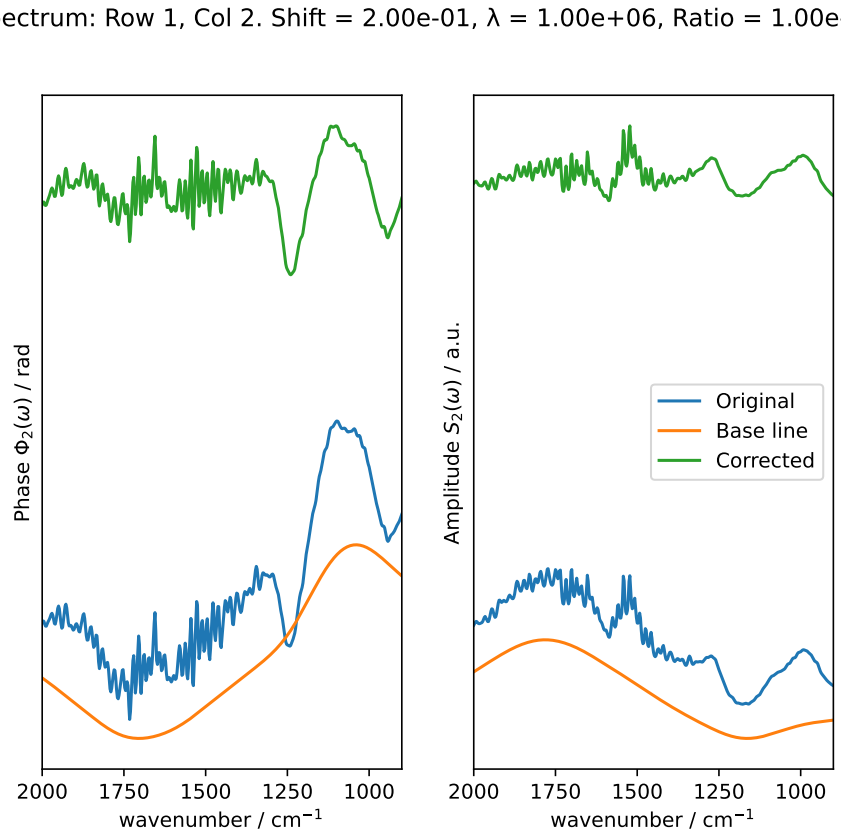

Figure F.10: SINS baseline spectrum for position (1,2).

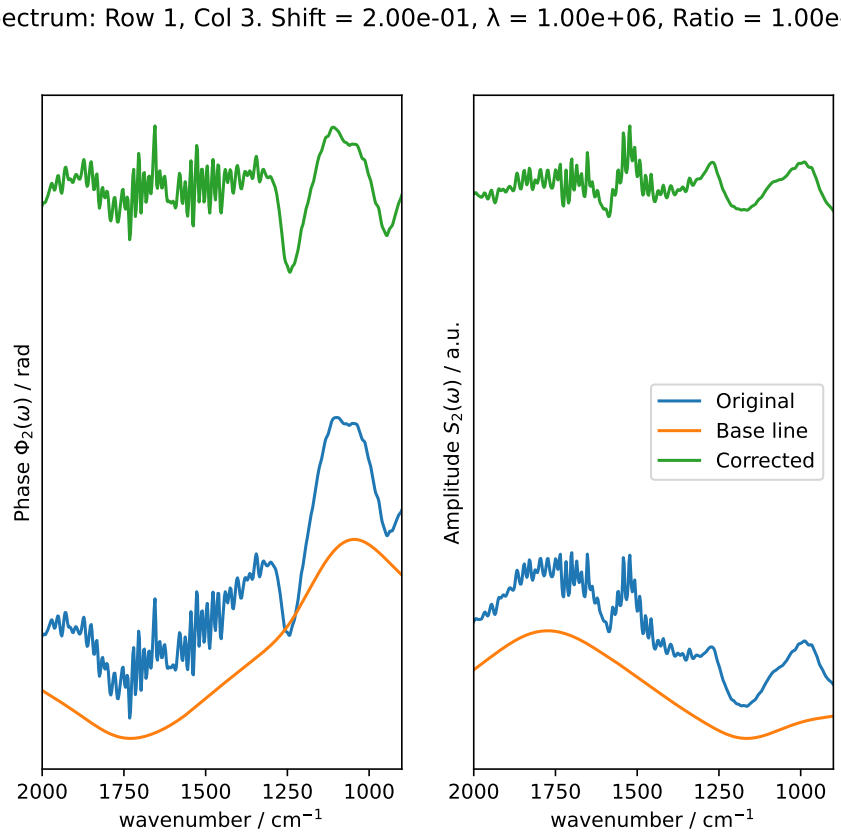

Figure F.11: SINS baseline spectrum for position (1,3).

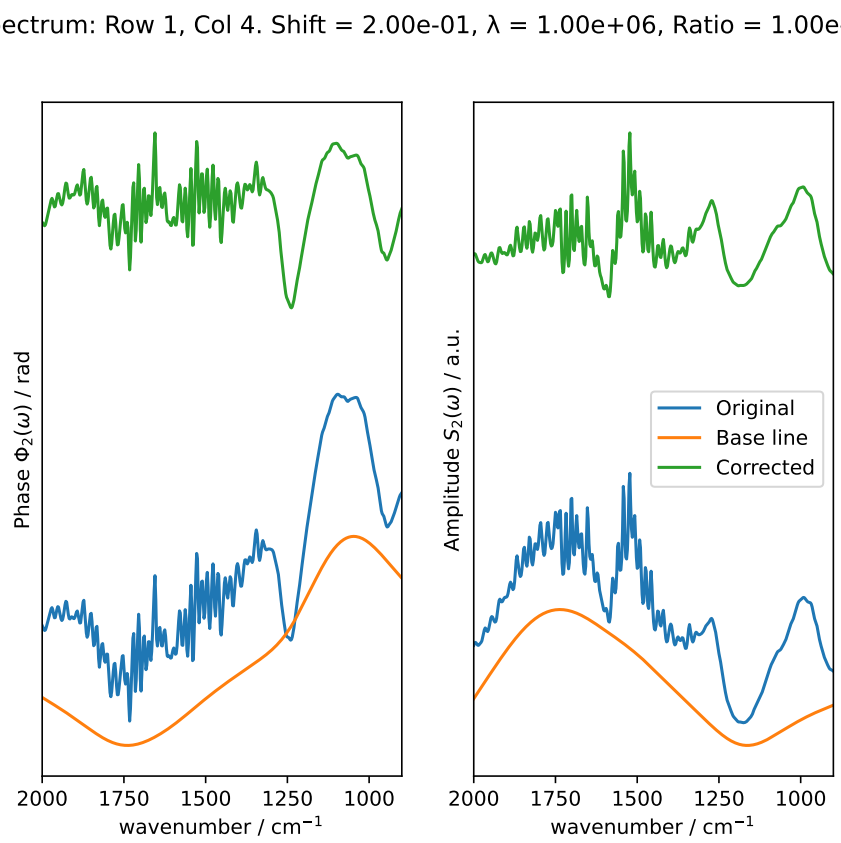

Figure F.12: SINS baseline spectrum for position (1,4).

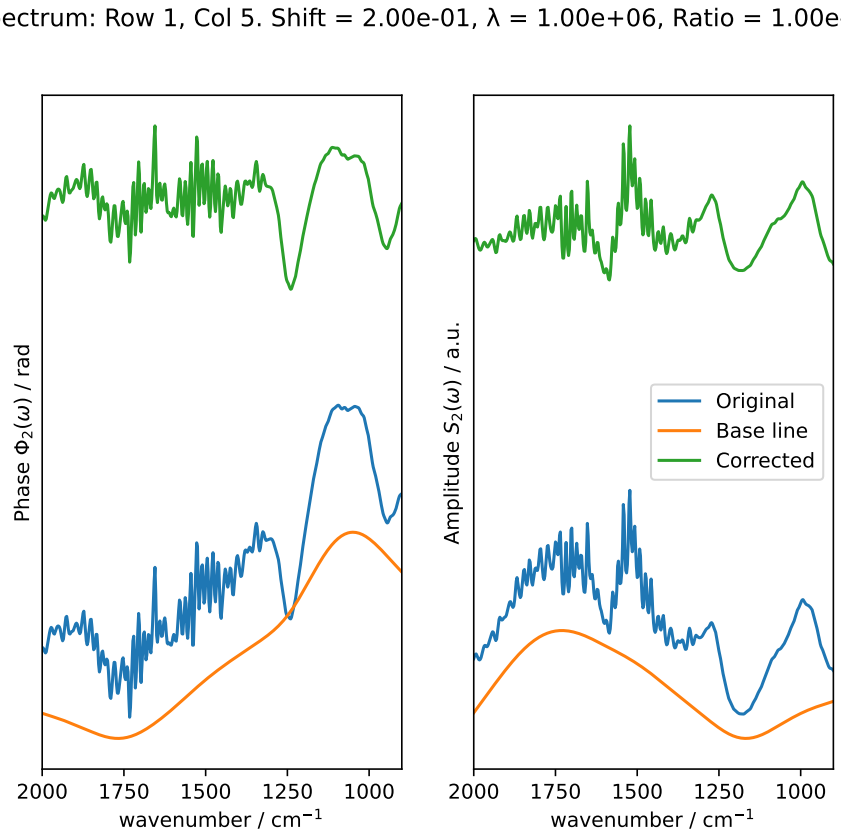

Figure F.13: SINS baseline spectrum for position (1,5).

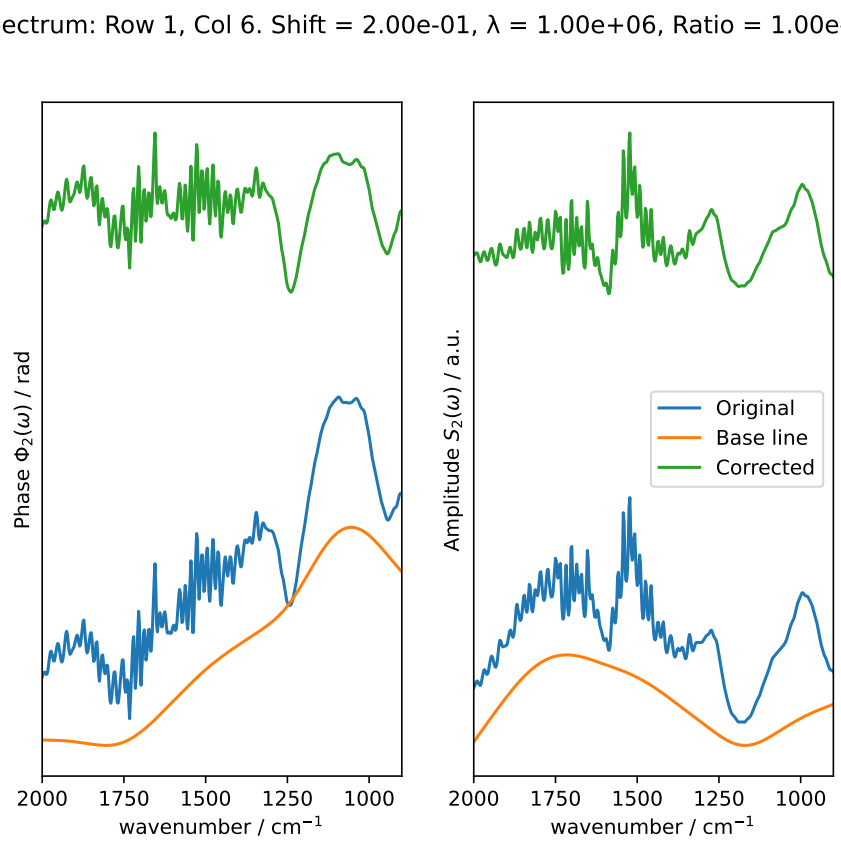

Figure F.14: SINS baseline spectrum for position (1,6).

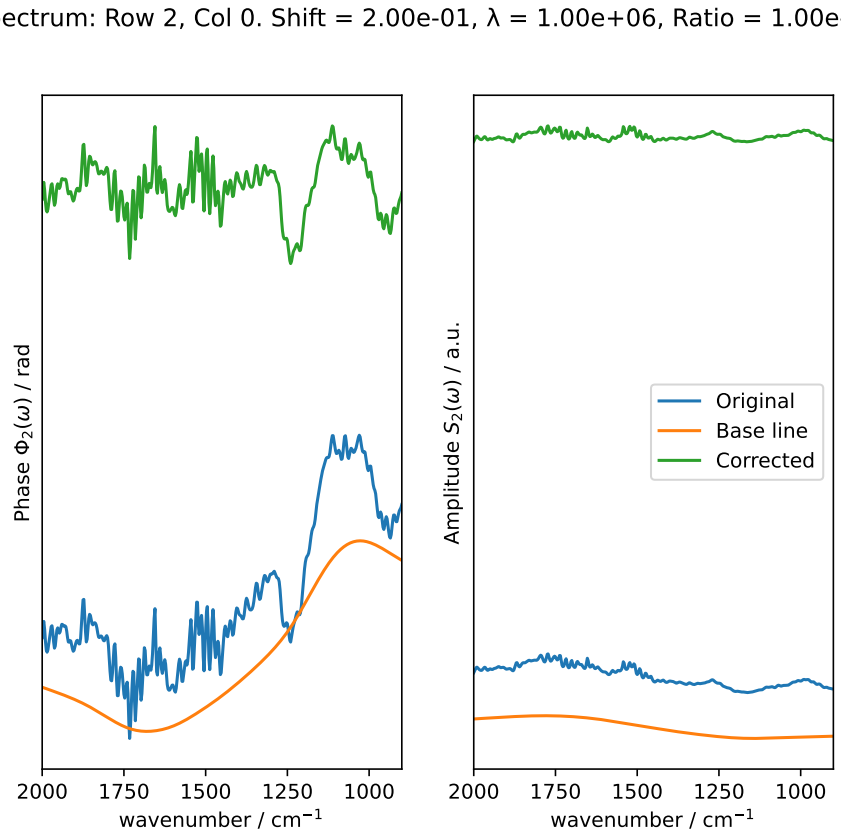

Figure F.15: SINS baseline spectrum for position (2,0).

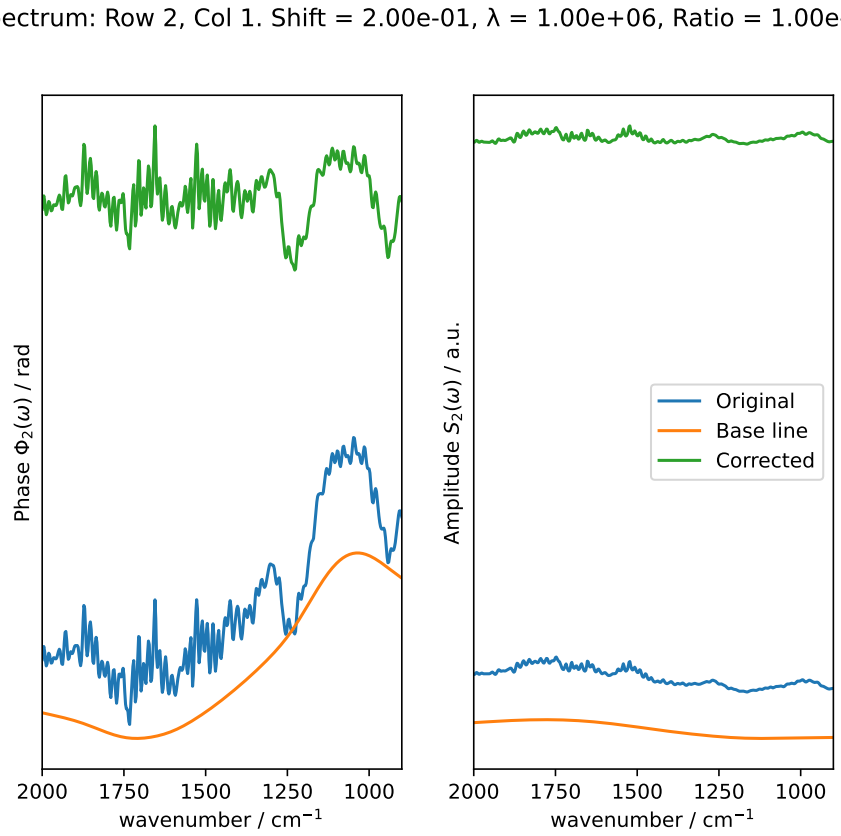

Figure F.16: SINS baseline spectrum for position (2,1).

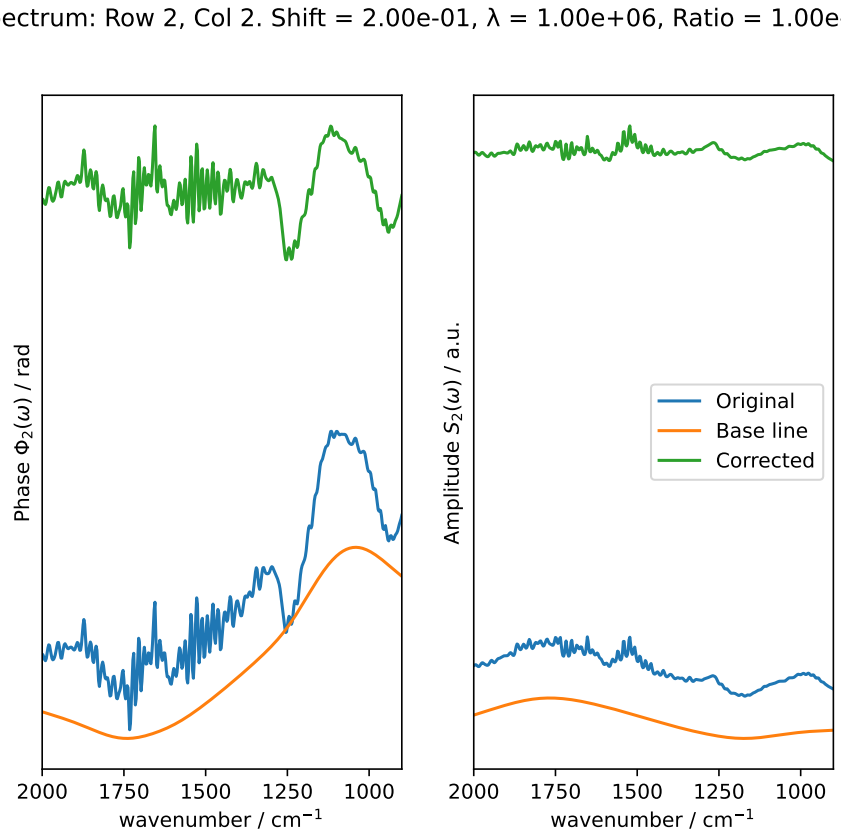

Figure F.17: SINS baseline spectrum for position (2,2).

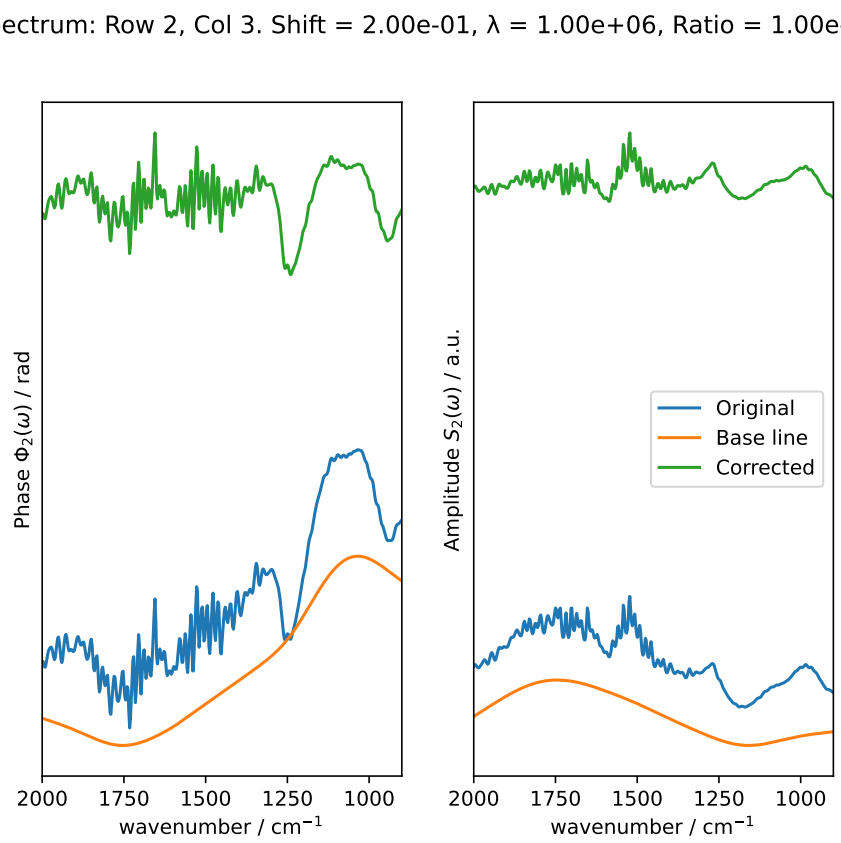

Figure F.18: SINS baseline spectrum for position (2,3).

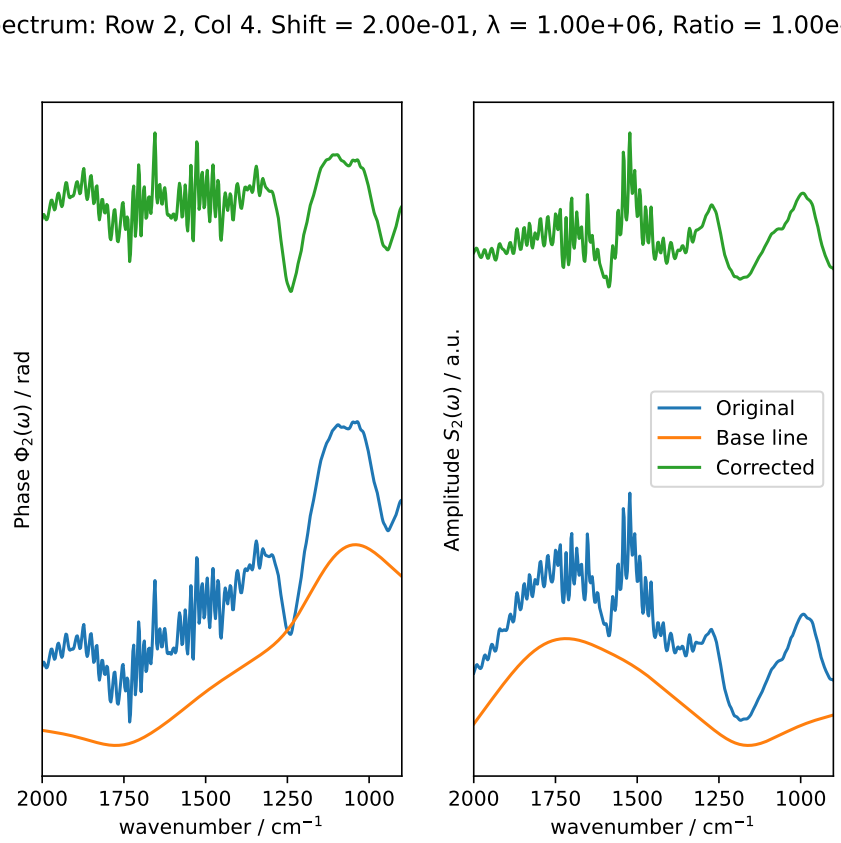

Figure F.19: SINS baseline spectrum for position (2,4).

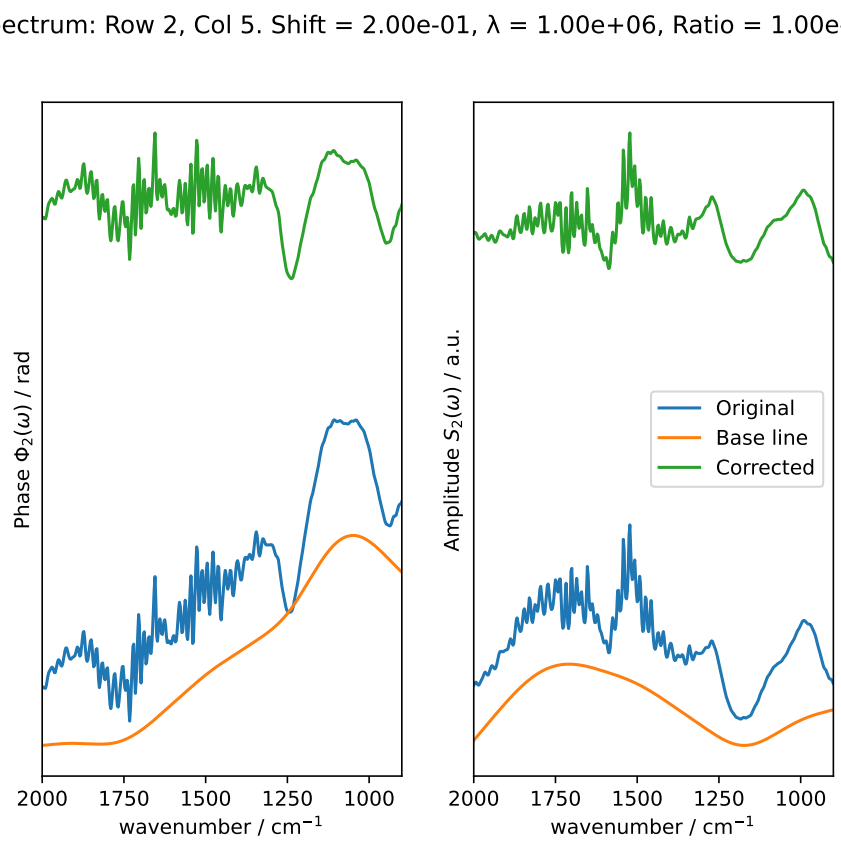

Figure F.20: SINS baseline spectrum for position (2,5).

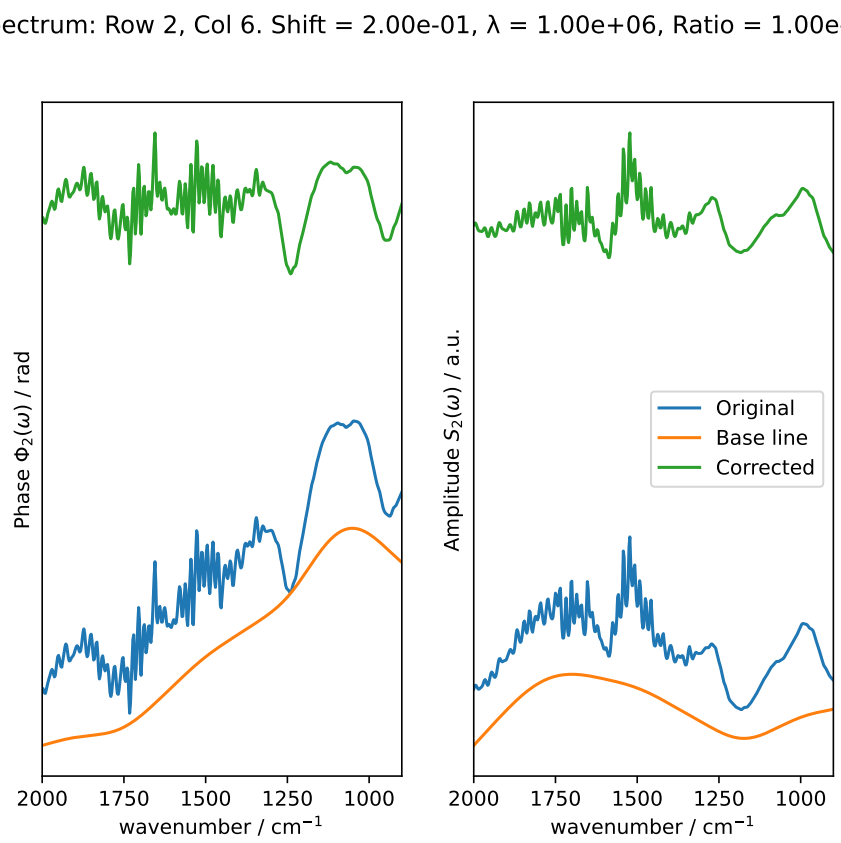

Figure F.21: SINS baseline spectrum for position (2,6).

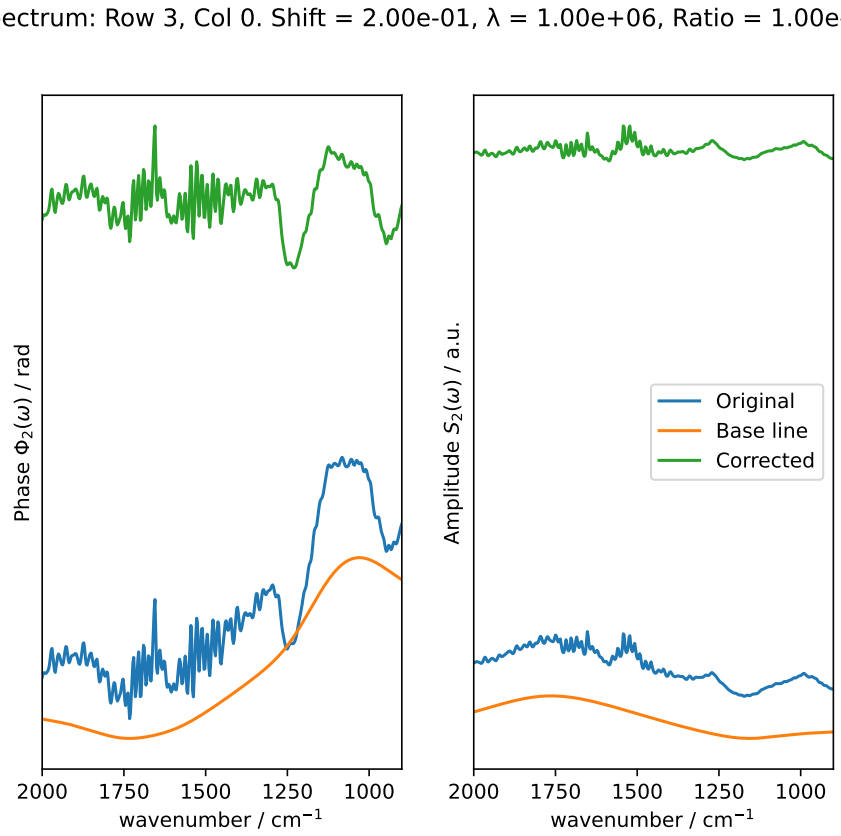

Figure F.22: SINS baseline spectrum for position (3,0).

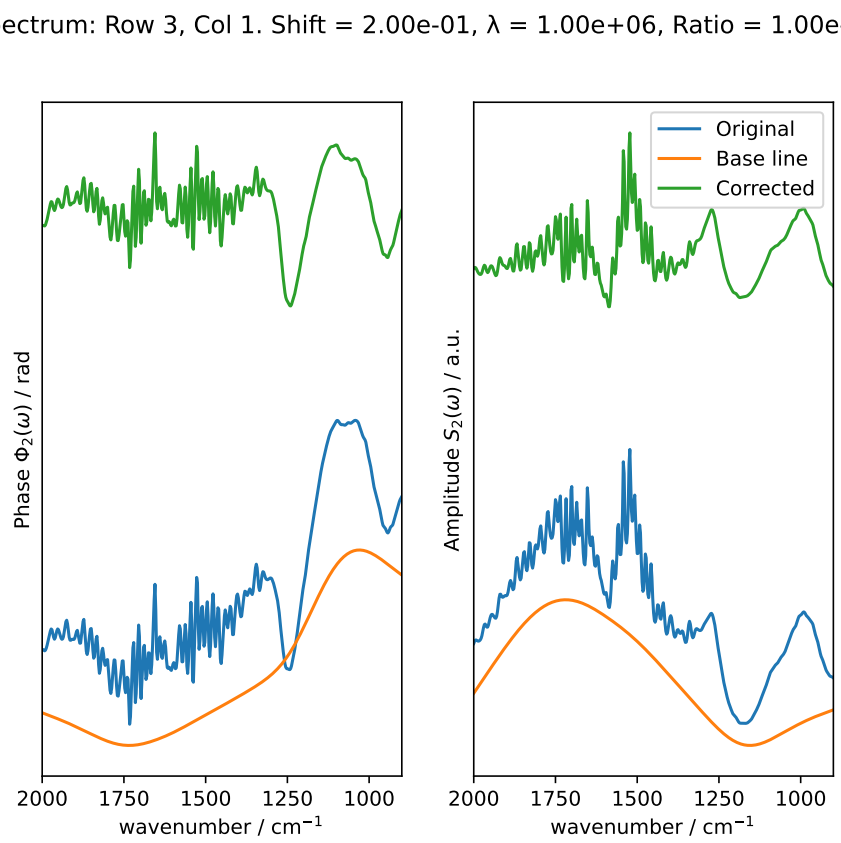

Figure F.23: SINS baseline spectrum for position (3,1).

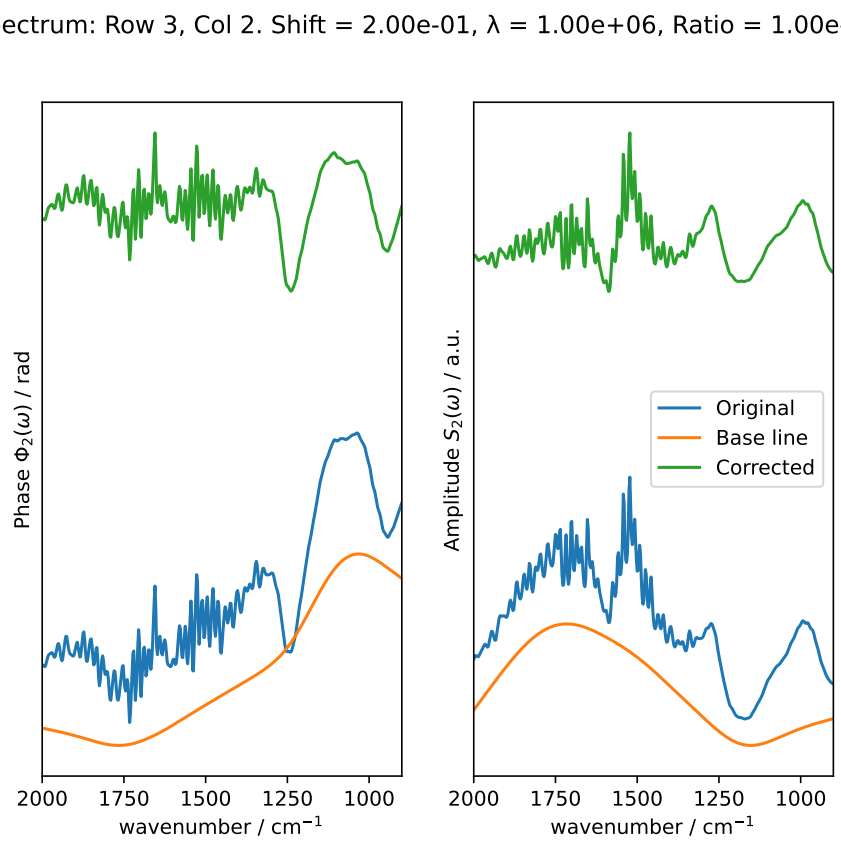

Figure F.24: SINS baseline spectrum for position (3,2).

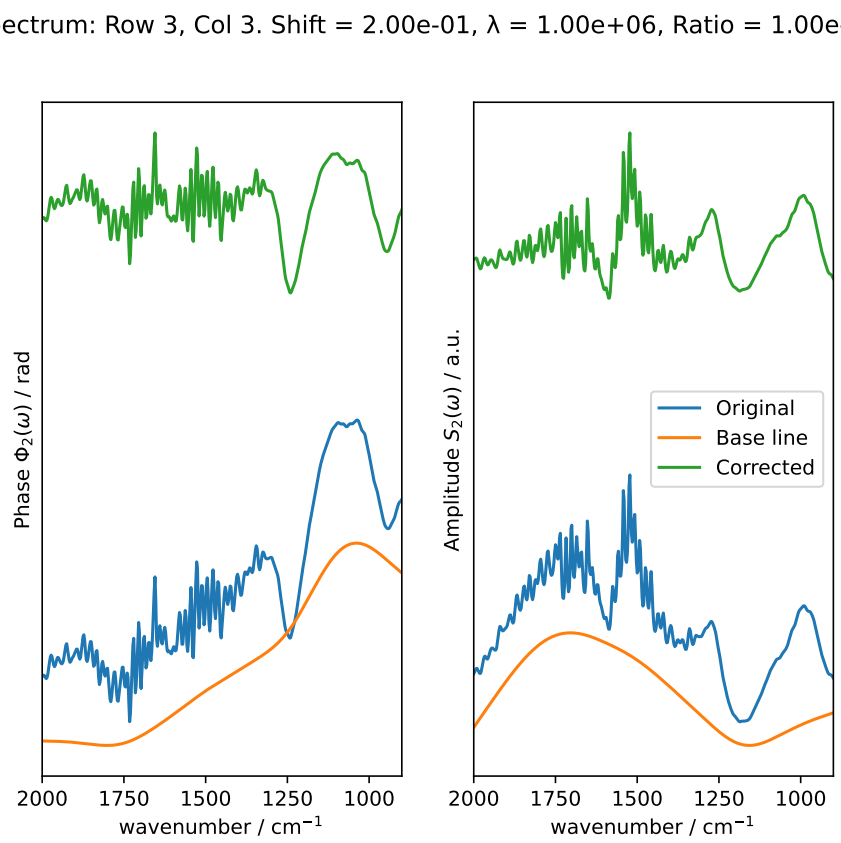

Figure F.25: SINS baseline spectrum for position (3,3).

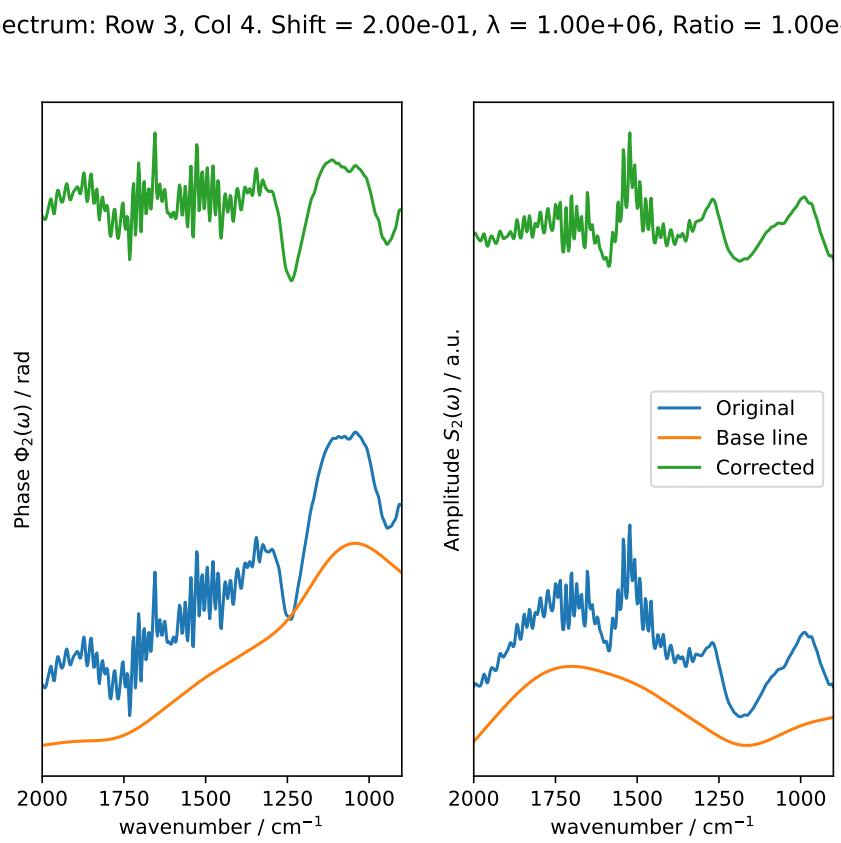

Figure F.26: SINS baseline spectrum for position (3,4).

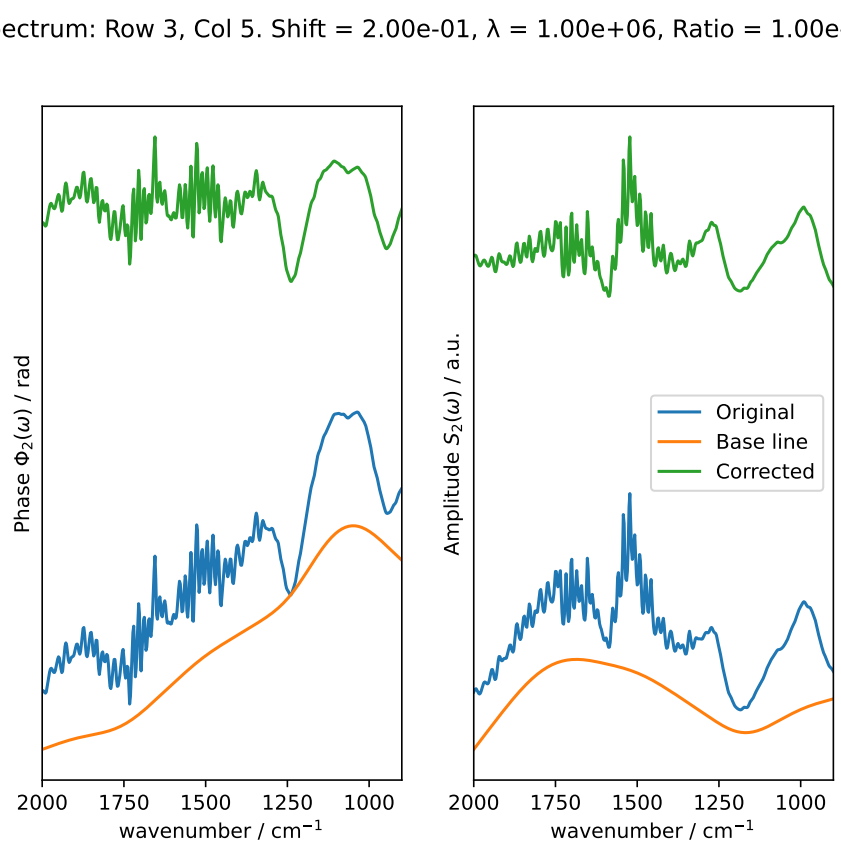

Figure F.27: SINS baseline spectrum for position (3,5).

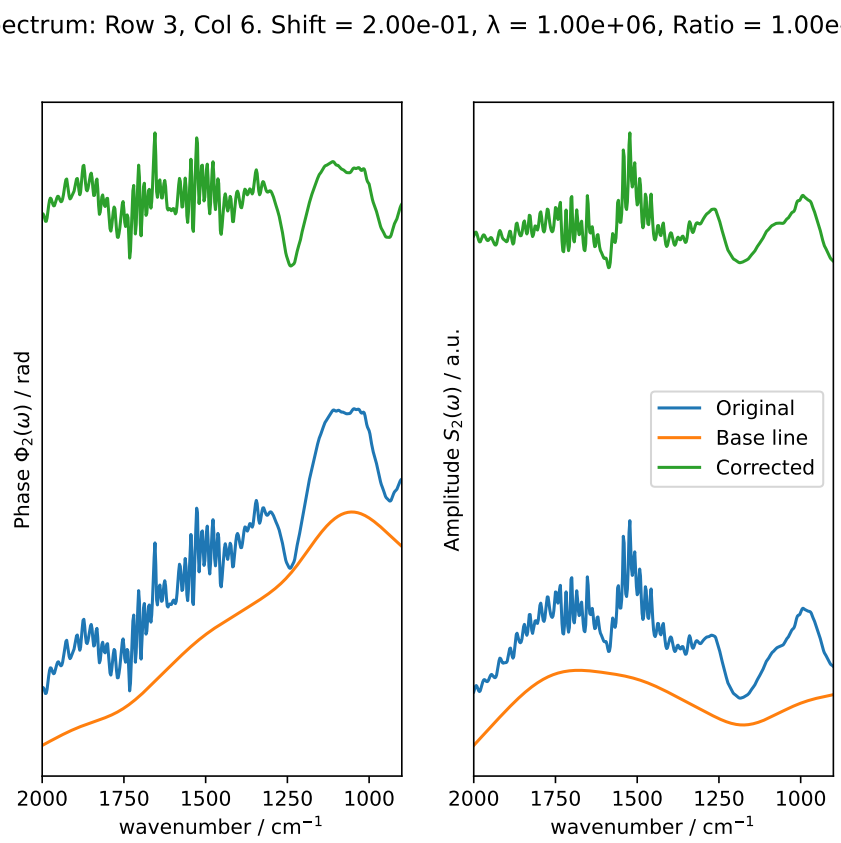

Figure F.28: SINS baseline spectrum for position (3,6).

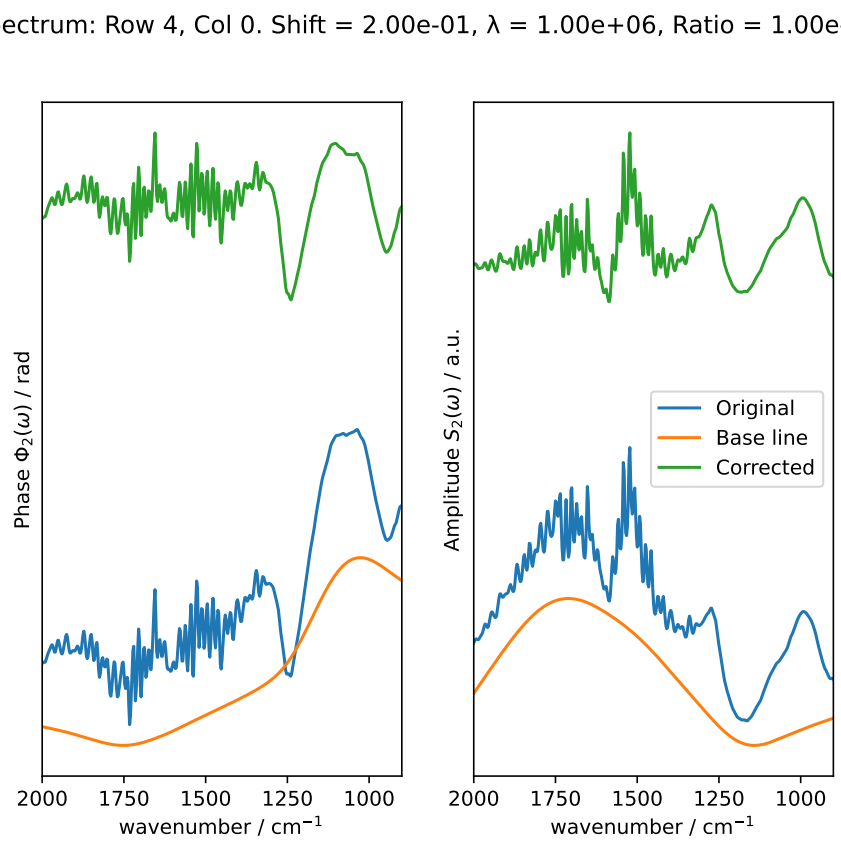

Figure F.29: SINS baseline spectrum for position (4,0).

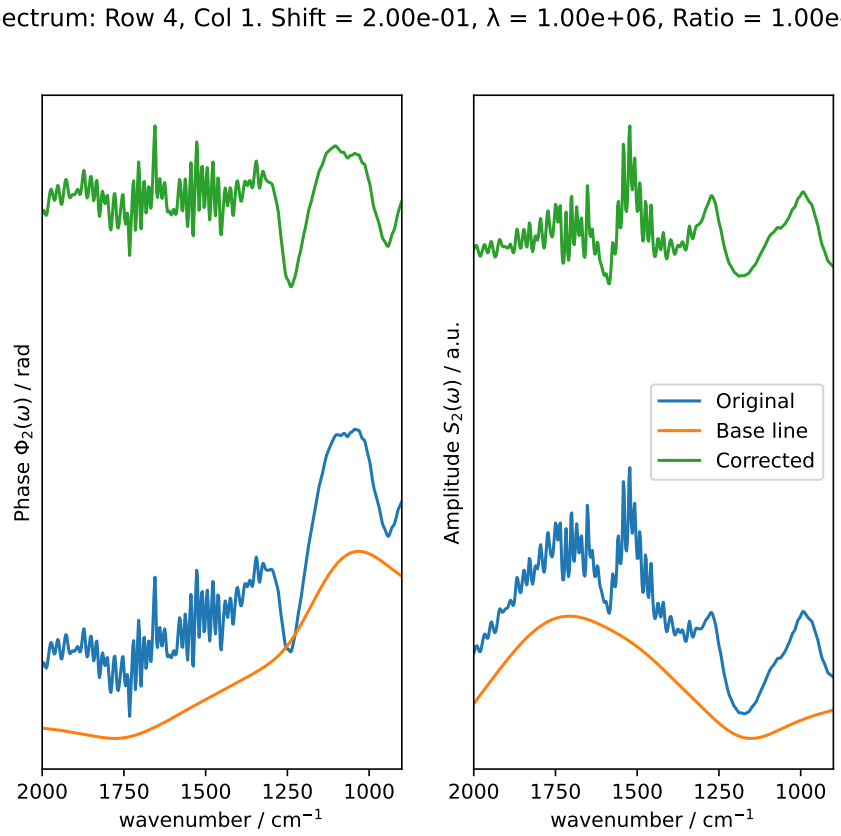

Figure F.30: SINS baseline spectrum for position (4,1).

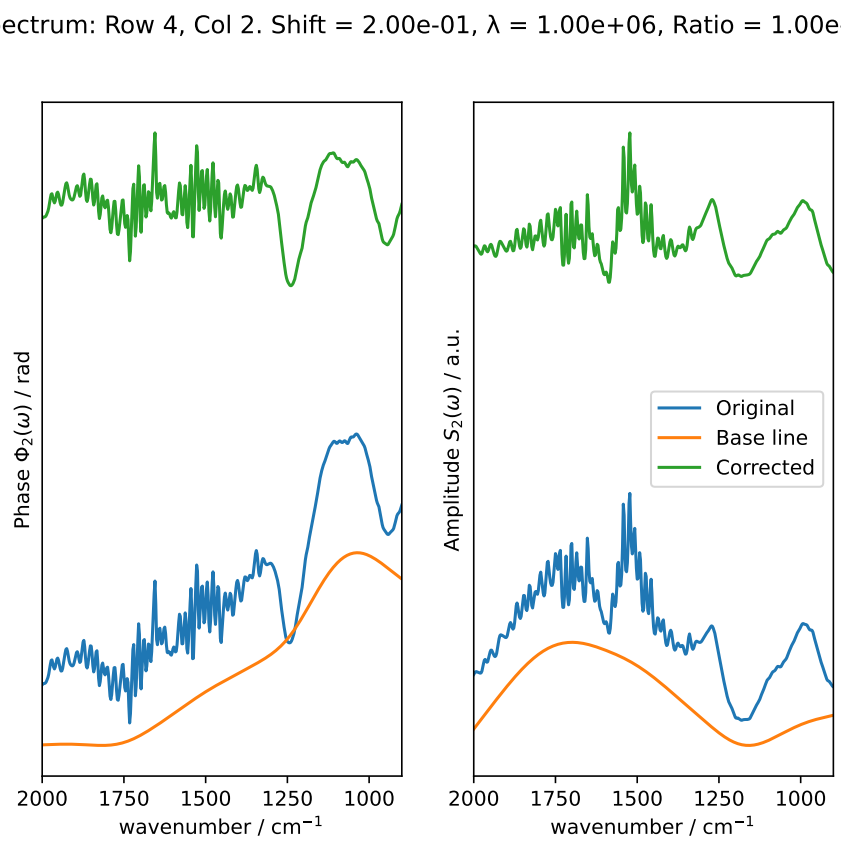

Figure F.31: SINS baseline spectrum for position (4,2).

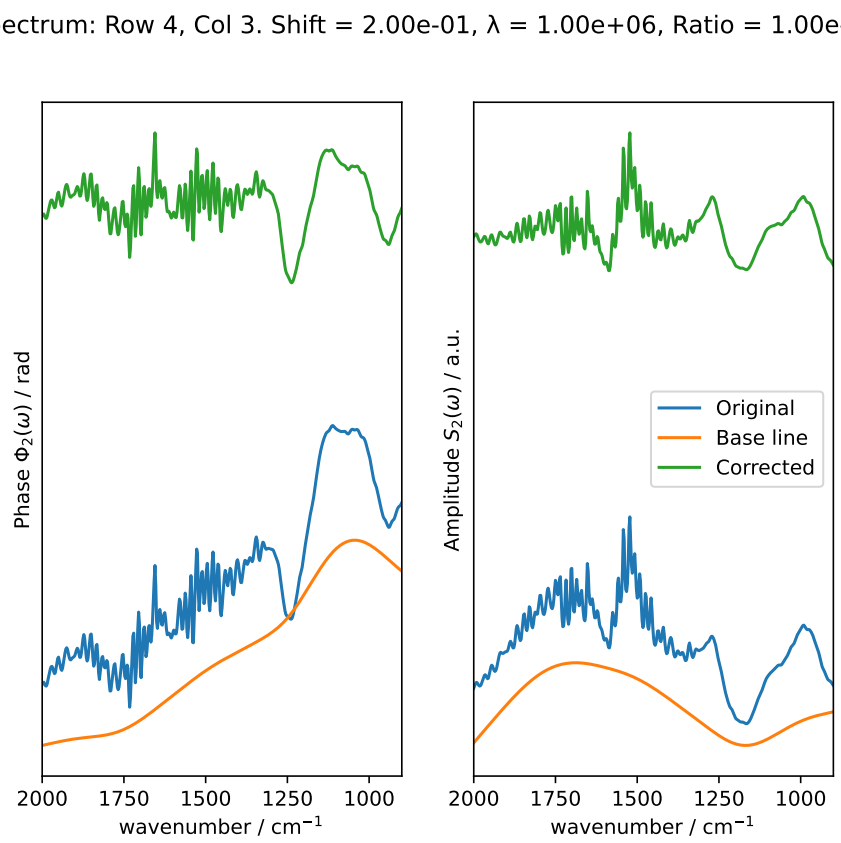

Figure F.32: SINS baseline spectrum for position (4,3).

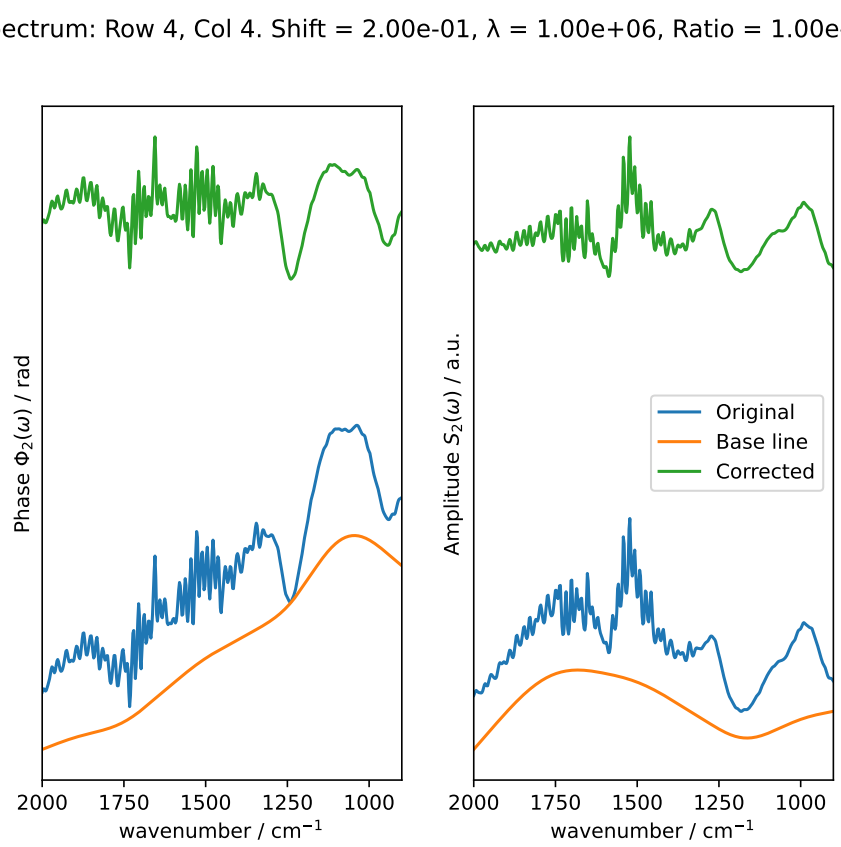

Figure F.33: SINS baseline spectrum for position (4,4).

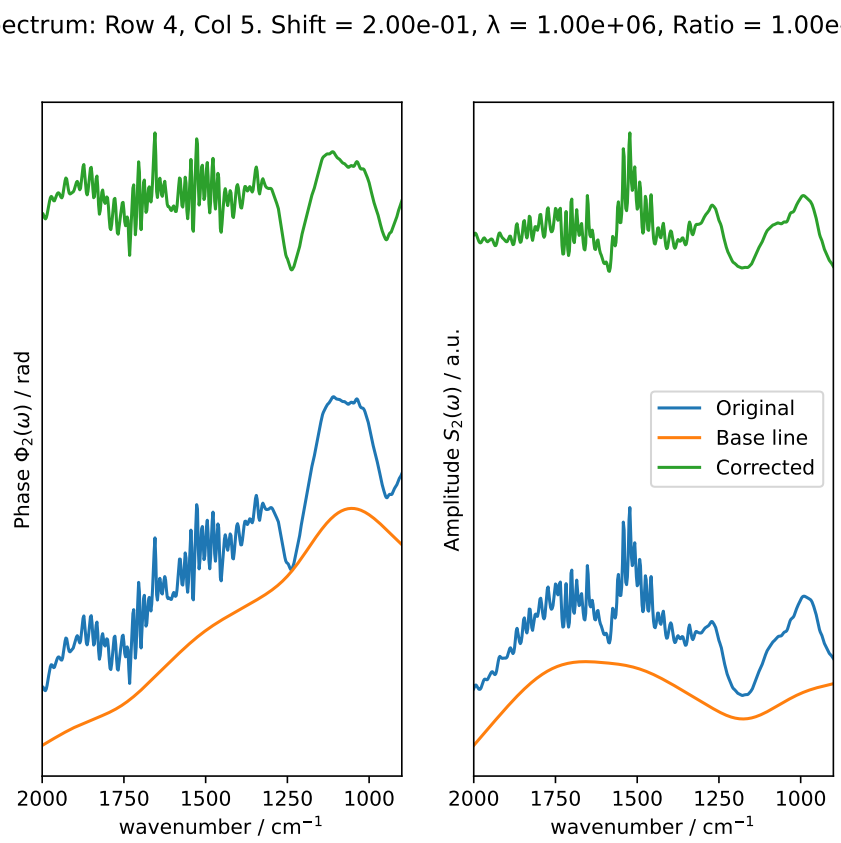

Figure F.34: SINS baseline spectrum for position (4,5).

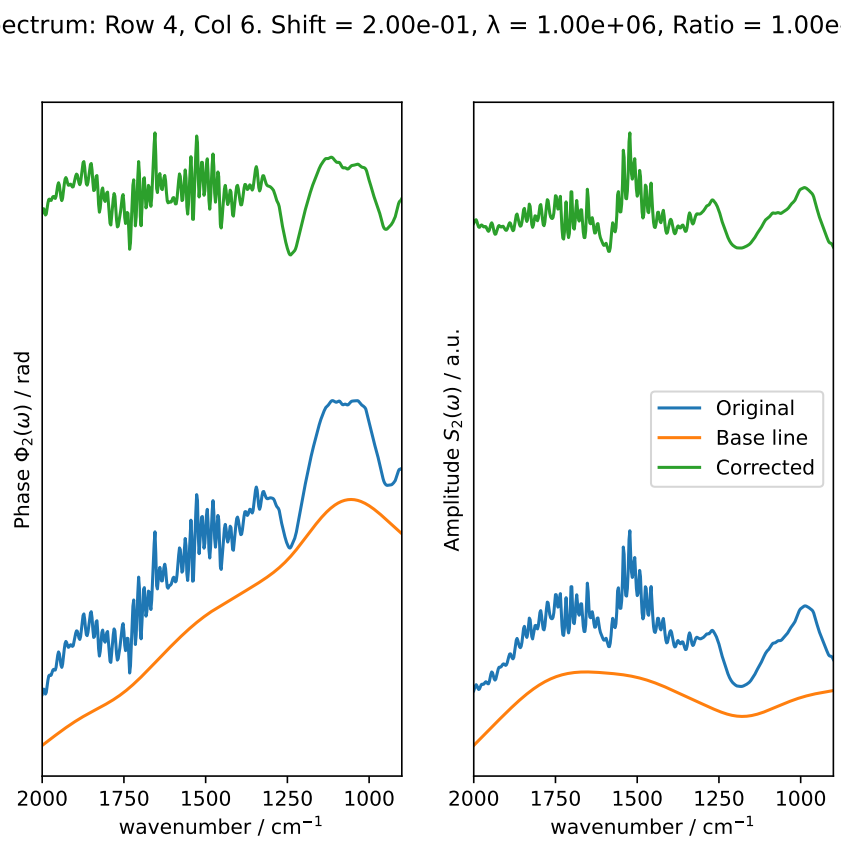

Figure F.35: SINS baseline spectrum for position (4,6).

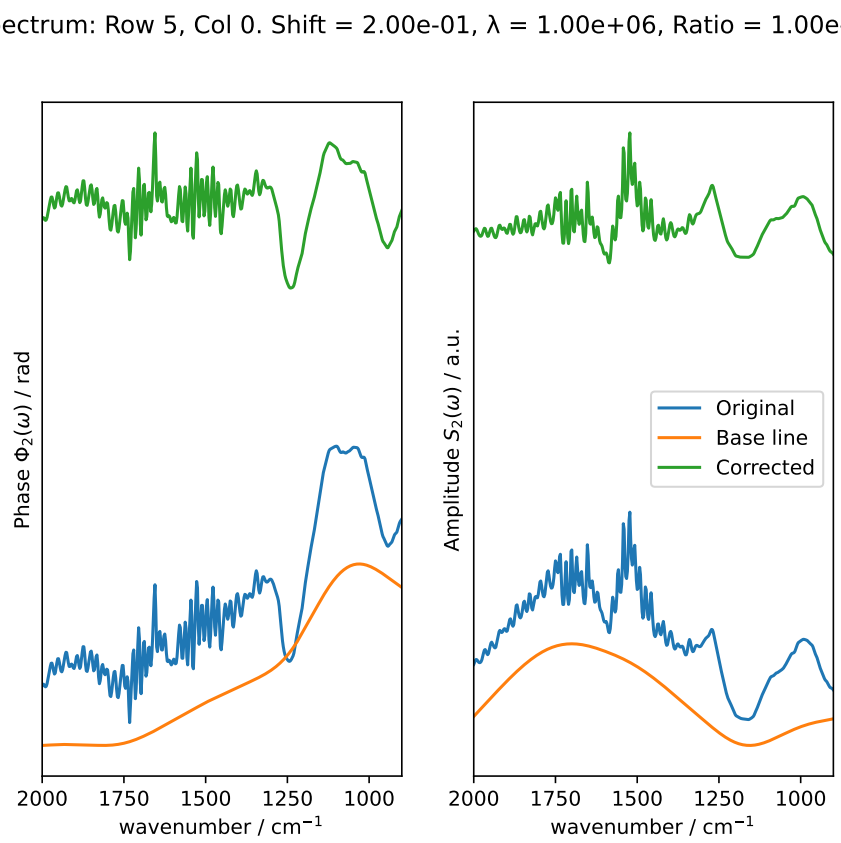

Figure F.36: SINS baseline spectrum for position (5,0).

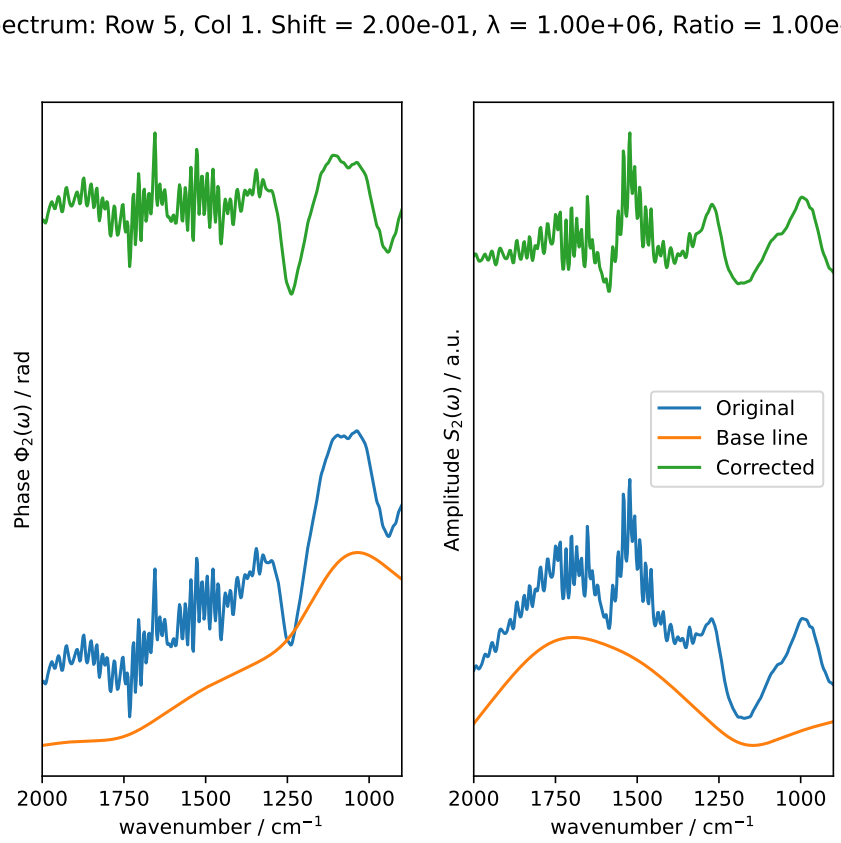

Figure F.37: SINS baseline spectrum for position (5,1).

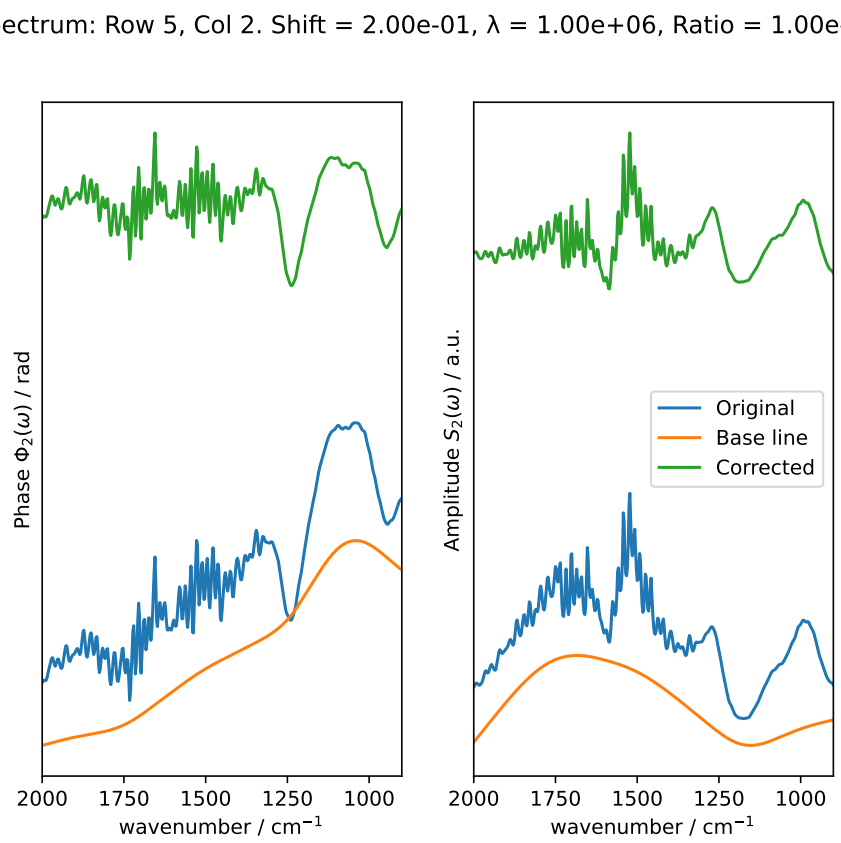

Figure F.38: SINS baseline spectrum for position (5,2).

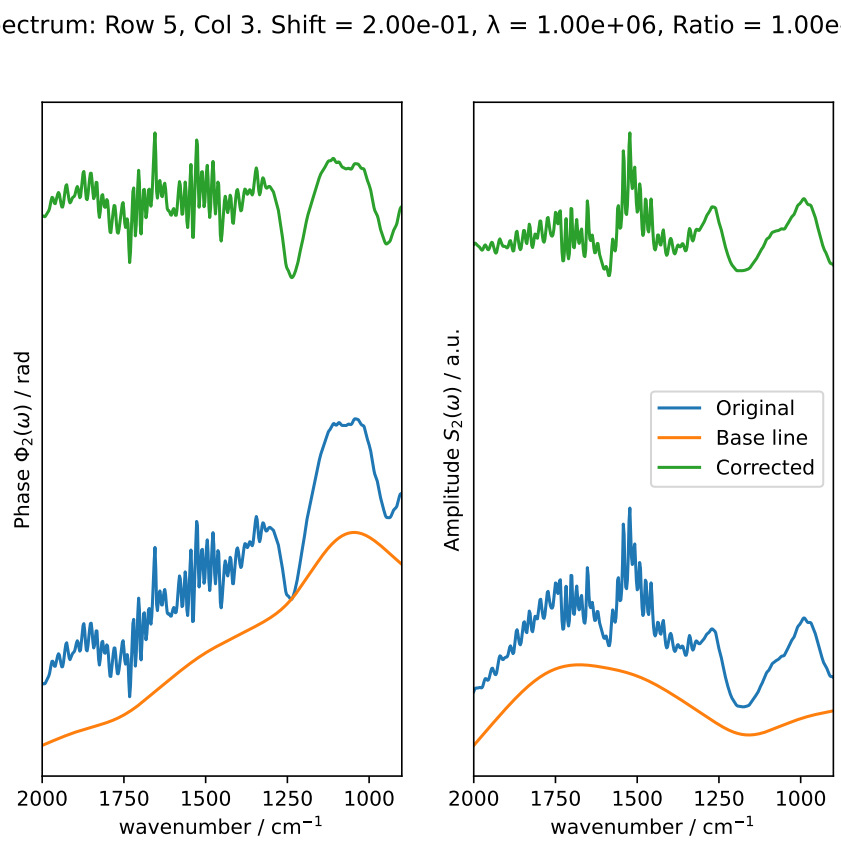

Figure F.39: SINS baseline spectrum for position (5,3).

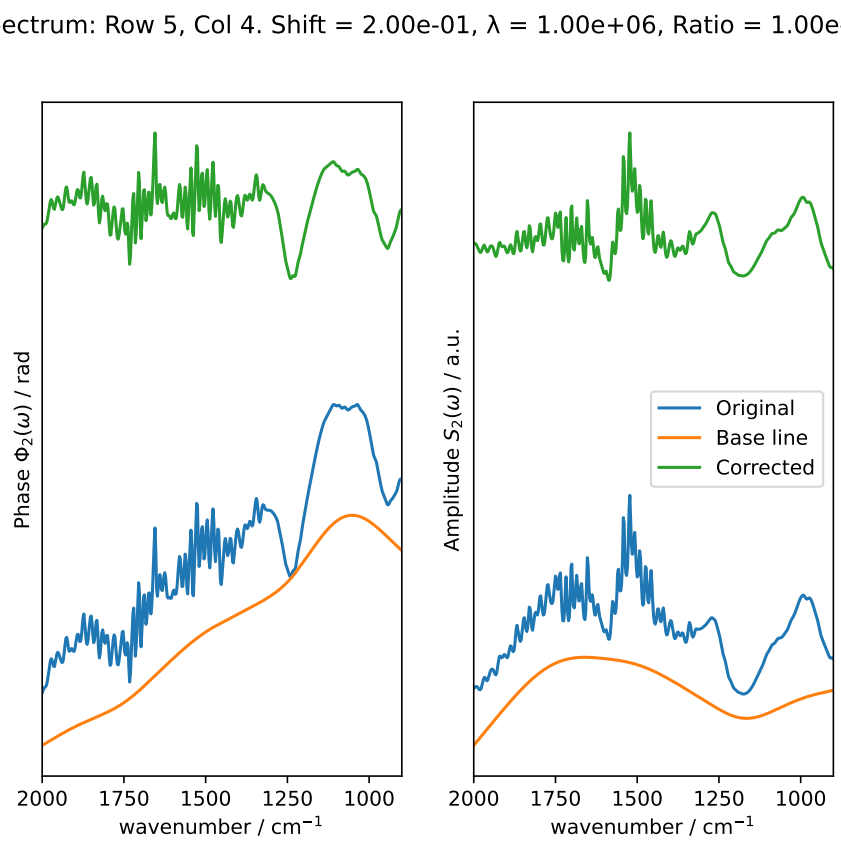

Figure F.40: SINS baseline spectrum for position (5,4).

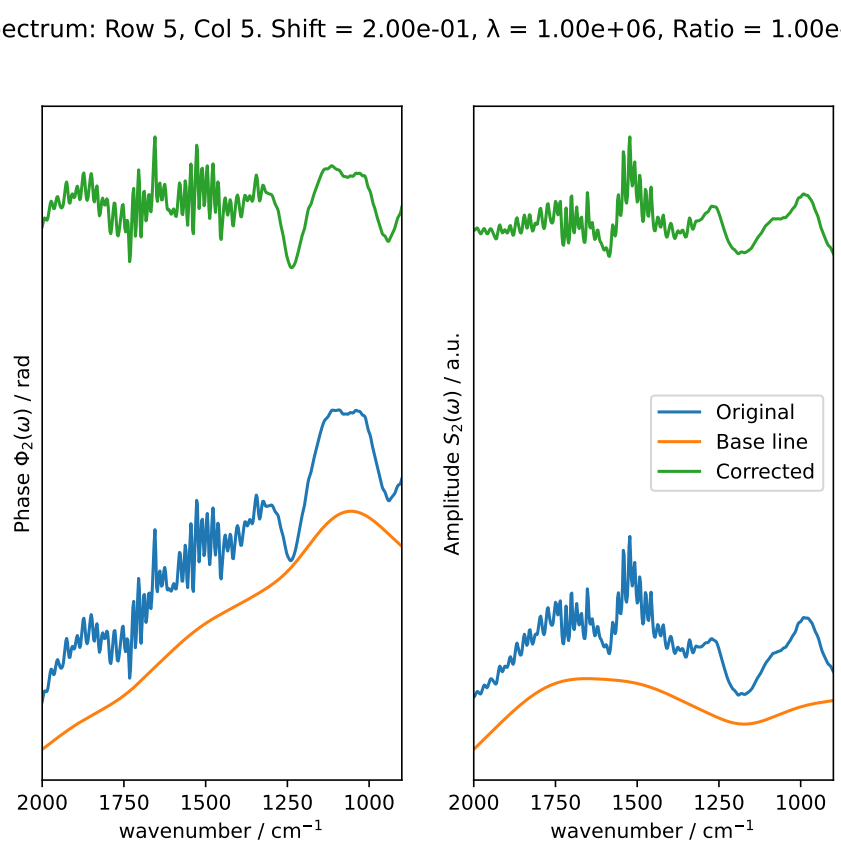

Figure F.41: SINS baseline spectrum for position (5,5).

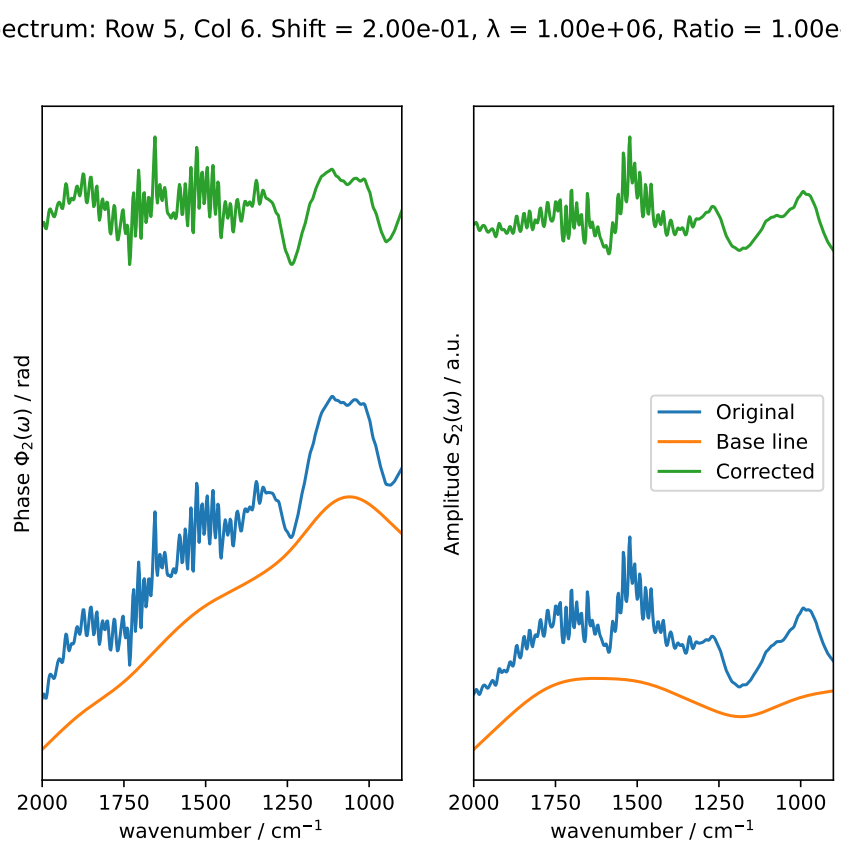

Figure F.42: SINS baseline spectrum for position (5,6).

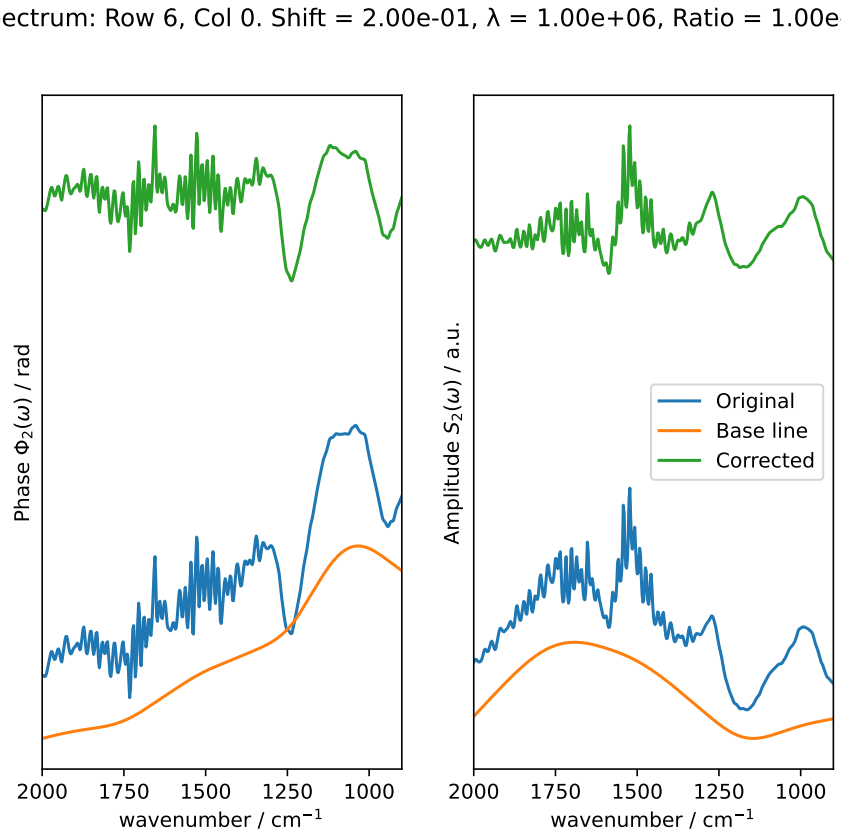

Figure F.43: SINS baseline spectrum for position (6,0).

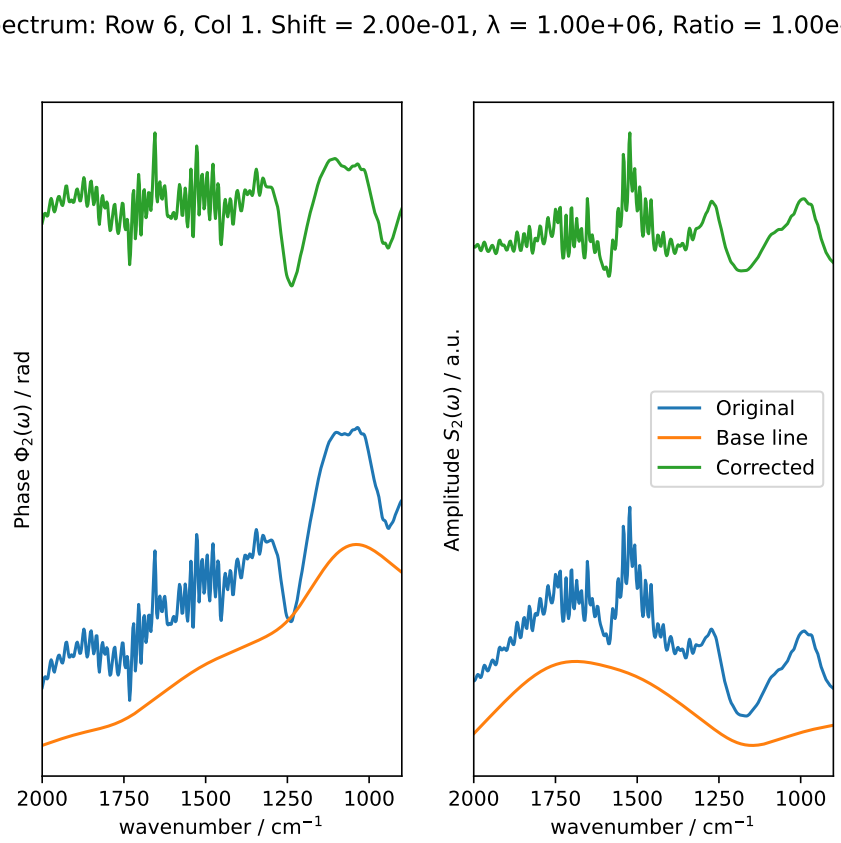

Figure F.44: SINS baseline spectrum for position (6,1).

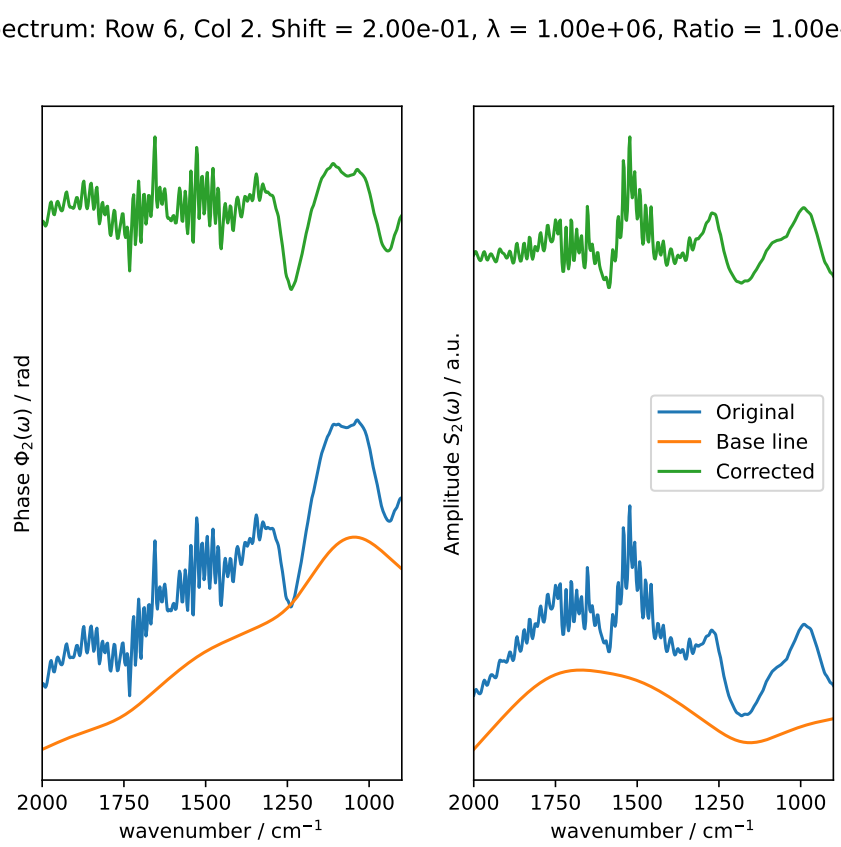

Figure F.45: SINS baseline spectrum for position (6,2).

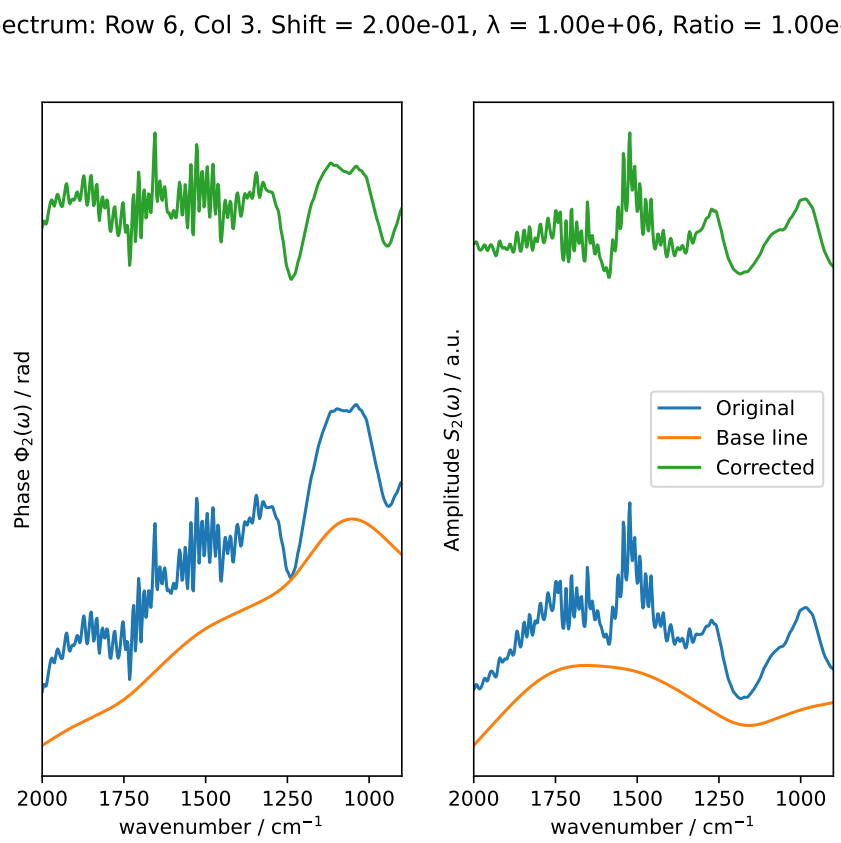

Figure F.46: SINS baseline spectrum for position (6,3).

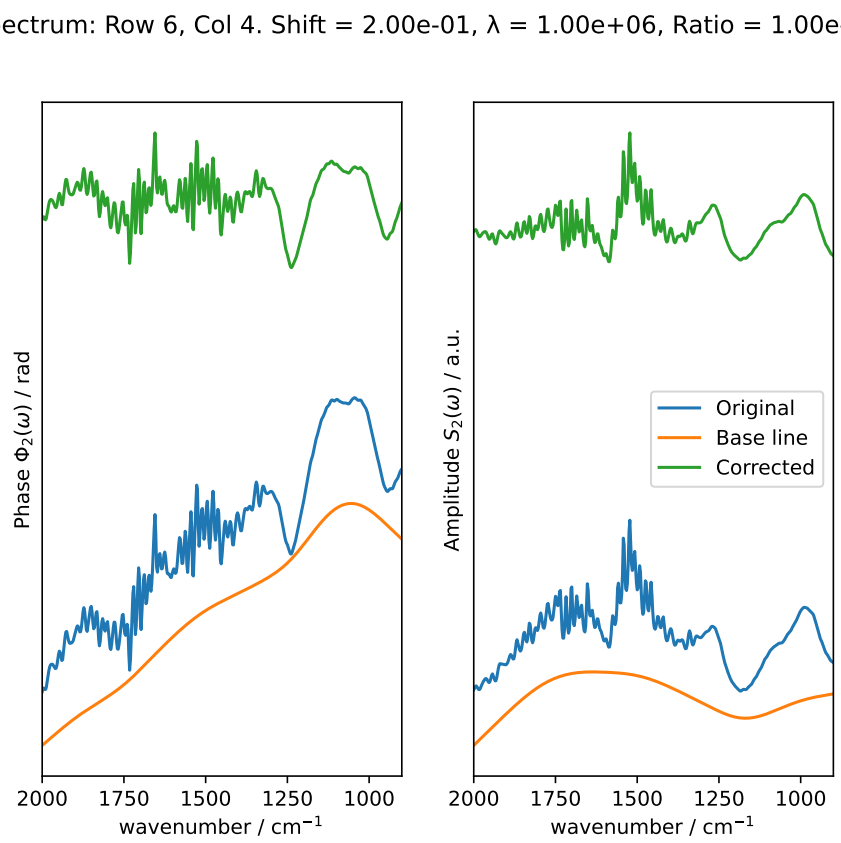

Figure F.47: SINS baseline spectrum for position (6,4).

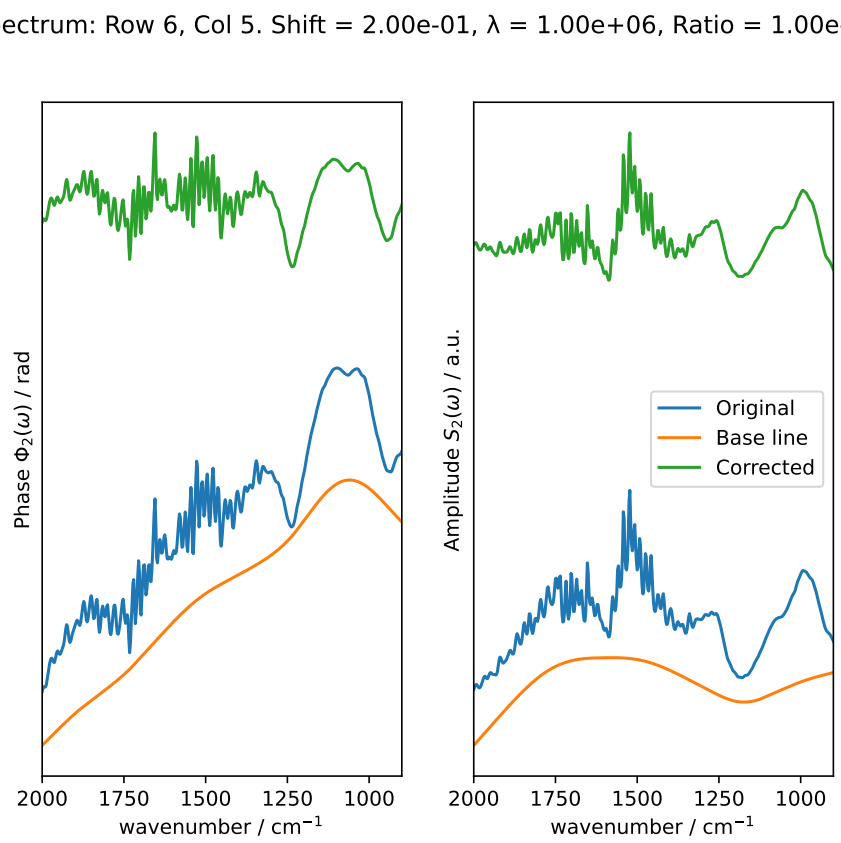

Figure F.48: SINS baseline spectrum for position (6,5).

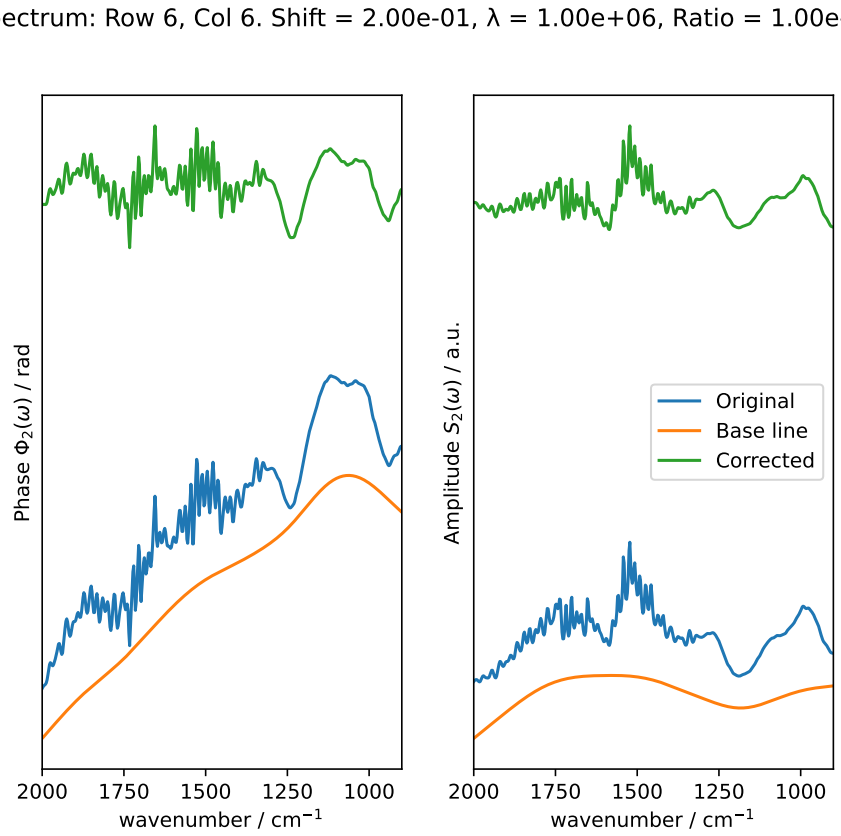

Figure F.49: SINS baseline spectrum for position (6,6).